Fabrication and Characterization of Photonic Bandgap Components

Frandsen, Lars Hagedorn

Publication date:
2006

Document Version
Publisher's PDF, also known as Version of record

Fabrication and Characterization of Photonic Bandgap Components

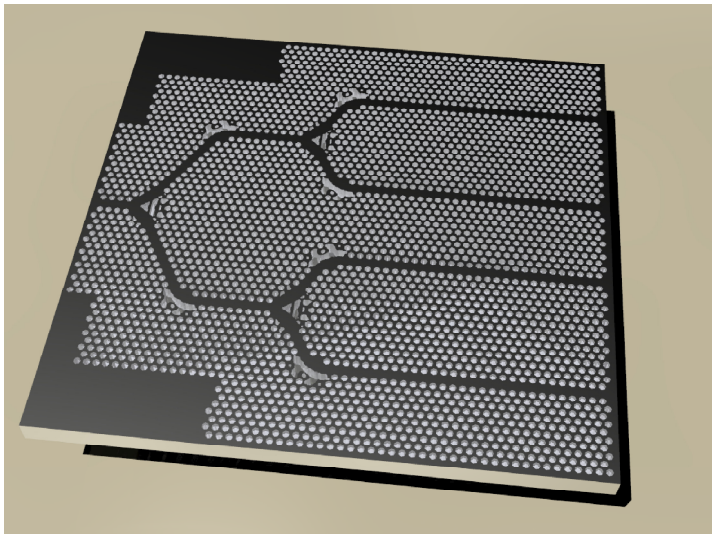

Lars Hagedorn Frandsen

COM•DTU
Department for Communications, Optics & Materials
Technical University of Denmark
Building 345v
2800 Kgs. Lyngby
Denmark

March 2006

Abstract

This ph.d. thesis deals with the modelling, fabrication and characterization of photonic bandgap components realized in silicon-on-insulator material.

Plane-wave expansion theory and finite-difference time-domain modelling are applied to the photonic crystal waveguide and demonstrate how the fundamental properties of such may be altered in terms of the operational wavelength range, the propagation loss, and the dispersion properties. The inverse design method topology optimization is applied to the photonic crystal platform and is demonstrated to be a powerful tool for the optimization of broadband performance for different passive nanophotonic components.

The fabrication of photonic crystals is covered in detail for the utilization of electron beam lithography and reactive ion etching. Photonic crystal structures corrected for proximity effects and with sub-20 nm features are successfully realized and etched with high fidelities and steep wall profiles into silicon. Moreover, nanoimprint lithography is demonstrated to be an attractive candidate for the lithographic step in the mass-production of nanophotonic circuits.

The thesis presents numerous experimental results on fabricated photonic crystal components including various waveguide bends, T- and Y-splitters, wavelength dependent filters, improved butt-couplings, and slow-light waveguides. The results promote the interest of applying photonic bandgap components in nanophotonic circuits that being for simple guiding, splitting, and multiplexing of light or for the utilization of the slow-light phenomenon for non-linear effects or dispersion compensating.

Resumé

Denne ph.d. afhandling beskæftiger sig med modelleringen, fabrikationen og karakteriseringen af fotoniske båndgabs komponenter, som er realiseret i et silicium-på-isolator materiale.

Metoderne "plane-wave expansion theory" og "finite-difference time-domain modelling" er blevet anvendt til at modellere den fotoniske krystal bølgeleder og demonstrerer, hvordan dens egenskaber kan ændres med henblik på det operationelle bølgelængde område, udbredelsestabet, samt dispersions egenskaber. Den inverse design metode topologi optimering er blevet anvendt på fotoniske krystaller og er blevet demonstreret til at være et kraftfuldt værktøj til at optimere bredbånds egenskaberne for forskellige passive nanofotoniske komponenter.

Fabrikationen af fotoniske krystaller er dækket i detaljer for udnyttelsen af elektron-stråle litografi og reaktiv ion ætsning. Fotoniske krystal strukturer, som er korrigeret for elektron-sprednings effekter og med sub-20 nm detaljer, er blevet realiseret med succes og ætset med en meget høj kvalitet og stejle side-vægs profiler i silicium. Endvidere, er nanoimprint litografi blevet demonstreret til at være en attraktiv kandidat til den litografiske del i en masseproduktion af nanofotoniske kredsløb.

Afhandlingen præsenterer en masse eksperimentielle resultater fra fabrikerede fotoniske krystal komponenter det være inklusiv forskellige typer bølgeleder bøj, T- og Y-fordelere, bølgelængde afhængige filtre, forbedrede koblings-overgange, og bølgeledere med langsomt lys. Resultaterne ger interessen for anvendelsen af fotoniske båndsgabs komponenter i nanofotoniske kredsløb om det være for simpel lysledning, lysdeling, og lysfiltrering eller for udnyttelsen af langsomt lys i ikke-lineære effekter eller til dispersions kompensation.

Acknowledgements

The successes of my ph.d. project could not have been without the proficient supervision given by my main supervisor Professor Martin Kristensen and my co-supervisor assistant professor Peter Ingo Borel, whom I would like to thank for guiding me along in the dynamic world of nanophotonics. Also I would like to thank research professor Bjarne Tromborg for taking over the main supervision at the time Martin Kristensen left COM•DTU.

I owe a lot of spare time and thanks to process engineer Peixiong Shi for his neverending helpfulness in the DANCHIP cleanroom. I would like to thank associate professor Andrei Lavrinenko for the inspiring discussions on the modelling of photonic crystal structures and professor Ole Sigmund and associate professor Jakob S. Jensen at MEK•COM for a fruit- and joy-full collaboration and for providing us with the remarkable topology optimization scheme. I would have looked forward to a more extensive collaboration regarding nanoimprint lithography with associate professor Anders Kristensen and his ph.d. students Brian Bilenberg and Theodor Nielsen had the time not been running short.

At times in my project, I have worked closely together with ph.d. students Anders Harpøth, Amèlie Têtu, and Thomas Tanggaard Alkeskjold, whom I thank for the hours spent in the cleanroom or in the lab. I'm also grateful for the collaboration I have had with assistant professor Jacob-Fage Pedersen and ph.d. Rune Jacobsen in respect to the experimental work done on slow-light measurements. Also thanks to visiting post doc. Tapio Niemi for his contributions during his stay at COM•DTU.

The dynamics of my project have been boosted by the presence of national and European projects, and for that I acknowledge all of the partners within the PIPE, PICCO, and ePIXnet projects.

Finally, the energy and motivation I have put into my ph.d. project could not have been without the great colleagues at COM•DTU, my office mate Henrik Rokkjær Sørensen, and my friends and family for their support and encouragement throughout the years.

Ph.D. Publications

Publish or Perish!

The following publications have resulted from this Ph.D. project:

Peer reviewed international scientific journal publications:

1. Morten Thorhauge, Lars H. Frandsen, and Peter I. Borel, "Efficient Photonic Crystal Directional Couplers", *Optics Letters*, Vol. 28, 17, 1525-1527 (2003)

2. Dirk Taillaert, Harold Chong, Peter I. Borel, Lars H. Frandsen, Roel Baets, "A Compact Two-dimensional Grating Coupler used as a Polarization Splitter", *IEEE Photonics Technology Letters*, Vol. 15, 1249-1251 (2003)

3. P. I. Borel, L. H. Frandsen, M. Thorhauge, A. Harpøth, Y. X. Zhuang, M. Kristensen, H. M. H. Chong, "Efficient propagation of TM polarized light in photonic crystal components exhibiting band gaps for TE polarized light", *Optics Express*, Vol. 11, 15, 1757-1762 (2003)

4. A.Lavrinenko, P. I. Borel, L. H. Frandsen, M. Thorhauge, A. Harpøth, M. Kristensen, T. Niemi, and H. M. H. Chong, "Comprehensive FDTD modelling of photonic crystal waveguide components," *Optics Express*, Vol. 12, 2, 234-248 (2004)

5. P.I. Borel, A. Harpøth, L.H. Frandsen, M. Kristensen, P. Shi, J.S. Jensen and O. Sigmund, "Topology optimization and fabrication of photonic crystal structures", *Optics Express*, Vol. 12, 9, 1996-2001 (2004)

6. L. H. Frandsen, P. I. Borel, Y. X. Zhuang, A. Harpøth, M. Thorhauge, M. Kristensen, W. Bogaerts, P. Dumon, R. Baets, V. Wiaux, J. Wouters, S. Beckx, "Ultra-low-loss 3-dB Photonic Crystal Waveguide Splitter", *Optics Letters*, Vol. 29, 14, 1623-1625 (2004)

7. P.I. Borel, L.H. Frandsen, A. Harpøth, J.B. Leon, H. Liu, M. Kristensen, W. Bogaerts, P. Dumon, R. Baets, V. Wiaux, J. Wouters and S. Beckx, "Bandwidth engineering of photonic crystal waveguide bends", *Electronics Letters*, Vol. 40, 20, 1263-1264 (2004)

8. L. H. Frandsen, A. Harpøth, P. I. Borel, M. Kristensen, J. S. Jensen, and O. Sigmund, "Broadband photonic crystal waveguide 60^0 bend obtained utilizing topology optimization", *Optics Express*, Vol. 12, 24, 5916-5921 (2004)

9. P.F. Xing, P.I. Borel, L.H. Frandsen, A. Harpøth and M. Kristensen, "Optimization of Bandwidth in 60^0 Photonic Crystal Waveguide Bends", *Optics Communications*, Vol. 248, 1-3, 179-184 (2005)

10. J. S. Jensen, O. Sigmund, L. H. Frandsen, P. I. Borel, A. Harpøth, and M. Kristensen, "Topology Design and Fabrication of an Efficient Double 90 Photonic Crystal Waveguide Bend", *IEEE Photonics Technology Letters*, Vol. 17, 6, 1202-1204 (2005)

11. P.I. Borel, L.H. Frandsen, A. Harpøth, M. Kristensen, J.S. Jensen and O. Sigmund, "Topology Optimised Broadband Photonic Crystal Y-Splitter", *Electronics Letters*, Vol. 41, 2, 69-71 (2005)

12. Rune S. Jacobsen, Andrei V. Lavrinenko, Lars H. Frandsen, Christophe Peucheret, Beata Zsigri, Gaid Moulin, Jacob Fage-Pedersen, and Peter I. Borel, "Direct experimental and numerical determination of extremely high group indices in photonic crystal waveguides", *Optics Express*, Vol. 13, 20, 7861-7871 (2005)

13. A. Têtu, M. Kristensen, L.H. Frandsen, A. Harpøth, P.I Borel, J.S. Jensen and O. Sigmund, "Broadband topology-optimized photonic crystal components for both TE and TM polarizations" *Optics Express*, vol. 13, pp. 8606-8611 (2005)

14. V. S. Volkov and S. I. Bozhevolnyi, P. I. Borel, L. H. Frandsen, and M. Kristensen, "Near-field characterization of low-loss photonic crystal waveguides", *Physical Review B*, vol. 72, pp. 035118-1 – 035118-7 (2005).

15. V. S. Volkov, S. I. Bozhevolnyi, P. I. Borel, L. H. Frandsen and M. Kristensen. "Near-field characterization of photonic crystal Y-splitters" *Physica Status Solidi C*, vol. 2, pp. 4087-4092 (2005).

16. Tapio Niemi, Lars Hagedorn Frandsen, Kristian Knak Hede, Anders Harpøth, Peter Ingo Borel, and Martin Kristensen, "Wavelength Division De-Multiplexing Using Photonic Crystal Waveguides", *IEEE Photonics Technology Letters*, vol. 18, no. 1, pp. 226-228 (2006).

17. Rune Jacobsen, Karin Andersen, Peter I. Borel, Jacob Fage-Pedersen, Lars H. Frandsen, Ole Hansen, Martin Kristensen, Andrei Lavrinenko, Gaid Moulin, Haiyan Ou, Christophe Peucheret, Beta Zsigri & Anders Bjarklev, "Strained silicon as a new electro-optic material", *Nature* 441, pp. 199-202 (2006).

18. L.H. Frandsen, A. Lavrinenko, J. Fage-Pedersen, P.I. Borel, "Photonic crystal waveguides with semi-slow light and tailored dispersion properties", accepted for publication in Optics Express (2006).

Peer reviewed international scientific conference publications:

1. L.H. Frandsen, P.I. Borel, M. Thorhauge, J. Cheng, M. Kampanis, M. Kristensen, A. Lavrinenko, Y. Zhuang, H.M.H. Chong, "Propagation of TE and TM polarised light through smoothed sixty degree bends in planar photonic crystal waveguides", Paper CM4-1-FRI, *CLEO-Europe'03*, Munich, Germany (2003)

2. P.I. Borel, M. Thorhauge, L.H. Frandsen, J. Cheng, M. Kampanis, M. Kristensen, A. Lavrinenko, Y. Zhuang, H.M.H. Chong, "Very high coupling of

TM polarised light in photonic crystal directional couplers", Paper CM4-2-FRI, *CLEO-Europe'03*, Munich, Germany (2003)

3. P.I. Borel, L.H. Frandsen, M. Thorhauge, A. Boltasseva, J. Cheng, M. Kampanis, M. Kristensen, A. Lavrinenko, K. Rechendorff, R. Shim, Y. Zhuang, H.M.H. Chong, "Very low losses for TM polarized light in photonic crystal waveguides", Paper JWC3, *CLEO/QELS'03*, Baltimore, Maryland, USA (2003)

4. Lars H. Frandsen, Morten Thorhauge, Peter I. Borel, Martin Kristensen, Anders Harpøth, Harold M.H. Chong, Richard M. De La Rue, "Ultra-Compact Photonic Bandgap Waveguide Coupler", Paper TU1.1.4, Vol. 5, 44-45, *ECOC'03* , Rimini, Italy (2003)

5. V.S. Volkov, S.I. Bozhevolnyi, P.I. Borel, L.H. Frandsen, M. Kristensen and H.M.H. Chong, 'Near-field imaging of low loss photonic crystal waveguides', Paper Tu4.1.3, Vol. 5, 68-69, *ECOC'03*, Rimini, Italy (2003)

6. Morten Thorhauge, Peter I. Borel, Lars H. Frandsen, Martin Kristensen, Andrei Lavrinenko, and Harold Chong, "Properties of Directional Couplers using Photonic Crystal Waveguides", Paper ThI5, 494-495, *OFC'03*, Atlanta, USA (2003)

7. Thomas F Krauss, Roel Baets, Martin Kristensen, Peter I Borel, Lars H Frandsen, Morten Thorhauge, Bjarne Tromborg, Richard M De La Rue, Luciano Socci, Michele Midrio and Dominic Gallagher, "Photonic Integrated Circuits using Crystal Optics (PICCO)", Paper ThB2, 113-120, *ECIO'03*, Prague, Tjekkiet (2003)

8. Dirk Taillaert, Roel Baets, Harold Chong, Richard M. De La Rue, Peter I. Borel, Lars H. Frandsen, "A Compact Two-dimensional Grating Coupler used as a Polarization Splitter", Vol. 4, 5-8, *ECIO'03*, Prague, Tjekkiet (2003)

9. Y.X. Zhuang, L.H. Frandsen, A. Harpøth, M. Thorhauge, M. Kristensen, P.I. Borel, W. Bogaerts, R. Baets, "Wavelength tuning of photonic crystal waveguides fabricated using 248-nm deep UV lithography", Paper ThR2, *OFC'04*, San Jose, USA (2004)

10. L.H. Frandsen, P.I. Borel, A. Harpøth, M. Kristensen, M. Thorhauge, W. Bogaerts, P. Dumon, R. Baets, V. Wiaux, J. Wouters, S. Beckx, " Ultra-low-loss 3-dB Photonic Crystal Waveguide Splitter", Paper TU-P52, 146, *PECS-V*, Kyoto, Japan (2004)

11. M. Kristensen, L.H. Frandsen, A. Harpøth, Y.X. Zhuang, P.I. Borel, W. Bogaerts, P. Dumon, R. Baets, V. Wiaux, J. Wouters, S. Beckx, "Large bandwidth 60^0 bend in photonic crystal waveguides", Paper Tu-F5, 93, *PECS-V*, Kyoto, Japan (2004)

12. A. Harpøth, L.H. Frandsen, P.I. Borel, M. Kristensen, J.S. Jensen, O. Sigmund, P. Shi, "Fabrication of topology optimized photonic crystal waveguide Z-bend displaying large bandwidth with very low bend loss", Paper Tu-E3, 83, *PECS-V*, Kyoto, Japan (2004)

13. V. S. Volkov, S. I. Bozhevolnyi, P. I. Borel, M. Kristensen, L.H. Frandsen, "Near-Field Characterization of Low-Loss Photonic Crystal Waveguides", Paper Mo04, *NFO-8*, Seoul, Korea (2004)

14. M. Thorhauge, L.H. Frandsen, P.I. Borel, A. Harpøth, Y.X. Zhuang, M. Kristensen, "Novel low-loss 60^0 bends in photonic crystal waveguides", Paper CWP2, *CLEO/QELS'04*, San Francisco, USA (2004)

15. M. Kristensen, P.I. Borel, L.H. Frandsen, A. Harpøth, J.S. Jensen and O. Sigmund, "Optimized planar photonic crystal waveguide 60^0 bend with more than 200nm wide 1-dB transmission bandwidth", Paper OWD6, *OFC'05*, Anaheim, USA (2005)

16. A. V. Lavrinenko, L. H. Frandsen, J. Fage-Pedersen, and P. I. Borel, "Photonic crystal waveguides based on an antiresonant reflecting platform", Proceedings of 2005 7th International Conference on Transparent Optical Networks - *ICTON 2005*, pp. 273-276, Tu.A2.1, Barcelona, Spain (2005).

17. V.S. Volkov, S.I. Bozhevolnyi, P.I. Borel, L.H. Frandsen and M. Kristensen, "Near-Field Characterization of Photonic Crystal Components", *Proceedings of CLEO-Europe'05*, p. 603, Munich, Germany (2005)

18. T. Niemi, L. H. Frandsen, A. Harpøth, P. I. Borel, and M. Kristensen, "Integrated optical components based on planar photonic crystal waveguides with perturbed border holes" *CLEO/Europe-EQEC 2005*, Europhysics Conference Abstracts vol. 29B, 1 page, Munich, Germany (2005).

19. A. Têtu, M. Kristensen, L.H. Frandsen, A. Harpøth, P.I. Borel, J.S. Jensen and O. Sigmund, "Low-Loss Photonic Crystal Y-Splitter for TM Polarization", Poster presentation, *BGPP'05*, Sydney, Australia (2005)

20. B. Bilenberg, M. Schøler, M. S. Schmidt, P. Shi, P. Bøggild, L. H. Frandsen, P. I. Borel, and A. Kristensen. "High pattern density nanoimprint lithography stamps fabricated by means of negative electron beam lithography resist, TEBN-1, and dry etching in silicon", *4th International Conference on Nanoimprint and Nanoprint Technology (NNT'05)*, poster presentation, 20P-5-29, Nara, Japan (2005).

21. P. I. Borel, L. H. Frandsen, J. Burgos Leon, T. Niemi, and A. Lavrinenko. "Optimization and applications of planar silicon-based photonic crystal devices" (invited) A*Active and Passive Optical Components for WDM Communications V* - Proceedings of SPIE, vol. 6014, pp. 601410-1 - 601410-9, Boston, Massachusetts, USA (2005).

22. Andrei V. Lavrinenko, Rune S. Jacobsen, Jacob Fage-Pedersen, Lars H. Frandsen, Beata Zsigri, Christophe Peucheret, and Peter I. Borel, "Extreme group index measured and calculated in 2D SOI-based photonic crystal waveguides", Proceedings of *LEOS 2005*, p.320-321, Sydney, Australia (2005)

23. T. Niemi, P. I. Borel, L. H. Frandsen, A. Harpøth, K. K. Hede, and M. Kristensen. "In-plane Wavelength Division De-Multiplexing Using Photonic Crystals" *PECS-VI: International Symposium on Photonic and electromagnetic Crystal Structures* - Conference Program, poster presentation A18, Aghia Pelaghia, Crete, Greece (2005).

24. L. H. Frandsen, A. Harpøth, K. K. Hede, M. Kristensen, P. I. Borel, J. S. Jensen, and O. Sigmund. "Topology Optimised Photonic Crystal 1x4 Waveghuide Splitter" *PECS-VI: International Symposium on Photonic and Electromagnetic Crystal Structures* - Conference Program, poster presentation B14, Aghia Pelaghia, Crete, Greece (2005).

25. A. V. Lavrinenko, R. S. Jacobsen, J. Fage-Pedersen, B. Zsigri, C. Peucheret, L. H. Frandsen, M. Kristensen, and P. I. Borel. "Direct numerical and experimental determination of group index dispersion in photonic crystal waveguides", *Photonic Crystals and Fibers* - Proceedings of SPIE, vol. 5950, pp. 59500F-1 - 59500F-11, Warsaw, Poland (2005).

26. Brian Bilenberg, Lars Hagedorn Frandsen, Theodor Nielsen, Marko Vogler, Peter Ingo Borel, and Anders Kristensen, "Nanoimprint lithography of topology optimized photonic crystal devices", Proceedings of CLEO USA, CTuK2, p.106 (2006).

27. Amélie Tétu, Lirong Yang, Andrei V. Lavrinenko, Lars H. Frandsen and Peter I. Borel, "Enhancement of coupling to the slow light regime in photonic crystal waveguides using topology optimization", Proceedings of CLEO USA, CTuAA2, p.127 (2006).

28. Andrei V. Lavrinenko, Amélie Têtu, Lars H. Frandsen, and Peter I. Borel, "Optimization of photonic crystal 60^0 waveguide bends in the slow light regime for broadband transmission", Proceedings of CLEO USA, QFC6, p.199 (2006).

29. L.H. Frandsen, P.I. Borel, J.S. Jensen and O. Sigmund, "Topology optimized photonic wire splitters", Proceedings of CLEO USA, CMV4, p.85 (2006).

30. L.H. Frandsen, A. Lavrinenko, J. Fage-Pedersen, P.I. Borel, "Tailoring the Group Velocity in Photonic Crystal Waveguides," Proceedings of Slow and Fast Light Topical Meeting, MD4, Washington (2006)

Non-reviewed scientific conference publications:

1. M.Kristensen, P.I. Borel, L.H. Frandsen, A. Harpøth, A. Lavrinenko, T. Niemi, P.F. Xing, P. Shi, J.S. Jensen and O. Sigmund, "Optimal design in nanophotonics" Invited talk, DTU Nano-symposium, Kgs. Lyngby, Denmark (2004)

2. Peter I. Borel, Lars H. Frandsen, Anders Harpøth, Martin Kristensen, Tapio Nemi, Pengfei Xing, Jakob S. Jensen, Ole Sigmund, "Design and fabrication of SOI-based photonic crystal components", Invited paper Tu.A2.4, *ICTON'04/ESPC'04*, Wroclaw, Poland (2004)

3. M. Kristensen, P.I. Borel, L.H. Frandsen, A. Harpøth and T. Niemi, "Design and Fabrication of Planar PBG Components", Invited paper SYA4, EPS-QEOD, Lausanne, Switzerland (2004)

4. B. Bilenberg, M. Schøler, M. S. Schmidt, P. Bøggild, A. Kristensen, P. Shi, L. H. Frandsen, and P. I. Borel, "High pattern density nanoimprint lithography stamps fabricated by means of negative electron beam lighography resist and dry etching in silicon", poster presentation, DOPS Annual Meeting abstracts, p. 26, Roskilde, Denmark (2005).

5. V.S. Volkov, S.I. Bozhevolnyi, P.I. Borel, L.H. Frandsen and M. Kristensen, "Near-Field Characterization of Photonic Crystal Y-Splitters", OSI-6 Conference, Ålborg, Denmark (2005)

6. V. S. Volkov, S. I. Bozhevolnyi, P. I. Borel, L. H. Frandsen, and M. Kristensen, "Near-field characterization of photonic crystal components", poster presentation, DOPS Annual Meeting abstracts, p. 32, Roskilde, Denmark (2005).

7. L. H. Frandsen, A. Harpøth, K. K. Hede, M. Kristensen, T. Niemi, and P. I. Borel, "In-plane wavelength division de-multiplexing using photonic crystals", poster presentation, Nano•DTU day, June 8, Kgs. Lyngby, Denmark (2005).

8. L. H. Frandsen, K. K. Hede, P. I. Borel, J. S. Jensen, and O. Sigmund, "Topology optimised planar photonic crystal building blocks", poster presentation, Nano•DTU day, June 8, Kgs. Lyngby, Denmark (2005).

9. K. K. Hede, J. Burgos Leon, L. H. Frandsen, P. I. Borel, J. S. Jensen, and O. Sigmund, "Topology optimised wavelength dependent splitters" Nano•DTU day, June 8, Kgs. Lyngby, Denmark (2005).

10. H. Liu, L. H. Frandsen, P. I. Borel, and J. Fage-Pedersen, "Planar photonic crystal waveguides in silicon oxynitride", poster presentation, Nano•DTU day, June 8, Kgs. Lyngby, Denmark (2005).

11. H. Liu, L. H. Frandsen, A. Têtu, P. I. Borel, and J. Fage-Pedersen, "Photonic crystal waveguides in PECVD glass", poster presentation, Nano•DTU day, December 6, Kgs. Lyngby, Denmark (2005).

12. G. Moulin, R. S. Jacobsen, A. V. Lavrinenko, L. H. Frandsen, P. I. Borel, and J. Fage-Pedersen, "Slow light in photonic crystal waveguides", poster presentation, Nano•DTU day, June 8, Kgs. Lyngby, Denmark (2005).

13. A. V. Lavrinenko, R. S. Jacobsen, J. Fage-Pedersen, L. H. Frandsen, B. Zsigri, C. Peucheret, and P. I. Borel, "Simulation and measurement of slow light in photonic crystal waveguides", poster presentation, Nano•DTU day, December 6, Kgs. Lyngby, Denmark (2005).

14. A. V. Lavrinenko, R. S. Jacobsen, J. Fage-Pedersen, L. H. Frandsen, B. Zsigri, C. Peucheret, and P. I. Borel. "Slow light in photonic crystal waveguides" DOPS Annual Meeting abstracts, p. 13, Roskilde, Denmark (2005).

Patent applications:

1. Rune Jacobsen et al, U.S. provisional patent application, 38932US1, 2005

Relevant scientific publications from my Master Thesis:

1. J. Arentoft, T. Søndergaard, M. Kristensen, A. Boltasseva, M. Thorhauge, and L. Frandsen, "Low-loss silicon-on-insulator photonic crystal waveguides", *Electronics Letters*, Vol. 38, 6, 274-275 (2002)

2. M. Thorhauge, M. Kristensen, J. Arentoft, L. Frandsen, T. Søndergaard, A. Boltasseva, and P.I. Borel, "Reduced coupling loss between fiber and planar photonic crystal waveguide", Paper Th-P-029, *Nano-7 / Ecoss-21*, Malm, Sweden (2002)

3. P.I. Borel, L.H. Frandsen, Y. Zhuang, M. Thorhauge, A. Lavrinenko, M. Kristensen, and M.H. Chong, "Propagation loss in photonic crystal waveguides", DOPS'02, Session III, Risoe, Denmark (2002)

4. M. Thorhauge, L. Frandsen, J. Arentoft, M. Kristensen, and T. Søndergaard, "Improving coupling loss to photonic bandgap waveguide structures by exposing the input fiber tip to UV-light", DOPS'02, Session III, Risoe, Denmark (2002)

5. M. Kristensen, A. Boltasseva, P.I. Borel, L.H. Frandsen, M. Thorhauge and B. Tromborg, "Integrated Photonic Crystal Waveguide Technology in Europe", Invited talk at ACOFT, Sydney, Australia (2002)

Contents

Chapter 1

Introduction

Why Photonics in Silicon?

Being a semiconductor and having an oxide with excellent properties, silicon is today one of the most important industrial materials and has for more than half a century been the choice of material for realizing integrated electronic circuits. In this way, silicon material permeates almost every facet of our daily lives.

Having an *indirect* electronic bandgap, though, bulk silicon only has limited active optical properties in contrast to III-V semiconductor compounds, which are widely used in e.g. photodiodes, light emitting diodes, and semiconductor lasers. For that reason, silicon has been a material for electronics; not photo-nics! Nevertheless, there has been an extreme commercial interest in 'siliconi-zing' photonics as the computing- and communication- industries face increasing challenges to deliver more data; faster; at a cheaper price. While microprocessors processing the delivered data are projected to meet future demands, the bandwidth of the databus interconnects needs to be increased to meet the speed of the microprocessors. This may be achieved by utilizing a monolithic integration of optical components on CMOS-compatible silicon chips for routing and molding datasignals on-chip in the optical domain.

Recently, major breakthroughs within the optical properties of silicon have been achieved and pave the way for the fully integrated electro-optic silicon chip (see e.g. ref. [1] for a recent review of silicon photonics). Major achievements include the recent demonstrations of Raman-amplification and four-wave-mixing in a silicon optical waveguide [2,3] that allow optical lasing, amplification, and wavelength conversion in silicon to be realized. Focus has also been put on demonstrating giga-hertz optical modulation of a signal in silicon, typically through charge density modulation [4]. Along with the development of low-loss silicon waveguides and simple passive components [5], ultra-fast cross-absorption modulation [6], and a strain-induced χ^2-coefficient in silicon waveguides [7], si-licon is indeed becoming a very attractive material for electro-optic circuits. In this way, great advantage can be taking by exploiting the fabrication-knowledge and foundries build up dur-

ing the last decades in the electronic industry, thus, making the electro-optic silicon chip a very cost-effective solution.

Why Photonic Crystals?

Guiding light in an optical waveguide is in principal a simple task. Conventional waveguides are based on the principle of total-internal-reflection (TIR) that allows an optical signal to be confined and guided in a core-material having a higher refractive index than the cladding. Conventional waveguides are easily realized in silicon as silicon is transparent for wavelengths used in optical fibers and has a high refractive index leading to a tight mode-confinement. Hence, simple tasks as guiding, bending, splitting, and coupling of optical signals can be carried out effectively in high-index silicon waveguide components with very small footprints on the chip. However, more complicated functionalities needed in electro-optic circuits as e.g. wavelength (de-)multiplexing, dispersion con-trol, increased light/matter interaction, and optical buffering may require more sophisticated solutions than using conventional TIR waveguides.

The periodic placement of *atoms* in a crystalline material may give rise to an electronic bandgap between the valence band and the conduction band wherein no electronic states can exist. In a similar way, a periodicity in the refractive index-profile on the scale of the wavelength in an optical material may open for a *photonic* bandgap that prevents signals of certain wavelengths to exist in the material [8,9]. Such a periodic medium is refereed to as a *photonic crystal* (PhC). Figure 1.1 sketches how PhCs may be realized in 1-,2-, or 3-dimensions. Optical waves propagating in the PhC structure scatter within each period due to the refractive index-difference and may either add-up constructively or cancel-out destructively. In this way, the PhC structure becomes either transparent or opaque to the travelling optical beam. The interference pattern is dependent on the wavelength and the travelling direction of the beam with respect to the index-profile. If the index-modulation is large and applied properly PhCs may have wavelength ranges, so-called photonic bandgaps (PBGs), where light cannot propagate through the structure. Defects in a PhC give rise to local optical states and open for e.g. routing of optical signals along line-defects or give resonant states with high Q-values in point-defects. As will be presented in this thesis, the behavior of such defect states may be novel and very different from modes in conventional TIR waveguides and allow exotic photonic components to be realized.

Due to the invariance of optical fibers along the direction of propagation 1D PhCs (also known as Bragg gratings) are conveniently realized in fibers and are widely used in the telecommunications industry as e.g. optical filters. Simple techniques have also been developed for the implementation of 1D gratings in planar silica-on-silicon waveguides [10, 11]. However, their 1D nature limits the functionalities of such. Waveguides and components fabricated in 3D PhCs are conceptually ideal building blocks for photonic circuits since they by nature have no scattering losses to the surroundings where all light propagation is forbidden

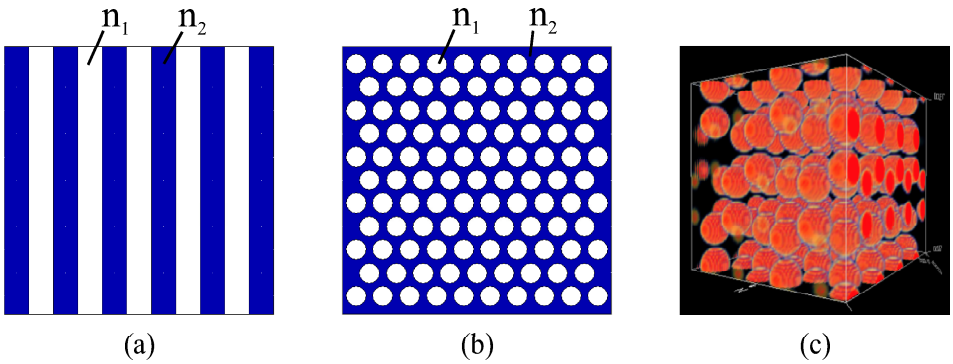

Figure 1.1: (a) A 1D photonic crystal consisting of a stack of piecewise constant refractive index materials has been known for a long time as a Bragg grating, which is widely used in the telecommunications industry. (b) 2D photonic crystals can e.g. be defined by periodically-placed air holes in a semiconductor material and are as such compatible with conventional CMOS fabrication technology. (c) The 3D photonic crystals can e.g. be constructed by stacking semiconductor spheres in a diamond lattice configuration. They are, however, rather cumbersome to fabricate and at present time difficult to integrate with planar electronic/photonic circuits.

within the PBG. However, they are difficult to fabricate and integrate with planar optical and electronic circuits. Therefore, more attention is at present time paid to 2D PhC structures integrated into slab configurations, which confine light in-plane by the PBG effect and out-of-plane by total-internal-reflection [12].

Why this Thesis?

The scope of this thesis is to discuss and demonstrate the modelling, fabrication, and characterization of planar photonic crystal structures realized in silicon-on-insulator material. The purpose is not to be a teachers-book on, nor a review of photonic crystals. However, it will present the main results from the research carried out on planar photonic crystals within the last three years in the Nanophotonics group at the "Department for Communications, Optics & Materials" (COM•DTU) located at the Technical University of Denmark (DTU).

Beside working together with people at COM•DTU, the work has partly been done in collaboration with partners within the European IST "Photonic Integrated Circuits using Photonic Crystal Optics" (PICCO) project, the national FTP "Planar Integrated Photonic Elements" (PIPE) project, and the European FP6 "European Network of Excellence on Photonic Integrated Components and Circuits" (ePIXnet) research project. Moreover, I have had a very fruitful inter-disciplinary collaboration with the "Department of Mechanical Engineering" (MEK•DTU) at DTU addressing topology optimization of photonic crystal components. For the

fabrication of photonic crystal components using nanoimprint lithography I have had a close collaboration with the Nanoimprint group at the "Department of Micro and Nanotechnology" (MIC•DTU). Last, but not least, great technological assistance have been obtained from the technicians associated with the DANCHIP cleanroom facility at DTU.

My role in the work presented here has been many-fold. The ph.d. project was formulated as being an experimental project with focus on the fabrication and characterization of simple passive photonic crystal components and, as such, I have been the "photonic handyman" of the group designing, simulating, fabricating, and characterizing photonic crystal components fulfilling different milestones of the funding projects. Specifically, within the fabrication part, extensive investigations have been conducted in the DANCHIP cleanroom in order to optimize the fabrication-line for photonic crystals utilizing the newly acquired electron beam facility (JEOL JBX9300FS installed in the late summer of 2004 and operational in the early spring of 2005). Some of the cleanroom work has been carried out in collaboration with (former) ph.d. student Anders Harpøth and ph.d. student Amélie Têtu. Beside the experimental aspects of the project, I have also been working extensively on the modelling and optimization of photonic crystal structures in collaboration with the theoreticians in the group.

Structure of the Thesis

This thesis is divided into seven chapters and four Appendices, the first chapter being this introduction and the last chapter containing the conclusion of the thesis. **Chapter 2** will give a short introduction to the mathematics governing photonic crystal structures and present two different domains wherein such can be modelled. After presenting the material platform in focus **Chapter 3** will continue on describing some fundamental properties of the photonic crystal waveguide by applying the plane-wave expansion method and the finite-difference time-domain scheme to model such. The main focus of **Chapter 4** is the design and optimization methods that have been used in the project. Specifically, the chapter will describe the topology optimization method that have been applied with great success to photonic crystal components. **Chapter 5** deals with the fabrication of photonic crystal structures in silicon, focusing on electron-beam and nanoimprint lithography. The chapter will only show the successes achieved in the cleanroom. However, the road along has been rather curved[1]. Finally, **Chapter 6** will present the experimental results obtained from the characterization of nanophotonic circuits, specifically, containing photonic crystal waveguide components. The Appendices of the thesis are included in order to (hopefully) assist in the future work to be carried out on photonic crystals at COM•DTU as they deal with parameters and recipes developed du-ring the project in the modelling and fabrication of such.

[1] For details consult my shrink.

Chapter 2

Theory of Photonic Crystals

As the name expresses, photonic crystals are materials having a crystalline (periodic) structure on the order of the wavelength of photons propagating in the material. They are an optical realization of the semiconductors having electronic bandgaps, wherein no electronic states exist, hence, PhCs have frequency ranges wherein no optical states exists. The principle of realizing PhCs was proposed in 1987 independently by Yablonovitch et al. [8] and S. John [9]. Their ideas started a new research area, which is now among the most exciting and high-profile areas in optics. This second chapter of the thesis will present the basic theory of photonic crystals and introduce two different approaches to solve the equation(s) arising from the theory and to obtain quantitative and qualitative information of photonic crystal structures.

2.1 Maxwell's Equations

To understand how electromagnetic waves propagate in a photonic crystal structure having a periodic index-profile, we need to go back to the year 1873 where James Clerk Maxwell published his *Treatise on Electricity and Magnetism*, in which he concluded that light *is* electromagnetic waves. In the book, Maxwell lists four key equations describing how the space- and time-dependent electromagnetic fields $\mathbf{D}$, $\mathbf{B}$, $\mathbf{E}$, and $\mathbf{H}$ are coupled to each other through differential equations including the field sources $\rho(\mathbf{r},t)$ and $\mathbf{J}(\mathbf{r},t)$, which are the density of free charges and currents, respectively. In their full form the equations take the form [13]:

$$\nabla \cdot \mathbf{D}(\mathbf{r},t) = \rho(\mathbf{r},t) \quad (2.1)$$
$$\nabla \cdot \mathbf{B}(\mathbf{r},t) = 0 \quad (2.2)$$
$$\nabla \times \mathbf{E}(\mathbf{r},t) = -\frac{\partial \mathbf{B}(\mathbf{r},t)}{\partial t} \quad (2.3)$$
$$\nabla \times \mathbf{H}(\mathbf{r},t) = \mathbf{J}(\mathbf{r},t) + \frac{\partial \mathbf{D}(\mathbf{r},t)}{\partial t} \quad (2.4)$$

The electromagnetic fields are related by the constitutive relations:

$$\mathbf{D} = \varepsilon\mathbf{E} = \varepsilon_r\varepsilon_0\mathbf{E} \quad (2.5)$$
$$\mathbf{B} = \mu\mathbf{H} = \mu_r\mu_0\mathbf{H} \quad (2.6)$$
$$\mathbf{J} = \gamma\mathbf{E} \quad (2.7)$$

where the properties of the material in which the fields propagate are contained in ε and μ, which are the dielectric function (or *permittivity*) and the *permeability*, respectively. The conductivity of the material is given by γ.

When considering the types of materials that PhC structures typically are implemented into, and under which conditions light propagate through them, some simplifications to eqs. (2.1)-(2.4) are permissable with the use of eqs. (2.5)-(2.7). First of all we assume that the host material is non-magnetic, isotropic, and that material losses are negligible. We also assume that the field energy are low so that we operate the material in the linear regime. Next, we disregard any material dispersion, so that ε and μ in total become real functions independent of field magnitude, direction, and frequency. Normally, no free currents or charges are present and we can put $\rho = 0$ and $\mathbf{J}$=0. In this way Maxwell's equations (2.1)-(2.4) reduce to the two linear wave equations:

$$\nabla \times \mathbf{E}(\mathbf{r},t) = -\mu_0\frac{\partial \mathbf{H}(\mathbf{r},t)}{\partial t} \quad (2.8)$$
$$\nabla \times \mathbf{H}(\mathbf{r},t) = \varepsilon\frac{\partial \mathbf{E}(\mathbf{r},t)}{\partial t} \quad (2.9)$$

where the dielectric constant $\varepsilon = \varepsilon(\mathbf{r})$ describes the structure through which the electromagnetic fields propagate. The solutions to the wave equations are sca-lable to any length scale[1] [14, 15] as no length dependent parameters are present in the equations (as opposed to e.g. the Bohr radius in quantum mechanics). Thus, the optical properties of the PhC structure can be tuned to any wavelength region by scaling the fundamental parameters of the dielectric structure as will be presented in chapter 3.

[1] As long as the material is macroscopic compared to the wavelength of the light.

2.2 Methods of Modelling

The wave equations, eq. (2.8) and eq. (2.9) for a given $\varepsilon(\mathbf{r})$ can seldomly be solved analytically and it is often necessary to use numerical techniques to solve them.

2.2.1 Plane-Wave Expansion Method

In the frequency domain, solutions to eq. (2.8) and eq. (2.9) are found as $\mathbf{E}$ and $\mathbf{H}$ are assumed to be harmonically[2] varying in time t at some angular frequency ω. The field vectors $\mathbf{E}$ and $\mathbf{H}$ can, thereby, be separated into a spatial- and time-dependent part and written as

$$\mathbf{H}(\mathbf{r},t) = \mathbf{H}(\mathbf{r})e^{i\omega t} \quad (2.10)$$

$$\mathbf{E}(\mathbf{r},t) = \mathbf{E}(\mathbf{r})e^{i\omega t} \quad (2.11)$$

where $\mathbf{E}(\mathbf{r})$ and $\mathbf{H}(\mathbf{r})$ each govern the spatial distribution of the fields and the term $e^{i\omega t}$ describes the harmonic variation of the fields in time t. Inserting eq. (2.10) and eq. (2.11) into eq. (2.8) and eq. (2.9), performing the time derivations, and taking the harmonic time dependence to be explicitly understood, we obtain

$$\nabla \times \mathbf{H}(\mathbf{r}) = i\omega\varepsilon(\mathbf{r})\mathbf{E}(\mathbf{r}) \quad (2.12)$$

$$\nabla \times \mathbf{E}(\mathbf{r}) = -i\omega\mu_0\mathbf{H}(\mathbf{r}) \quad (2.13)$$

By setting $\varepsilon(\mathbf{r}) = \varepsilon_0\varepsilon_r(\mathbf{r})$ it is now convenient to formulate the problem in terms of $\mathbf{H}(\mathbf{r})$. First, eq. (2.12) is divided with $\varepsilon_r(\mathbf{r})$. Next, the curl of eq. (2.12) is taken, and eq. (2.13) is used to eliminate $\mathbf{E}(\mathbf{r})$. The result is an equation in $\mathbf{H}(\mathbf{r})$ alone:

$$\nabla \times \left\{ \frac{1}{\varepsilon_{\mathrm{r}}(\mathbf{r})} \nabla \times \mathbf{H}(\mathbf{r}) \right\} = \frac{\omega^2}{c^2}\mathbf{H}(\mathbf{r}) \quad (2.14)$$

with $c^2 = 1/(\varepsilon_0\mu_0)$. Eq. (2.14) is a single time-independent eigenvalue equation that governs the propagation of light with frequency ω in a dielectric material described by $\varepsilon_r(\mathbf{r})$. The convenience of dealing with the magnetic field vector $\mathbf{H}$ becomes evident as the operator is Hermitian. This gives orthogonal solutions to eq. (2.14) having real eigenvalues ($\frac{\omega^2}{c^2}$) [14].

We seek to solve the 'master' equation (2.14) for a photonic crystal with a spatially varying dielectric function $\varepsilon(\mathbf{r})$ in order to obtain the allowed frequencies of light in the structure. The discrete translational symmetry of the photonic crystal states that

$$\varepsilon_{\mathrm{r}}(\mathbf{r}) = \varepsilon_{\mathrm{r}}(\mathbf{r}+\mathbf{R}) \quad (2.15)$$

where $\mathbf{R}$ is a lattice vector that for all $\mathbf{r}$ translates the lattice onto itself. This allows Bloch's theorem and a variational principle to be applied as described in detail in

[2]This assumption is justified as Fourier analysis allows one to build any solution to a linear equation (as the simplified Maxwell's equations are) from harmonically varying functions.

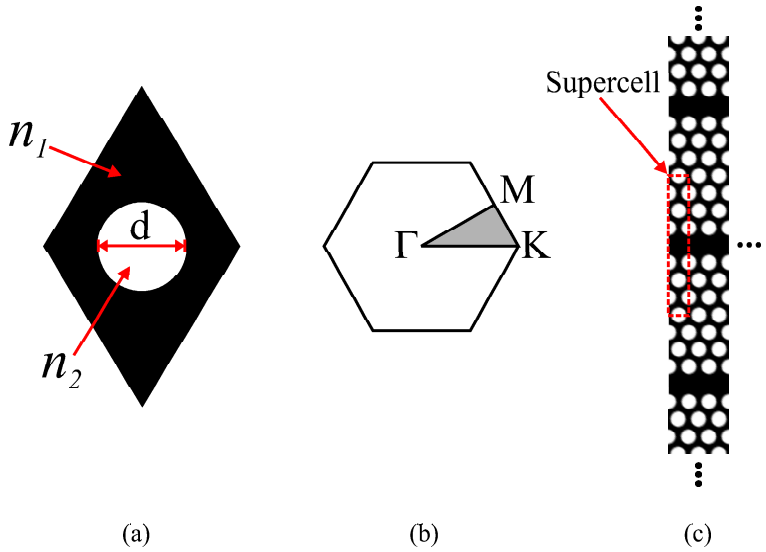

Figure 2.1: (a) Simple cell in real space with a hole of diameter d and refractive index n_2 placed in a dielectric with index n_1. (b) The simple cell in k-space and the irreducible Brillouin-zone (gray) with the high-symmetry points Γ, M, and K. (c) Schematic of the structure created from the supercell (dotted red) repeated infinitely in space for the calculation of the band diagram for a photonic crystal waveguide.

refs. [14,16,17]. The plane-wave expansion method operates in k-space (reciprocal-space), which is a Fourier transform of the real space, whereby solutions formed by combinations of plane-waves can be described as Fourier expansion series, which make calculations less cumbersome. In this way, solutions ω to eq. (2.14) are found as a function of the wavevector $\mathbf{k}$.

As an example, a perfect photonic crystal structure can in real-space be described using a simple cell as shown in fig. 2.1(a). This cell is repeated infinitely in space to create a periodic structure of circular holes with index n_2 placed in a triangular lattice in the material with index n_1. The modal field distribution and the dispersion relation $\omega(\mathrm{k})$ for the structure can easily be found and analyzed by applying the plane-wave expansion method to the simple cell. Due to symmetry of the simple cell, solutions to eq. (2.14) are typically sought along the high-symmetry points Γ, M, and K in k-space of the irreducible Brillouin-zone as sketched in gray in fig. 2.1(b).

To find the solutions of a photonic crystal containing defects a so-called *supercell* approximation is adopted that defines a supercell of $M \times N$ repeated simple cells with the defect contained in each supercell. The supercell is repeated in

space as depicted in fig. 2.1(c) where a structure for calculating the modes for a photonic crystal waveguide is set up. The waveguide is defined by a line-defect in the triangular lattice and solutions to eq. (2.14) are sought along the line-defect in nearest-neighbor direction of the crystal (ΓK-direction of the supercell in k-space). In this way, the photonic crystal waveguide is approximated by a structure with repeated waveguide cores. Therefore, in order to give accurate and converged results, the supercell should be large enough for the modes of the repeated waveguide cores (or other types of defects) to be uncoupled. In practice, a supercell of size 1×11 has been found to be an appropriate choice for calculating the modes of a photonic crystal waveguide (see Appendix A).

The software used in this thesis for calculating the dispersion relations for photonic crystals is the freely-available "MIT Photonic-Bands" (MPB) [16], which can be downloaded from the internet [18]. MPB is a full-vectorial eigenmode solver of Maxwell's equations and computes the eigenmodes with periodic boundary conditions by utilizing a preconditioned conjugate-gradient minimization of the block Rayleigh quotient in a plane wave basis [16]. The use of the *MPB* package will be presented in chapter 3.

2.2.2 Finite-Difference Time-Domain Method

Apart from knowing *which* frequencies that are allowed in the PhC it is essential for a practical implementation to know *how* the electromagnetic fields propagate through time and space. For this purpose, the Finite-Difference Time-Domain (FDTD) scheme is very useful and has found widespread use in the modelling of PhCs as it is very flexible concerning structure geometries and can handle large index variations [19].

By taking the curl, eq. (2.9) can be rewritten as [20]:

$$\nabla \times (\nabla \times \mathbf{H}(\mathbf{r},t)) = -\mu_0 \varepsilon(\mathbf{r}) \frac{\partial^2 \mathbf{H}(\mathbf{r},t)}{\partial t^2} \tag{2.16}$$

which is identical to

$$\nabla^2 \mathbf{H}(\mathbf{r},t) = \mu_0 \varepsilon(\mathbf{r}) \frac{\partial^2 \mathbf{H}(\mathbf{r},t)}{\partial t^2} \tag{2.17}$$

as $\nabla \cdot \mathbf{H} = 0$.

This equation is a wavevector equation, which may be solved to find the magnetic field distribution in time and space in the dielectric structure described by $\varepsilon(\mathbf{r})$. A similar derivation can be performed for the electric field. For a magnetic field having only field-components *in* the plane of the photonic crystal (x and y) the wavevector equation (2.17) can be rewritten in Cartesian coordinates as

$$\frac{\partial^2 \mathbf{H}(x,y)}{\partial x^2} + \frac{\partial^2 \mathbf{H}(x,y)}{\partial y^2} = \mu_0 \varepsilon(x,y) \frac{\partial^2 \mathbf{H}(x,y,t)}{\partial t^2} \tag{2.18}$$

Equation (2.18) is now discretized in a simple lattice, where the space and time points are separated by the basic units Δs and Δt, respectively. The indices of the lattice are labelled by i,j for space and n for time so that $\mathbf{H}(x, y, t) \rightarrow H(i\Delta\mathrm{s}, \mathrm{j}\Delta\mathrm{s}, \mathrm{n}\Delta\mathrm{t}) \rightarrow H^{\mathrm{n}}_{\mathrm{i,j}}$, which points in the z-direction. The derivatives of eq. (2.18) taken in each of the lattice points are approximated by a simple centered-difference, which gives the finite difference equation

$$\frac{H^n_{i+1,j} - 2H^n_{i,j} + H^n_{i-1,j}}{(\Delta s)^2} + \frac{H^n_{i,j+1} - 2H^n_{i,j} + H^n_{i,j-1}}{(\Delta s)^2} = \mu_0(\varepsilon_{ij}) \frac{H^{n+1}_{i,j} - 2H^n_{i,j} + H^{n-1}_{i,j}}{(\Delta t)^2} \tag{2.19}$$

Equation (2.19) can be used to determine the future component $H^{n+1}_{i,j}$ for a known initial vector field typically set to have a Gaussian distribution. Typically, only fields at specific positions for all times are kept for the final analysis of the PhC. At the boundaries of the structure where $i+1$ and $j+1$ are not defined, a chosen set of boundary conditions can be applied. Very often a perfectly matched layer (PML), which absorbs all light at the boundaries, is used.

The FDTD scheme have been implemented in a commercially available software tool called *CrystalWave*, which was developed in the scope of the IST PICCO project by the company Photon Design [21]. The software is based on the ONYX-2 version of the FDTD algorithm developed by A. Ward and J. Pendry [22] as the basic FORTRAN code. Improvements, have been made to the code by employing newly developed PML boundary conditions by Andrei Lavrinenko [23, 24]. The following chapter will present how CrystalWave can be used to get qualitative information about PhC components.

Chapter 3

Numerical Modelling of the Photonic Crystal Waveguide

Being in a fast-moving research field governed by economics it is of high importance to have access to accurate and effective modelling tools in order to foresee, understand, and optimize the performance of nanophotonic components to be fabricated. The "MIT Photonic Bands" [16,18] and the "CrystalWave" [21] software packages have been used in the project to simulate the behavior of photonic crystal components and will be applied in this chapter to bring forward the fundamental properties of *planar* photonic crystal waveguides.

3.1 Material Platform in Focus

As briefly presented in chapter 1, photonic crystals can be realized in many different ways depending on the application in mind, the choice of material, the needed simplicity of the fabrication, the need for integration with other electric/optic circuits etc.. This thesis will focus on 2D photonic crystals fabricated in a silicon-on-insulator (SOI) material having a ∼220 nm or ∼340 nm thick single-crystalline silicon layer placed on a 1 μm thick silica layer[1]. For the remaining of this thesis, if nothing else is mentioned, the PhC structures are realized as described in the following and sketched in fig. 3.1. The PhC structures are defined in the top silicon layer by holes arranged in a triangular lattice with lattice constant $\Lambda \approx 400$ nm. The diameter D of the holes are typically in the range $D/\Lambda = 0.5 - 0.8$. The value of these fundamental parameters of the PhC are chosen with respect to the needed functionality and operational wavelength region of the PhC component. Waveguides are carved out by removing one row of holes in the nearest-neighbor direction of the lattice (ΓK-direction in k-space, see fig. 2.1). In this way, light is

[1] The SOI wafers are bought from the company SOITEC, http://www.soitec.com/. For details and issues on the fabrication of SOI wafers see e.g. ref. [25].

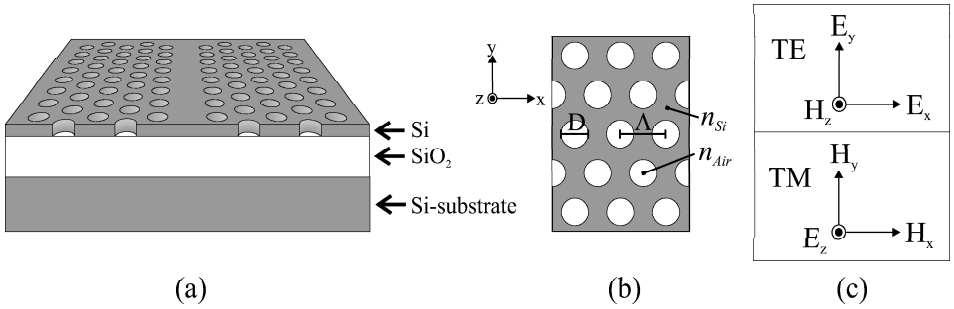

Figure 3.1: (a) Sketch of the planar photonic crystal slab configuration in focus in this thesis. (b) The photonic crystal is defined by air holes of diameter D and index $n_{air} = 1$ arranged in a triangular lattice with lattice constant Λ in silicon with index $n_{si} = 3.476$. (c) Definitions of transverse electric (TE) and transverse magnetic (TM) mode.

confined to the top silicon layer by total-internal-reflection due to the high index difference between the silicon core and the air/silica claddings and can be confined in-plane by the PBG arising from the PhC.

The modal solutions to equation (2.14) for a 2D PhC structure can be classified into two non-interacting polarizations [14, 26, 27] as sketched in fig. 3.1(c) for a PhC defined in the xy-plane:

Transverse electric (TE) polarization: $\mathbf{E} = (E_x, E_y, 0)$ and $\mathbf{H} = (0, 0, H_z)$
The electric field, and *only* the electric field, has field components in the xy-plane.

Transverse magnetic (TM) polarization: $\mathbf{H} = (H_x, H_y, 0)$ and $\mathbf{E} = (0, 0, E_z)$
The magnetic field, and *only* the magnetic field, has field components in the xy-plane.

However, because of the finite height of the PhC slab and, hence, lack of translational symmetry in the vertical direction modes are not purely TE or TM polarized in the fabricated structures. Instead, if the vertical claddings of the slab are identical, polarizations can be classified according to whether they are even or odd with respect to reflections through a plane bisecting the core slab. These even and odd modes do, however, have strong similarities with TE- and TM-modes, respectively. Therefore, they are often referred to as being TE- and TM-like. If the claddings in the vertical direction are different as e.g. is the case for the SOI structure polarization mixing occurs. In this thesis, however, I will keep it simple and refer to modes as being TE- or TM-polarized due to a high degree of similarity with *pure* TE- and TM- modes.

The advantages of using the SOI platform are the simplicity in the fabrication of PhC structures and the mechanical robustness of the components it offers.

Though, as will be discussed in a later section, the out-of-plane losses may be severe and limit the useful bandwidth of the PhC components. To overcome this challenge, it is convenient to remove the underlying silica layer in an etch process and, thereby, increase the leakage-free bandwidth (as presented later). Moreover, it increases the degree of vertical symmetry decreasing the TE-/TM- mode coupling. However, such a membrane configuration may have troubles with mechanical stability, it adds more process steps to the fabrication procedure, and makes it difficult to realize e.g. electrical contacts on top of the PhC but isolated from the core material[2]. Another widely discussed configuration is the so-called Anti-Resonant-Reflection-Optical-Waveguide (ARROW) configuration [28–30] in which the cladding beneath the core layer is deliberately chosen to provide high reflectance by the principle of interference similar to a Fabry-Perot resonator, which has broad reflecting windows on antiresonant wavelengths and sharp transmission peaks on resonant wavelengths. Though, the ARROW principle may offer near-zero out-of-plane losses in broad wavelength ranges it may be challenging to implement in a cost-effective way into a fabrication line of conventional electronics and photonics.

3.2 Modelling with MIT Photonic Bands

This section will apply the MIT Photonic Bands (MPB) to model and present some of the basic properties that arise when a line-defect is introduced in the PhC and forms a planar photonic crystal *waveguide*, which has been in focus in this project. For discussions and results on another important group of PhC components utilizing photonic crystal cavities, see e.g. refs. [31–37]. Details regarding the modelling software and parameters applied in this thesis can be found in ref. [38] and Appendix A.

3.2.1 The Perfect Photonic Crystal

Figure 3.2 shows the dispersion relation calculated for the TE (red) and TM (blue) polarization along the symmetry points Γ, M, K for a perfect 2D PhC structure with a hole diameter D=0.90Λ. Due to the scalability of Maxwell's equations the allowed frequencies ω within the PhC are normally plotted norma-lized to the lattice pitch Λ. It is seen that a large bandgap exists from 0.30-0.49 Λ/λ for the TE polarization (light-gray) wherein no modes are present. For the TM polarization a somewhat smaller bandgap appears from Λ/λ=0.40-0.44 (dark-gray). It overlaps with the TE bandgap and, thus, leads to a complete omnidirectional bandgap in this frequency range. However, it is well-known [14] that the PBGs for the TE- and TM-polarization are governed by different conditions. For this reason, it is difficult to fabricate PhC components with large and overlapping PBGs for both

[2]This would actually be needed if an optical modulator exploiting slow-light and strain-induced χ^2 effects in PhC waveguides were to be realized as presented in ref. [7].

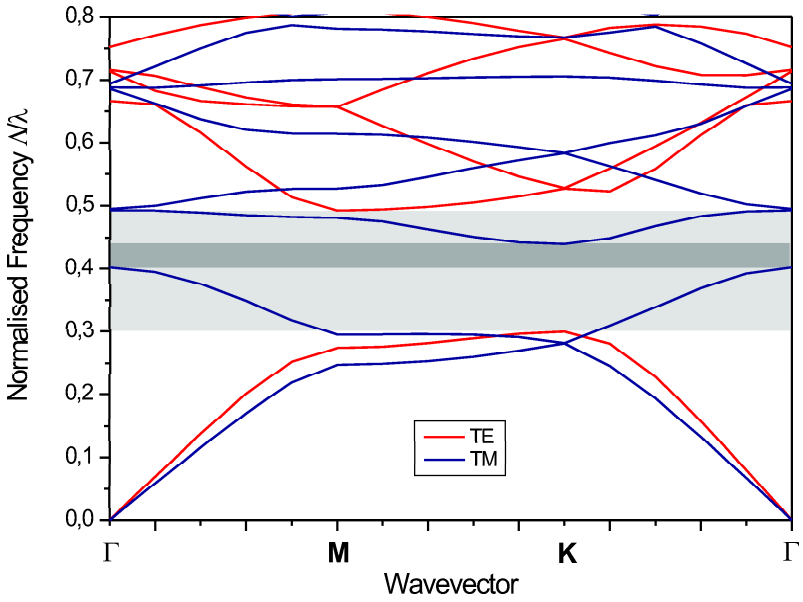

Figure 3.2: 2D band diagram for the TE (red) and TM (blue) polarization in a perfect photonic crystal with D/Λ=0.90. A large PBG is present for the TE-polarization (light-gray) and a narrow PBG (dark-gray) for the TM-polarization.

polarizations in the wavelength regions of interest and a choice of polarization is typically made. Here, the focus is on PhC components optimized for TE polarized light as the slab configuration presented in section 3.1 is known to support a large PBG for the TE polarization [14, 39]. Moreover, the TM polarization is more sensitive to sidewall roughness in the structure [40] leading to higher losses. Examples of different configurations with large bandgaps for either TE- or TM-polarized light can be found in e.g. ref. [41].

3.2.2 The Photonic Crystal Waveguide

In itself, the perfect PhC may be an interesting structure for the realization of e.g. optical mirrors [42], collimators [43], and superprisms [44,45]. However, introducing defects in the PhC may lead to defect states in the PBG that have novel properties and open for the realization of new and compact waveguide devices.

The photonic crystal waveguide (PhCW) is formed by introducing a line-defect into the PhC. Figure 3.3(a) shows the 2D band diagram for the TE-polarization of a so-called *W1* PhCW where *one* row of holes has been removed along the nearest-neighbor direction of the crystal. The supercell used in the calculation is shown in the inset of the figure. The calculated modes have been projected along the ΓK-direction of the triangular lattice [46] and shown are only the 30 lowest-frequency solutions, which are an appropriate number to find the presence of the lowest bandgap from Λ/λ=0.226-0.342. The gray regions in the figure represent continuum of projected slab modes, which have their field distributions mainly in the PhC cladding and are not confined to the line-defect. The H_z field distributions for $k\Lambda/2\pi$=0.5 of two such slab modes are shown in frame ***iv*** and ***ix*** of fig. 3.3(b). The slab bands would be the only ones present if the line-defect was omitted. By introducing the line-defect 7 defect states are created. The three modes (dotted) lying below the first slab band are purely index-guided modes and the four modes (solid) located in the PBG are addressed as PBG-modes. *Even* modes are colored in red and are symmetrical under mirroring through a plane oriented parallel to and bisecting the waveguide core and *odd* modes are colored in blue and are asymmetrical under a similar mirroring.

The fundamental PBG mode with an even field distribution as shown in frame *v* has a large bandwidth in the PBG running from ∼0.23-∼0.31 Λ/λ and its field distribution has a large overlap with that of an even mode in a ridge waveguide. This makes the fundamental PBG mode attractive and easy to couple to, in contrast to the higher-order PBG modes (modes ***vi***, ***vii***, and ***viii***), which have narrow bandwidths and/or are odd.

3.2.3 Relative Hole Diameter

To obtain a large PBG it is important to choose an optimal value of the relative diameter D/Λ. However, in planar PhCWs it is not possible to obtain leakage free transmission for the fundamental PBG mode in the full available PBG due

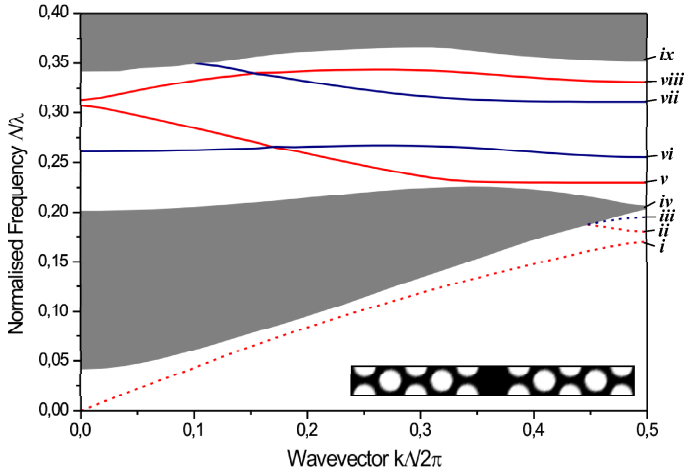

(a)

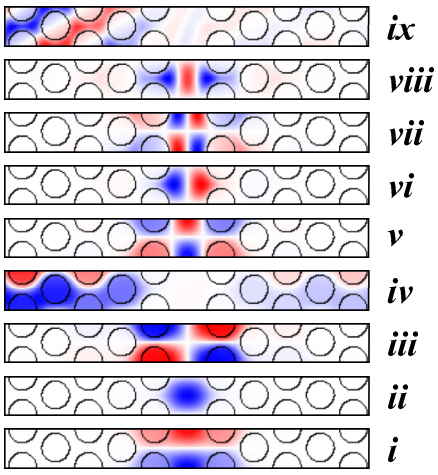

(b)

Figure 3.3: (a) 2D band diagram for the TE-polarization for a photonic crystal waveguide with D/Λ=0.725. Slab modes are shown in shaded gray, index-guided modes are shown dotted, and PBG modes are shown in solid. Even modes with respect to the center of the waveguide are in red and odd modes are in blue. Inset shows the supercell used in the calculation. (b) H_z field distributions of the modes at kΛ/2π=0.5.

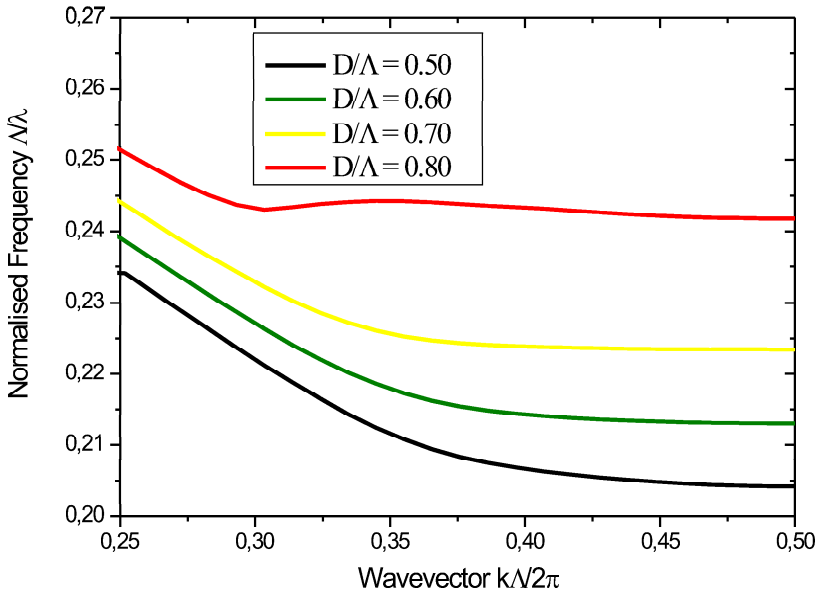

Figure 3.4: The movement of the fundamental PBG mode when varying the relative hole diameter D/Λ.

to out-of-plane scattering (as will be discussed later in this section). Therefore, it is important to focus on the absolute position of the fundamental mode instead of having a maximum PBG as design goal. Figure 3.4 shows the movement of the fundamental PBG mode when changing the relative diameter of the holes. Increasing the relative hole diameter moves the mode and the cutoff to higher frequencies. If the relative diameter becomes too large the mode interacts with the slab band as seen for $D/\Lambda = 0.8$. This may lead to degeneracy of the mode. The relative movement of the fundamental even and odd PBG modes may also be of concern, as coupling between such modes may occur in real samples. The relative placement of these should therefore be addressed in the design phase.

In the fabrication of PhCWs it is important that the fabricated hole dia-meters turn out so that the features of the fundamental mode are in an appropriate frequency window. A thorough investigation should be made for the exact slab configuration available, i.e. 3D calculations for the exact core thickness and the proper cladding conditions should be made prior to fabrication. Knowledge of

how the modes move with the relative hole diameter as sketched in fig. 3.4 can be helpful in an eventual post-processing step of the PhC component. Typically, the holes can be made larger by oxidizing the sample as presented in [47] and, hence, shift the cutoff of the fundamental mode to higher frequencies.

3.2.4 The Slab Configuration

Figure 3.5 shows the 3D band diagram for a W1 PhCW defined by holes of diameter $D/\Lambda = 0.725$ in a 340 nm thick silicon layer on top of 1 μm silica and with air above. The lattice pitch $\Lambda = 400$ nm. A large similarity between the present modes is found when comparing the 3D band diagram to the 2D band diagram shown in fig. 3.3. Basically, the only difference is a frequency shift of the modes to higher frequencies. This arises when having a finite-height silicon core with the modes feeling the low-index claddings above and below the core reducing the effective mode indices and increases their energies. Decreasing the core thickness will move the modes even higher up in frequency.

For the planar PhC slab, restrictions are put to whether modes are confined vertically or not. For the air-silicon-silica (the SOI) configuration only modes located below the light-gray region in fig. 3.5, defined by the silica-line $\frac{\omega}{c} = \frac{k}{n_{silica}}$, may be guided with no loss. Modes (or part of the modes) located above the silica-line are resonant in the vertical direction and can couple to modes in the silica cladding. They are, however, still guided along the PhCW but are (very) lossy as will be presented later. It is seen that only small fractions of the PBG-modes are below the silica-line and, thus, leakage-free guidance can only be obtained in very narrow bandwidths. For an air-silicon-air (the membrane) configuration modes that are lossy in the vertical direction are determined by the light-line shown as the black line in fig. 3.5. The inset sketches the increase in bandwidth for leakage-free guidance of the fundamental PBG mode when going from the SOI slab to the membrane configuration. Here, the gain is in practice going from zero bandwidth to ∼50 nm. For this reason, the membrane configuration has attracted a lot of attention for the realization of low-loss PhCWs.

3.2.5 Waveguide Width

Changing the width of the PhCW is a handle for controlling the properties of the fundamental PBG mode. The width of the PhCW is defined as the center-to-center distance between the holes adjacent to the waveguide core. Figure 3.6(a) shows how the fundamental PBG mode in 2D is greatly influenced by decreasing the waveguide width. The red curve represents the mode for a conventional W1 PhCW with $D/\Lambda = 0.60$ and Wx curves are for waveguides with width x compared to the width of a W1 PhCW. The effect of changing the waveguide width stems from a change in the effective index of the core region and it is apparent that a narrower core moves the fundamental mode up in frequency. This is of no surprise as the effective mode-index is reduced. However, for a width around 0.75 the

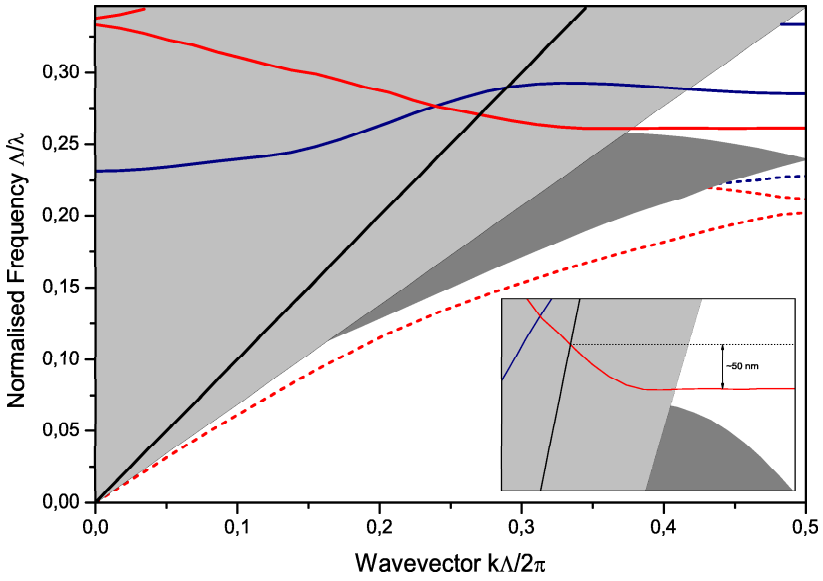

Figure 3.5: 3D band diagram for a W1 PhCW with D/Λ=0.725. The PBG (solid) and the index-guided modes (dotted) are divided into even (red) and odd (blue) modes. The slab-band is shown as the dark-gray region. The parts of the modes located above the silica-line in the light-gray region are not confined vertically with respect to the silica cladding. The black-line represents the light-line. Inset shows the practical difference in useful bandwidth between having a SOI or a membrane structure.

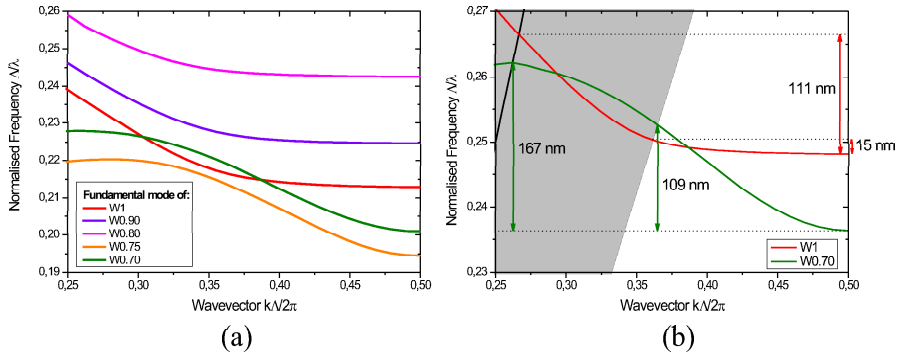

Figure 3.6: (a) 2D band diagram for the TE-polarization in PhCWs with D/Λ=0.60 and different widths Wx (where x notes the width compared to a conventional W1 PhCW). (b) 3D band diagram for the fundamental mode in a W1 (red) and W0.70 (green) PhCW. Gray region represents modes allowed in the silica cladding. Black line represents the light-line.

fundamental mode moves up into the upper slab band and a new mode is pulled up from the lower slab band. Note that the field distribution of the W0.70 mode is different from the conventional W1 PBG mode and has a field distribution more similar to the index-guided modes below the lower slab band. Figure 3.6(b) plots the dispersion relation in 3D for the fundamental mode for the W1 (red) and W0.70 (green) PhCW. The gray region corresponds to the continuum of modes in the silica cladding and the black line represents the light-line. It is seen that the leakage-free bandwidth of the PhCW in a membrane configuration is increased by ∼50 nm from ∼111 nm to ∼167 nm when going from the W1 PhCW to the W0.70 PhCW. Having a SOI configuration the increase is even more dramatic going from ∼15 nm to ∼109 nm. This is a general trend for all values of D/Λ. Therefore, if large-bandwidth low-loss PhCWs in the SOI configuration are needed it may be favorable to use W0.70 waveguides instead of the conventional W1 waveguides. Note, however that the dispersion properties of the W0.70 PhCW are very different from that of the W1 PhCW, i.e. slow-light phenomena as presented in the next section may not be obtainable for a W0.70 PhCW.

3.2.6 The Slow-Light Phenomenon

It is well-known that various classical nonlinear effects in optical waveguides can be enhanced by a small group velocity v_g of light, since the light-matter interaction increases linearly with decreasing group velocity [48–51]. For the traditional ridge or slab waveguides usually considered in integrated optics, a nonlinear mode

dispersion, which leads to a small value of the group velocity, is a highly exotic phenomenon. However, photonic crystal waveguides deliver very large group index dispersion combined with extremely low values of the group velocity at the cutoff wavelength for the fundamental PBG mode.

Basically, the fundamental PBG mode in a W1 PhCW has two regimes of operation: a very broad regime, where the slope of the dispersion relation is linear (the linear regime) and a narrow and curved regime (the slow-light regime), where the slope and, thus, the group velocity approaches zero at the Brillouin-zone end. Figure 3.7(a) plots the 2D band for the fundamental PBG mode highlighting (arbitrarily chosen) one frequency in the linear regime (green), one frequency in the slow-light regime (red), and one frequency on the border between these regimes (yellow). The slope $\delta\omega/\delta k$ equal to the group velocity v_g is plotted in fig. 3.7(b) highlighting again the three frequencies. In the linear region (green) the group velocity v_g is approximately one-fourth of what it would be in vacuum corresponding nicely to the effective index of an index-guided mode in an conventional ridge waveguide. The field distribution H_z in the linear regime (green) is shown in fig. 3.7(c) and shows that the mode is nicely confined to the core and, indeed, have similarities with an index-guided mode. Approa-ching the slow-light region (yellow) the group velocity starts to decrease and the field penetrates more into the PhC cladding. In the slow-light regime near the Brillouin-zone end (red) the group velocity comes close to zero and the mode penetrates strongly into the PhC. This slow-light phenomenon in PhCWs arises from the periodicity of the micro-structured waveguide cladding and makes the PhCW a very interesting candidate for e.g. optical buffering [52], switching [53], dispersion control [54, 55], lasing [36] and non-linear light/matter effects [7] in nanophotonic circuits. The terms "index-guided" and "gap-guided" is often used for the fundamental PBG mode in the linear- and slow-light regime, respectively, to distinguish its very different mode profiles as presented here.

3.2.7 Perturbation of the Photonic Crystal Waveguide

Though, slow-light in a PhCW may be an attractive phenomenon to exploit there are some challenges to overcome. First of all, the slow-modes in PhCWs have by nature a very limited bandwidth as the numerical value of the group velocity is proportional to the slope of the dispersion relation; thus, a numerical low group velocity comes with a numerical low slope and, hence, a small bandwidth. In practice, this makes (extremely) slow-light in the W1 PhCW a single frequency phenomenon, which may be challenging for practical implementations. Next, slow-modes may be difficult to couple to from a conventional ridge waveguide due to a large impedance mismatch [56–60], and, finally, the propagation loss of slow-light modes may be dramatically increased compared to light travelling at 'normal' ($c/4$ for silicon) speeds as the loss may have a $1/v_g$ or even a $1/v_g^2$ dependency [61, 62].

The knowledge of the field distributions shown in fig. 3.7(c) may be exploited to shape the slope of the dispersion relation for the fundamental PBG mode in

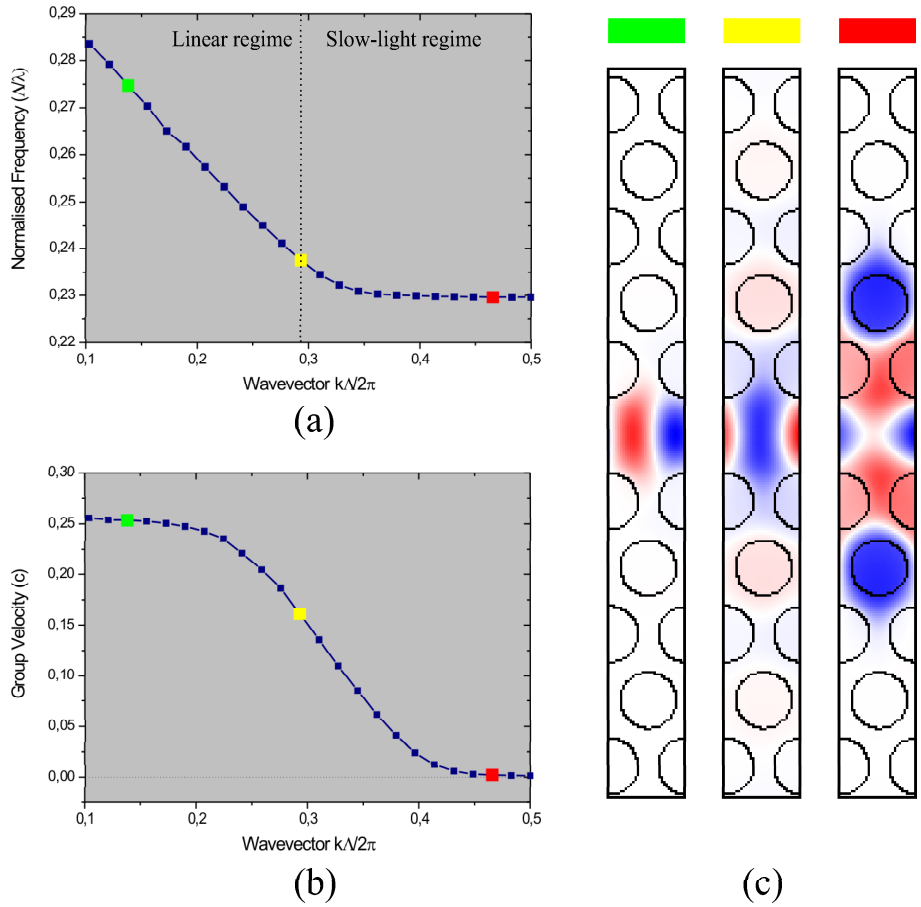

Figure 3.7: (a) Fundamental PBG mode for TE-polarization. Dotted line sketches the two different regimes of the PhCW distinguished by the field distributions. (b) The group velocity $v_g = \delta\omega/\delta k$ for the mode. (c) H_z field distributions for the fundamental PBG mode at the three highlighted frequencies (green, yellow, red).

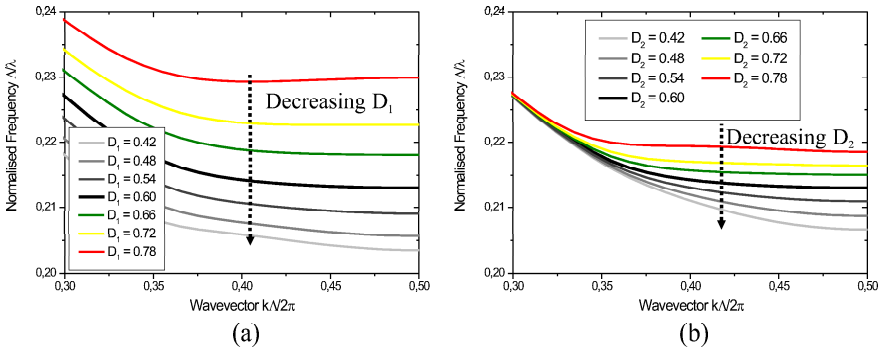

Figure 3.8: Effect on the fundamental PBG TE-mode in a W1 PhCW with $D = 0.60\Lambda$ when changing the diameter (a) D_1 of the first row of holes and (b) D_2 of the second row of holes.

the PhCW. One goal-criteria, as pursued in the following, could be to obtain constant, high-but-non-extreme group velocities in a useful bandwidth. In this way, the waveguide would support an increased light/matter interaction over a useful bandwidth for e.g. non-linear effects or buffering with vanishing (zero) third-order dispersion.

Figure 3.8(a) shows the effect on the fundamental PBG mode when the relative diameter of the first row of holes (borderholes) is changed. The black curve represents the situation when no change of the borderholes have been made, i.e. the mode in a conventional W1 PhCW. It can be seen that if the size of the borderholes is decreased the mode shifts down in frequency and, conversely, an increase in the borderhole size will shift the mode up in frequency. This frequency shift occurs without affecting the slab modes dramatically and can be understood by studying the field distribution of the mode shown in fig. 3.7(c): in the linear *and* in the slow-light regime the mode 'feels' the borderholes to a large extent and, hence, is affected when the refractive index is changed locally in these. This feature can e.g. be exploited to realize PhC drop filters as will be demonstrated in chapter 6. It is noted the slope in the slow-light regime increases numerically when the borderholes are decreased in size, which is equal to a decrease in group velocity.

Turning back to the field distributions in fig. 3.7(c) it is obvious that in the slow-light regime and only here the mode penetrates beyond the first row of holes and into the PhC cladding. With this in mind, the behavior of the mode shown in fig. 3.8(b) when changing only the size of the *second* row of holes can be understood. Again, the black curve corresponds to the situation when no change is made and as before the perturbation does only affect the slab-modes slightly. Increasing the diameter of the second row of holes pushes the *tail* of the mode up in frequency and

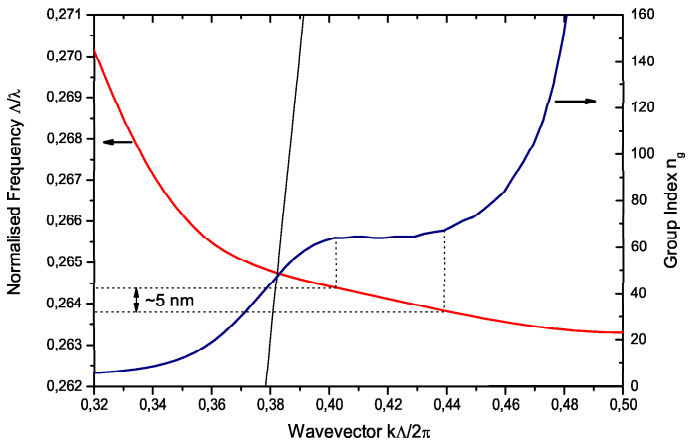

Figure 3.9: 3D band diagram of the fundamental TE-mode (red) of a W1 PhCW with D/Λ=0.60 and perturbed first (**-40** nm) and second (**+25** nm) row of holes and the corresponding group index curve (blue). The black line indicates the silica-line.

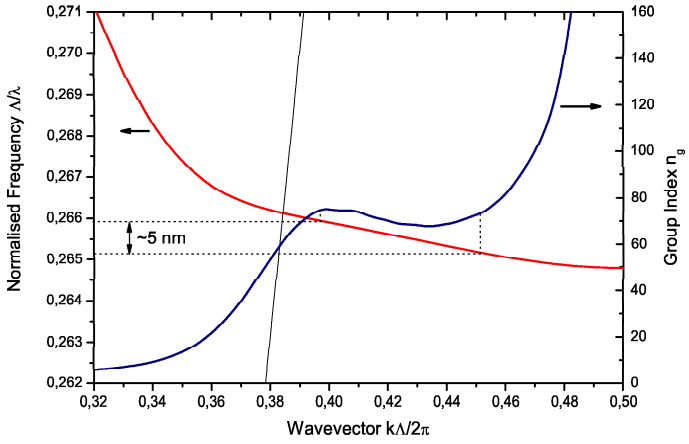

Figure 3.10: 3D band diagram of the fundamental TE-mode (red) of a W1 PhCW with D/Λ=0.60 and perturbed first (**-30** nm) and second (**+40** nm) row of holes and the corresponding group index curve (blue). The black line indicates the silica-line.

decreasing the diameter pulls it down. In both cases the part of the mode located in the linear-regime is unaffected. Combining the knowledge from figs. 3.8(a) and (b) it is possible to realize the PhCW with a constant and high-but-non-extreme group index for the fundamental PBG mode in a useful bandwidth. Calculating the group index n_g for the situation where the borderholes are decreased to D_1/Λ=0.48 reveals that the value in a ∼10 nm bandwidth is around 30, which is a factor of ∼8 higher than in the linear regime. This value can, however, be increased further by increasing the diameter of the second row of holes and, as seen in fig. 3.8(b), move the tail of the mode up in frequency and, hence, decrease the slope. Figure 3.9 shows an example where the borderholes and the second row of holes have been decreased/increased by 40/25 nm, respectively, from an initial diameter of 240 nm. The corresponding group index is also plotted and shows that the mode has a ∼5 nm bandwidth below the silica-line where the group index is ∼65; a factor of ∼13 higher than in conventional ridge waveguides. The high and constant group index may be decreased/increased leading to a larger/smaller bandwidth by changing the perturbation parameters of the borderholes and the second row of holes.

Figure 3.10 shows another example where the borderholes and the second row of holes have been changed by -30/+40 nm, respectively, from their initial diameter of 240 nm. The obtained group index plateau is a bit higher in value but located at higher frequencies. However, the group index plateau is not as flat as the previous

example, thus, the perturbation parameters could be optimized if a constant level is the goal. On the contrary, a curved group index profile as this could be this used in a dispersion compensating component [55].

Conclusively, by changing the diameter of the borderholes and the second row of holes it is possible to tailor the dispersion properties of the PhCW. These 'handles' may come in handy and offer more degrees of freedom than previous attempts of tailoring the dispersion by changing the waveguide width or utilizing coupled or linearly chirped PhCWs [54, 55]. Arguably, all tricks may be combined to obtain the properties needed in a proper bandwidth. In chapter 6 experimental results on perturbed PhCWs will be presented.

3.3 Modelling with CrystalWave

As presented in the previous section, the plane-wave expansion method can be used to gain knowledge of the physics governing the properties of the photonic crystal waveguide. However, the method is restricted to model simple configurations and does not provide a *quantitative* description of the fields propagation through the photonic crystal structure as is needed for practical implementations. The Finite-Difference Time-Domain scheme can be utilized to get a quantitative description of (more or less) arbitrary geometries. This section will present the utilization of the FDTD scheme for modelling the broadband performance of photonic crystal structures as well as their response for narrow-width pulses. All transmission spectra throughout the section have been obtained by using the *CrystalWave* software [21] for which details regarding the modelling parameters can be found in Appendix B and refs. [24, 63].

3.3.1 Broadband Characteristics of PhCWs

Figure 3.11(left) shows a 2D band diagram for a PhCW with $D = 0.75\Lambda$ plotted with a 2D FDTD simulation (right) of TE-polarized light propagating through a 10 μm long W1 PhCW with $D = 0.75\Lambda$. No fitting procedures have been applied to any of the plots and show an ambiguous frequency correlation between the band diagram and the transmission spectrum as all major features in the transmission spectrum are directly relatable to features in the band diagram. The index-guided modes (dotted) below the slab band do provide an opportunity to have high transmission up to a frequency of Λ/λ=0.19. The absence of transmission from Λ/λ=0.19-0.23 is due to the lack of guided modes and/or presence only of slab modes. In the frequency range Λ/λ=0.23-0.31 high transmission is observed that stems from the fundamental even PBG mode for which the low- and high-frequency cutoffs are nicely correlated between the two schemes. The small fringes in the transmission spectrum are due to Fabry-Perot oscillations occurring at the facets of the PhCW and transmission levels above unity may be due to instabilities in the perfectly matched layers of the FDTD scheme [23]. The transmission from Λ/λ=0.31-0.35 can be related to the higher order even mode. The

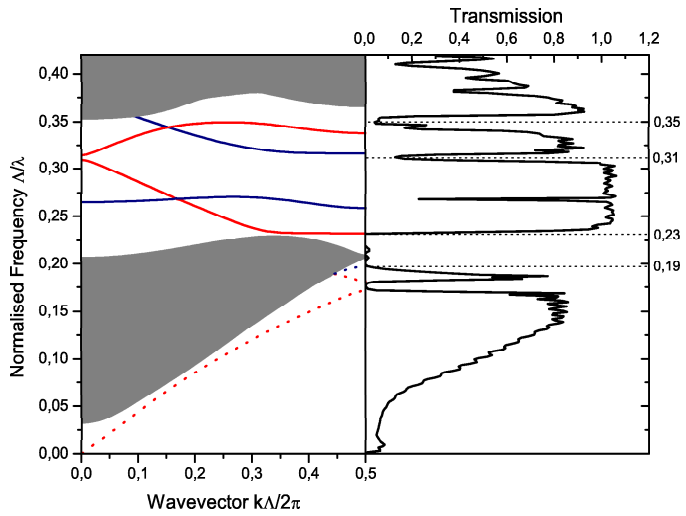

Figure 3.11: 2D band diagram (left) and 2D FDTD (right) simulation for TE-polarization in a 10 μm W1 PhCW with $D = 0.75\Lambda$. In the band diagram the PBG (solid) and index-guided (dotted) modes are divided into even (red) and odd (blue) modes. Slab-bands are shown in shaded gray.

dip in the transmission spectrum around 0.27 Λ/λ is (in theory) artificial and can be explained by a broken symmetry of the simulated structure when first-order finite-differences in the FDTD scheme are applied [24]. Therefore, numerically induced interactions between even and odd modes are un-avoidable and an artificial anti-crossing effect leads to the artificial mini stop-zone and, hence, the dip in the transmission spectrum where the odd mode crosses the fundamental PBG mode. Increasing the spatial resolution in the FDTD calculation will reduce the numerical coupling and the dip will eventually disappear. However, mode coupling between the fundamental even and odd mode in the PBG may occur in a real PhCW due to imperfections, such as roughness and irregularities [64]. Such mode coupling will lead to a dip in transmission due to poor coupling efficiency between the odd PBG mode and the fundamental even mode in a ridge waveguide normally used for routing light to and from the PhCW.

Figure 3.12 shows a zoom-in on the fundamental PBG mode of the 3D band diagram from fig. 3.5 plotted aside a 3D FDTD calculation for a 10 μm long W1 PhCW with $D = 0.725\Lambda$. A $\sim$1% frequency shift has been applied to the 3D FDTD spectrum to match the mode-cutoff to the *MPB* simulation. This shift may be explained by differences in the vertical conditions of the *MPB* calculation and the

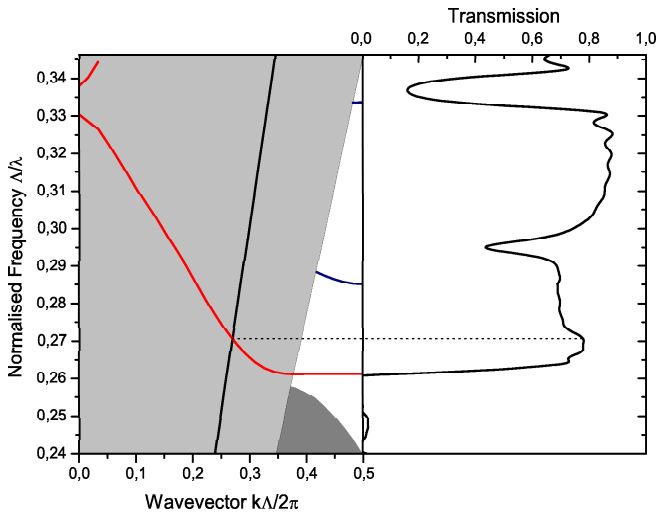

Figure 3.12: 3D band diagram (left) and 3D FDTD (right) simulation for TE-polarization in a 10 μm W1 PhCW with $D = 0.725\Lambda$. The light-gray region represents the continuum of modes allowed in the silica cladding layer and the black-line is the light-line. Grid spacing in the 3D FDTD is $\Lambda/24$, though the artificial dip around 0.29 Λ/λ is still present.

FDTD simulation and a mismatch in the applied calculation grids. Again, the figure displays a nice correlation between the band diagram and the transmission spectrum. Most of the fundamental mode is seen to be located above the silica-line in the light-gray region and, thus, is not confined vertically. However, as the waveguide is very short light is seen to be transmitted through the waveguide. The artificial anti-crossing effect is again seen as the dip in transmission around 0.295 Λ/λ. A small peak in transmission in nicely seen in the region where the fundamental mode goes below the light-line and, thus, does not leak to the air cladding (but only to the silica-cladding).

Figure 3.13 shows the normalised transmission spectra obtained from a 3D FDTD simulation (red) and an experimental measurement (black) of a 10 μm long W1 PhCW fabricated with $D/\Lambda = 0.7$. Due to uncertainties of the experimental parameters and the limited grid resolution in the 3D FDTD calculation, the 3D FDTD spectrum has been shifted $\sim$10 nm to match the calculated transmission cutoff to the measured spectrum. However, it is clearly seen that the 3D FDTD spectrum successfully explain the essential features of the measured spectrum as well as the actual transmission level. The deviations between the measured and

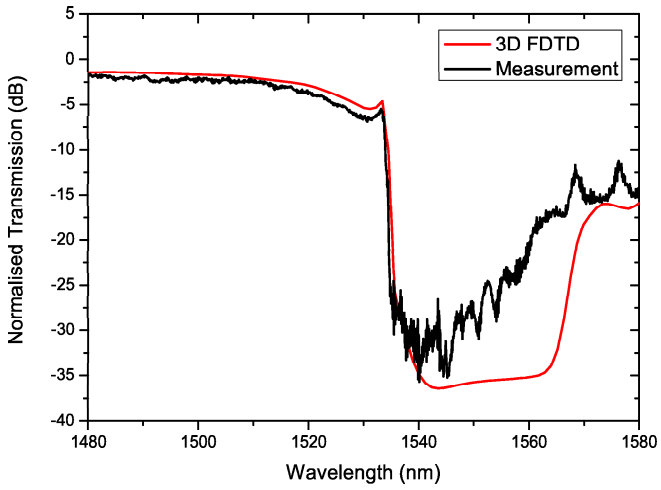

Figure 3.13: Comparison between a 3D FDTD simulation (red) and an experimental measurement (black) of a 10 μm long PhCW with $D/\Lambda = 280\text{nm}/400\text{nm} = 0.7$.

calculated spectrum after the cutoff is due to the presence of TM polarized light in the fabricated sample (arising from polarization mixing in the sample and/or the limited extinction ratio between TE and TM in the setup).

Having demonstrated the excellent correlation between the band diagram obtained by *MPB*, the transmission characteristics obtained from *CrystalWave*, and experimental measurements on a PhCW, the accuracy and reliability of the simulation tools are verified and these will be used to model various fabricated photonic crystal components as presented in chapter 6.

3.3.2 Narrow-Width Pulses in PhCWs

Alternatively, to model the *broadband* performance of the PhCW by applying a plane-wave excitor to the structure, it is possible to use a single-frequency excitor in *CrystalWave* to gain knowledge of the group index for light in the PhCW using the so-called Time-Of-Flight (TOF) method [34, 65–68]. The concept of utilizing the ToF method in *CrystalWave* has been developed by Andrei Lavrinenko [23] and is as follows: a narrow-width pulse centered around the wavelength of interest is launched into the PhCW from a butt-coupled ridge waveguide and the tracing of the pulse is performed by using two detector plates that are placed e.g. at the input and output ports of the PhCW. The dynamics of the pulse propagation through the detectors are recorded by storing the field values at the detector plates for all time steps. By determining the time when the top of the pulse passes the detectors, the time delay Δt for the pulse to travel from the input to the output detector can be found. Together with the known distance ΔL between the detectors, the group index can be calculated as

$$n_g = \frac{c}{v_g} = \frac{c\Delta t}{\Delta L}. \tag{3.1}$$

Figure 3.14 shows two adjacent and un-coupled PhCWs excited by two dipole exciters (yellow) placed in butt-coupled photonic wires. The excitor for the lower PhCW is centered around the cutoff of the fundamental PBG mode at 1715 nm and the upper excitor is centered around 1615 nm in the linear regime of the mode (refer to fig. 3.7 for $\Lambda = 400$ nm.). Here, the temporal widths of the pulses are chosen conveniently short but sufficiently small in spectral bandwidth to picturise a difference in time-of-flight between the two pulses. Clearly, the pulse centered around 1615 nm in the linear-regime of the PBG mode reaches the end of the PhCW before the pulse centered around the mode-cutoff in the slow-light regime. Thus, it travels with a higher group velocity. Figure 3.15(a) plots the fundamental PBG mode and marks the positions of the center-frequencies for three different pulses. Figures 3.15(b-d) show typical time-of-flight pictures of the electric field amplitude for 0.5 nm narrow pulses recorded at the input (blue) and output (red) detectors of a 30 μm long PhCW and centered around frequencies as given in fig. 3.15(a). Away from the cutoff wavelength (fig. 3.15(b)) the time-of-flight in the

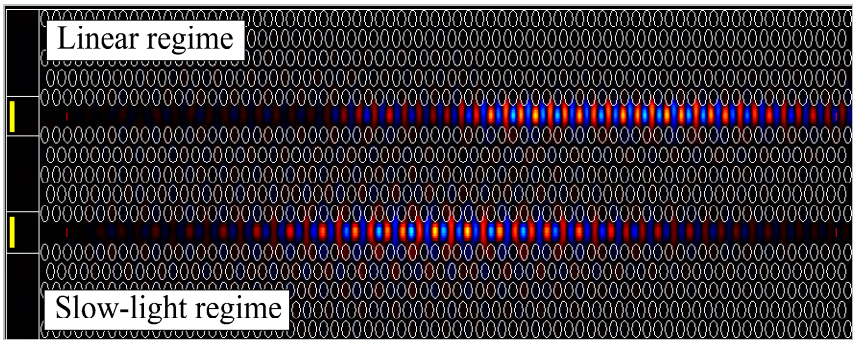

Figure 3.14: Snapshot of the 2D FDTD modelling of two TE-polarized pulses propagating through two identical PhCWs of length ∼30 μm. The upper pulse is centered around 1615 nm in the linear-regime of the PBG mode and the lower pulse is centered around the mode cutoff at 1715 nm.

waveguide can be found to $\Delta t = 0.5$ ps that leads to a group index using eq. (3.1):

$$n_g = \frac{3 \cdot 10^8 \frac{m}{s} \times 0.5ps}{30\mu m} = 5. \tag{3.2}$$

Closer to the cutoff wavelength represented by the situation in fig. 3.15(c) the time-of-flight is 3 ps and, hence, the group index can be found to approach 30. For the pulse centered around the cutoff wavelength of the fundamental mode the travelling time is $\Delta t = 15$ ps and the group index of the pulse is calculated to $n_g \approx 150$. This predicts that light is slowed down by a factor of ∼30 just before the cutoff wavelength compared to light in the linear-regime of the transmission band[3]. Moreover, the footprint of the high dispersion in the slow-light regime can be seen as the pulses in figs. 3.15(c)+(d) have broadened severely during their propagation through the waveguide. Experimental results on group index measurements will be presented in chapter 6.

[3]If the wavelength is chosen to match the exact cutoff wavelength and using an extremely narrow pulse it should be possible to calculate an extremely high group index. However, this would require an extreme amount of timesteps and loads of computer resources.

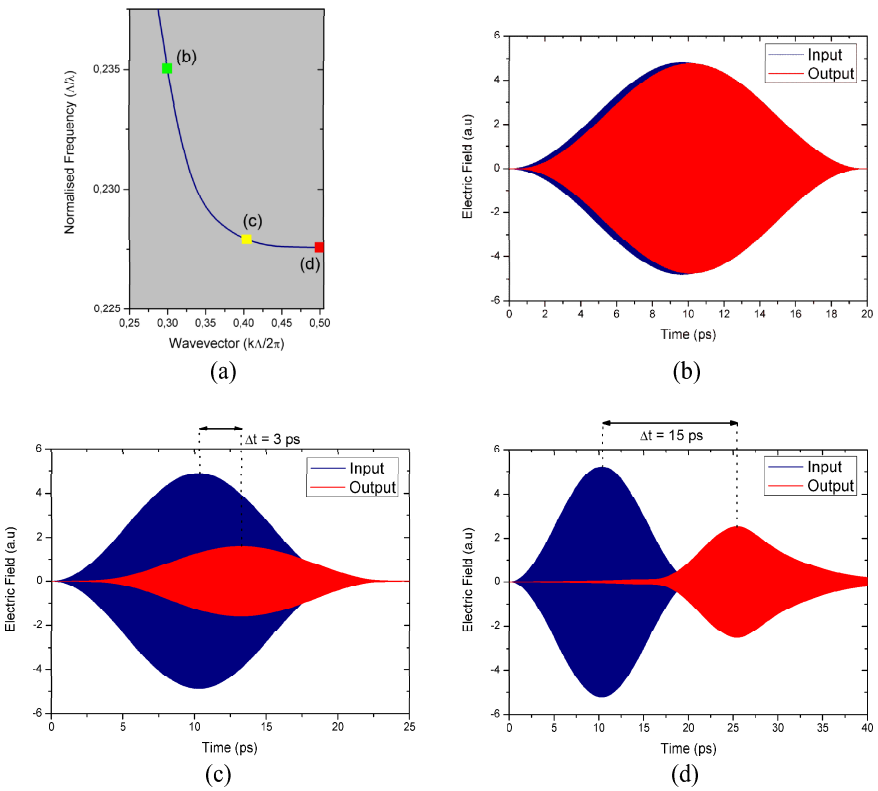

Figure 3.15: Typical 2D time-of-flight pictures of a 0.5 nm narrow TE-polarized impulse recorded at the input (blue) and the output (red) detectors for a 30 μm long PhCW with D/Λ=0.725, and located at the positions marked (b),(c),(d) on the fundamental mode plot in (a).

3.4 Summary

This chapter presented how the *MPB* and *CrystalWave* software packages can be applied to model the behavior of a photonic crystal waveguide realized in a SOI slab configuration. It was presented how the hole diameter and waveguide width affect the position of the fundamental even mode in the photonic bandgap. It was shown that a too large relative hole diameter will lead to an interaction between the fundamental bandgap mode and the lower slab band. The W0.7 waveguide with a core-width of 70% of the W1 waveguide was shown to be favorable to utilize to obtain a large low-loss bandwidth below the silica-line in the silicon-on-insulator slab. The fundamental mode was divided into two different regimes: a linear regime having an effective group index around 4-5 and a slow-light regime where there group index of the mode goes to infinity, i.e. the group velocity approaches zero. It was demonstrated how the knowledge of the field distribution for the fundamental photonic bandgap mode in the waveguide can be exploited to realize a photonic crystal waveguide having a narrow-but-useful wavelength region with a very high and constant group index that may be favorable in e.g. dispersion compensating and/or non-linear optical devices. The Finite-Difference Time-Domain scheme showed to be an excellent tool to obtain qualitative information that explains the behavior of fabricated photonic crystal waveguides and correlates to the band diagram of such calculated by using *MPB*. Moreover, *CrystalWave* makes it possible to investigate how narrow width pulses propagate in time and space through photonic crystal structures to obtain e.g. the group index of the waveguide.

Chapter 4

Design and Topology Optimization

In the field of photonic crystals, research has within the last decade mostly relied on an Edisonian design approach combining physical arguments and experimental/numerical verifications, typically utilizing the plane-wave expansion method and/or the FDTD scheme as presented in chapter 3. Optimizations are done in an iterative trial-and-error procedure with changed parameters - typically the position or size of a PhC element - to improve a chosen performance measure of the component. Throughout this project the Edisonian method has been used extensively utilizing the *CrystalWave* and *MPB* software as verification tools. Figure 4.1 shows examples of how the design of a sixty degree bend in a W1 PhCW can be optimized by moving (green holes) and/or enlarging (yellow holes) holes in the bend [69–71]. The concept of moving and/or re-shaping PhC elements is based on a local perturbation of the guided mode in order to account for the dramatic change in k-vector enforced by the waveguide and to avoid mode-conversions into unguided higher-order or slab-modes [72, 73]. Such an optimization approach is very time-consuming, non-trivial, and does not gua-rantee optimal solutions. Recently, however, sensitivity analysis have shown to be assistive in choosing the critical parts of the PhC component to be altered (see e.g. ref. [74]) but it does not quantify the needed parameter-change and brings the optimization procedure back into the Edisonian loop.

There is an increasing interest in applying inverse design strategies for the designing and optimization of photonic circuits [75, 76] where inverse algorithms allow to work backward from a given objective function and to achieve the exact design of the dielectric structure that achieves the objective. This is similar to what is used extensively in the electronic industry when designing integrated circuits using the VHSIC hardware description language (VHDL)[1]. Within inte-

[1]Where the objective function is given through a software code that is transformed into a

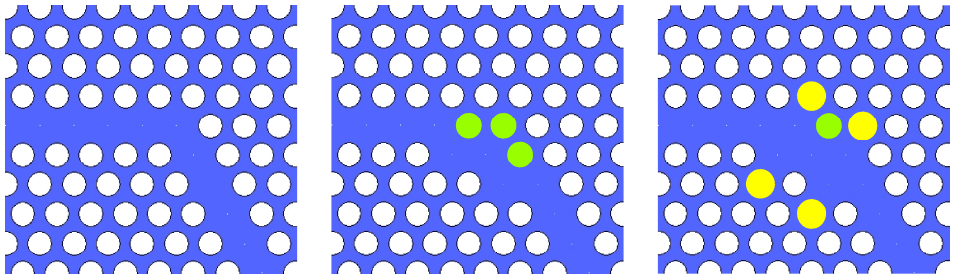

Figure 4.1: Examples on the design and optimization of a 60° bend in a PhCW by moving (green) holes and enlarging (yellow) holes. (a) The generic bend. (b) Three holes moved. (c) Combination of moving and enlarging holes.

grated optics, several different approaches such as the *level set* method [41,77], the *evolution algorithm* [78], and the *gradient descent*-based method [79] have been suggested to solve inverse design problems.

A different approach as presented in this thesis is to utilize topology optimization [80], which has been adopted from mechanical engineering and has found widespread use in a number of different applications. This design method offers an effective and robust optimization of the photonic crystal structure irrespectively of the device under consideration. The method is based on repeated finite element analysis where the distribution of material in a given design area is iteratively modified in order to improve a chosen performance measure. The resulting designs are inherently free from geometrical restrictions such as the number of PhC elements, their shapes, placement etc., thereby allowing the large potentials of PhC components to be exploited to hitherto unseen levels [81]. The utilization of topology optimization on photonic crystal structures is presented in details in refs. [82,83]. Here, the method will be presented and exemplified with an optimization for high transmission through a PhCW 60^0 bend. The optimization scheme has been developed by Ole Sigmund and Jakob S. Jensen at MEK•DTU and implemented into a user-friendly software package named *TopOpt* [84,85], which has been used for the optimization of some of the structures presented in this thesis.

The topology optimization method is, at present time, a 2D optimization scheme taking its starting point in the scalar wave equation for e.g. TE-polarized light:

$$\nabla^2 E(x,y) + \omega^2 \left(\frac{n(x,y)}{c}\right)^2 E(x,y) = 0 \tag{4.1}$$

where ω and c is the frequency and speed of light, respectively, n the refractive

circuit layout.

index describing the dielectric structure, and E is the electric field. Figure 4.2(a) sketches a PhCW with two consecutive 60^0 bends, which we want to optimize for high and broad transmission. A plane-wave is incident from the bottom left of the PhCW and is collected at the output port. At the top and bottom of the structure normal absorbing boundaries (cyan) are used. To eliminate unwanted reflections from the input and output ports perfectly matched layers (PMLs) are utilized at the in- and out-put by continuing the waveguide into these (gray regions). The generic 60^0 bend is known to have a very narrow bandwidth with low loss [86]. The goal of the optimization is to optimize the transmission through the bends in a broad wavelength range.

The topology optimization method is based on a finite element method that discretizes the solving of eq. (4.1) into rectangular bilinear elements and leads to a set of equations

$$\mathbf{S}(\omega)\mathbf{u} = \mathbf{f}(\omega) \tag{4.2}$$

where $\mathbf{S}(\omega)$ is a frequency-dependent system matrix, $\mathbf{f}(\omega)$ a frequency-dependent load vector modelling the incident harmonic wave, and $\mathbf{u}$ the vector for which the equation is to be solved. The structure domain Ω in fig. 4.2(a) is discretized into appropriately chosen square blocks so that the structure can be build from only a few different blocks due to the periodicity. Each block is again discretized into a number of finite elements mainly dependent on the computer power available.

The objective is to optimize the transmission of energy through the waveguide by maximizing the time-averaged Poynting vector through the area Ω_P in fig. 4.2(a) (yellow). The optimization is achieved by redistributing material in the (arbitrarily) chosen design domains Ω_D (red), thereby affecting the time-averaged Poynting vector in the area Ω_P. A suitable objective function for the optimization is the component of the Poynting vector that points in the output direction of the structure P^{out} averaged over all finite elements in the domain Ω_P:

$$P^{\text{out}} = \frac{1}{N} \sum_{e \in \Omega_{\text{P}}} P_e^{\text{out}} \tag{4.3}$$

where N is the total number of finite elements in the domain Ω_P.

Thus, the optimization problem can be formulated as:

$$\max_{x_e} P^{out}(\omega). \tag{4.4}$$

In order to decrease the number of needed calculations and the total computational time, the redistribution of material is done iteratively by applying a sensitivity analysis where each finite element in the design domain is assigned to a design variable

$$x_i \in \Re | 0 \leq x_i \leq 1 \text{ for } i = 1, M$$

where M is the total number of elements in the domain Ω_D. The refractive index n_i of the ith element in the design domain is then expressed by a linear interpolation:

$$n_i^2 = n_1^2 + x_i(n_2^2 - n_1^2) \tag{4.5}$$

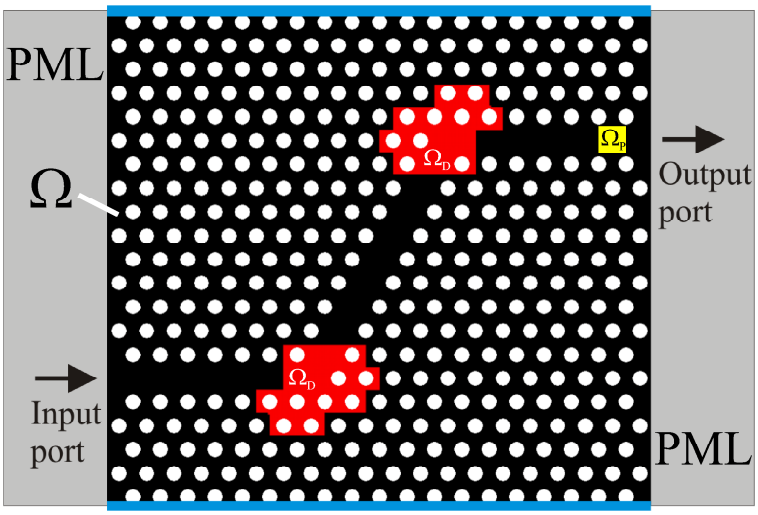

(a)

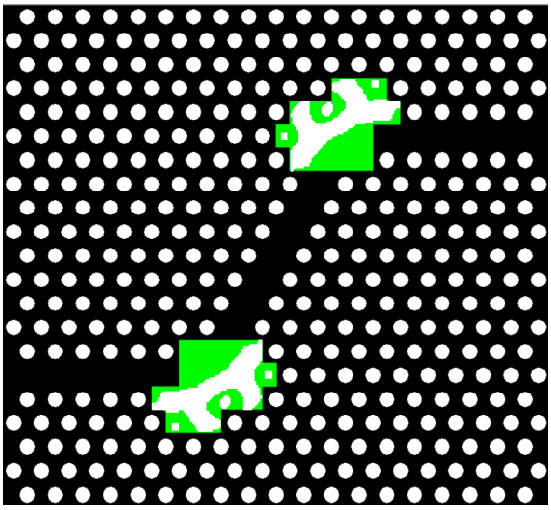

(b)

Figure 4.2: Schematics of a photonic crystal waveguide containing two con-secutive 60^0 bends. (a) Generic bend configuration. The red areas illustrate the chosen design domains in the topology optimization procedure. (b) Topology-optimized bends. The green areas highlight the optimized structures showing that a non-trivial smoothening has been applied to the bend.

where n_1 and n_2 are the indices of the holes and the silicon, respectively. If $x_i = 0$ the element take the refractive index of n_1, if $x_i = 1$ it takes the index of silicon n_2, and for any intermediate value of x_i the index will be between n_1 and n_2.

For a given initial distribution of x_i the optimization problem in eq. (4.4) is solved by calculating P^{out} along with the sensitivities $\frac{\delta P^{out}}{\delta x_i}$, i.e. the influence of each finite element on the energy flow through area Ω_P. A numerical method of moving asymptotes (see ref. [80] for details) is applied to transform P^{out} and the sensitivities into a new and improved design suggestion, i.e. updated values x_{new_i} of x_i so that P^{out} and the sensitivities can be recalculated. This iterative procedure is continued until $\max |x_{new_i} - x_i| < \delta$, where δ is a small positive constant. In order to create a broadband component the power flow can be evaluated for several frequencies (up to 6) in the chosen frequency range. During the optimization procedure the output is maximized for all frequencies, and these target frequencies can be updated e.g. every 10th or 20th iteration in order to eliminate transmission dips in the frequency range.

Even though a converged design leading to a maximized energy flow through the waveguide is obtained, the solution may have problems [83]. First, the obtained maximum may be non-unique and result in multiple local maxima and, hence, lead to resonance effects and poor performance of the design. To overcome this a continuation method is applied in which an artificial damping (β-value in *TopOpt*) is introduced to smooth the dynamic response of the structure and to avoid undesired local extremes. Secondly, eq. (4.5) allows each finite element to have a non-physical refractive index, i.e. $n_1 < n_i < n_2$ that makes the design unrealistic to fabricate. These undesired 'gray elements' can be removed by inducing an extra energy loss (ϵ-value in *TopOpt*) to elements $0 < x_i < 1$. In practice, the filtering and damping parameters can be changed iteratively to obtain a smooth spectral response with no (few) 'gray elements'.

The optimized design for the PhCW with two 60^0 bends is shown in fig. 4.2(b) where the green areas highlight the optimized design domains. This design was obtained after approximately 1000 iterations (each iteration taking around 5 seconds) of the optimization algorithm, however, with the qualitative structure of the design appearing after about 200 iterations. Clearly, the bends have been smoothened by applying a soft curvature in the bend region and one hole has been removed on the inner side of the bend.

Figure 4.3 shows the steady-state magnetic field distribution for the fundamental PBG mode simulated using 2D FDTD for the *fabricated*[2] PhCWs with the topology-optimized bends. The left image shows the mode behavior for light incident from the bottom-left through the PhCW with the generic bends. It is clearly seen that the generic bend forms a severe discontinuity in the PhCW and excite an odd mode, which is not well guided in the PhCW. Moreover, the lower bend introduces large reflections and scattering of light to the PhC structure. In contrast, the right image shows that the topology-optimized bend regions guide

[2]The fabricated structures deviate from the actual optimized structures due to line-broadening in the etch.

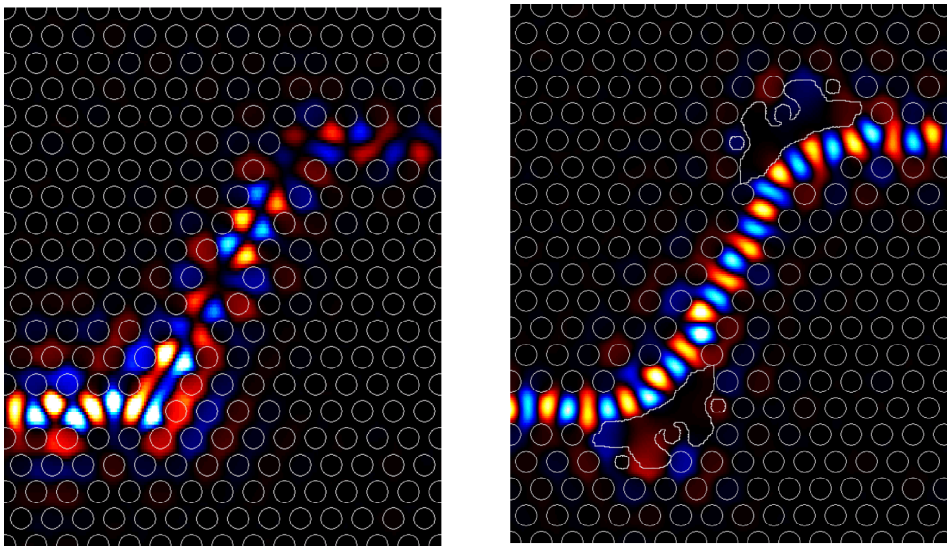

Figure 4.3: Steady-state magnetic field distribution for the fundamental PBG TE-mode simulated using 2D FDTD. The mode is incident from the bottom-left part of the waveguide. [Left] Mode profile through the generic bends. [Right] Mode profile through the topology-optimized bends.

the fundamental PBG mode nicely through the two bends without disturbing the mode profile. Experimental results on the topology-optimized 60^0 bends will be presented in chapter 6 among other results for topology-optimized structures.

Chapter 5

Fabrication of Photonic Crystal Structures

This chapter will present issues on the fabrication of photonic crystals in the silicon-on-insulator material. Fabrication of nanophotonic structures with feature sizes down to a few tens of nanometers is a very demanding process and requires high-resolution lithography and a highly anisotropic etch. Conventional optical lithography for photonic structures utilizing wavelengths in the optical or near-ultra-violet range (presently, 365 nm being the shortest) limits the feature size for dense features to approximately 600 nm, which is insufficient for fabricating photonic crystals operating in the telecom wavelength range. Going to even lower wavelengths in the deep ultra-violet region the resolution can be squeezed down to feature sizes of ∼240 nm, which is just sufficient for generic PhC structures for use in the 1550 nm wavelength regime. At COM•DTU, we have been involved in the utilization of deep-ultra-violet (DUV) lithography for fabricating PhC structures in the scope of the IST PICCO project with the fabrication part (except for designing the structures) being done by the project-partners at the Ghent University. For detailed information about utilizing DUV lithography to fabricate PhC structures the reader is refereed to refs. [40, 87, 88].

The majority of the photonic structures to be presented in chapter 6 have been fabricated in the DANCHIP cleanroom utilizing state-of-the-art electron beam lithography (EBL) offering resolutions below 20 nm and will be in focus of this chapter. For the mass fabrication of nanophotonics EBL is not feasible due to its sequential scanning procedure. However, nanoimprint lithography allows the mass-fabrication of sub-100 nm structures and has been challenged in this project for the fabrication of nanophotonics. The work done on NIL[1] will also be presented in this chapter. The transfer of patterns from the resist to the silicon have been done by using reactive ion etching (RIE) as presented in the end of the chapter.

[I]Done in collaboration with the Micro-Electro-Mechanical Systems (MEMS) group at MIC•DTU.

5.1 Process Overview

The main steps in the fabrication of nanophotonic structures realized in the SOI slab configuration as sketched in fig. 3.1 are as listed below. Appendix C presents detailed information and parameters for each step and can be used as guidance/inspiration for the future fabrication of nanophotonic circuits at COM•DTU. The main steps are:

- Preparation of design files in the GDSII format.
- Spin-cleaning of wafer in acetone, ethanol, iso-propanol (IPA) and blow-dry with N_2.
- Resist spinning (ZEP520A, ∼100 nm thick).
- Pre-baking 2 min. at 130^0C.
- Cleaving in pieces and blow with N_2.
- Electron beam Lithography.
- Development, 1 min. in ZED-N50, rinse in 15 seconds in IPA.
- Post-bake 5 min. at 110^0C.
- (SEM inspection).
- Etch, (ICP) RIE.
- SEM inspection.
- (Thermal Oxidation and SEM inspection).
- Cleaving of sample to waveguides.

Figure 5.1 shows a schematic of the fabrication. After a cleaning procedure, the SOI wafer is covered in a spinning process with a thin layer of electron beam resist that is used as a soft mask in an etching process. The resist is a high-resolution positive Zep520A[2] resist having a high sensitivity. The Zep520A resist is diluted 1:1 in anisole (methoxybenzene) to decrease the viscosity and, thus, the resulting film thickness after a spinning procedure. A thin film is needed in order to obtain a high fidelity in a following pattern transfer to the silicon. However, the film should be thick enough to comply to the selectivity between the resist and silicon compared to the needed etch-depth. The thickness is typically ∼100 nm, which is measured with a Dektak 8 profiler and sufficient for etching all the way through the top silicon layer without degrading the resolution. Prior to the lithography step the resist is pre-baked 2 minutes at 130^0C on at hotplate to drive out the solvent and harden the resist film. As the resist is positive, areas in the resist that

[2]http://www.zeon.co.jp/business_e/enterprise/imagelec/imagelec.html

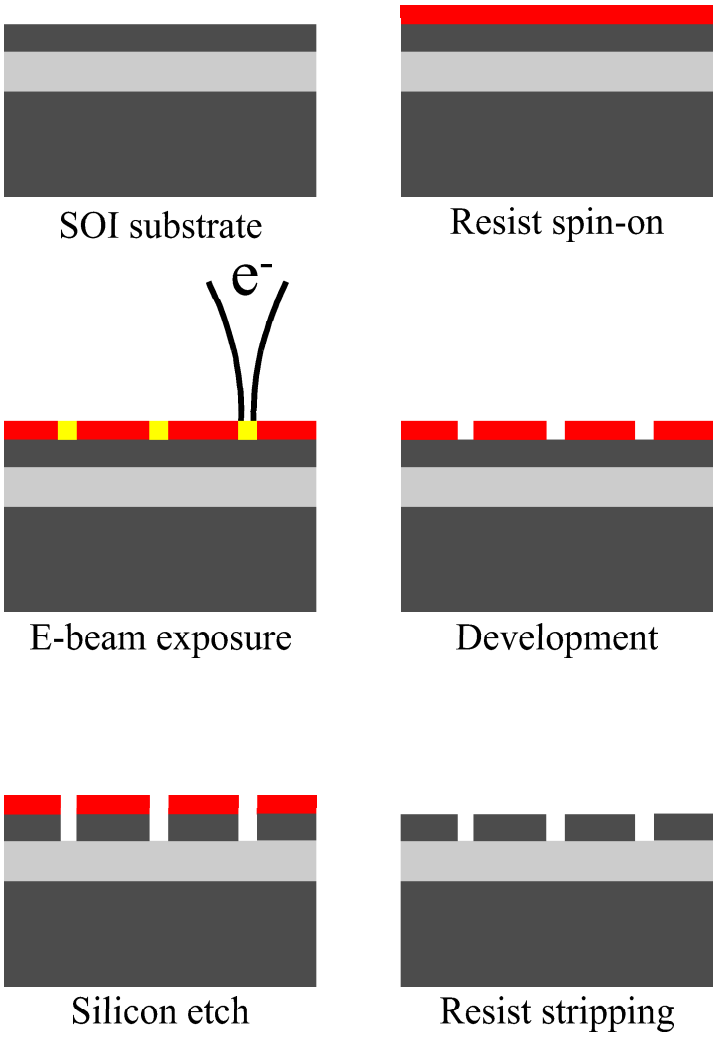

Figure 5.1: Schematic overview of the fabrication when utilizing electron beam lithography.

are exposed to the electron beam (e-beam) in the EBL will change their chemistry and become soluble in a following development and, hence, will be removed. In a dry-etch process where chemical reactions between the etchant and the silicon are enhanced by ions bombardment the unprotected silicon can be etched away and, hence, the pattern in the resist is transferred to the silicon. To track the quality of the EBL and the etch step a scanning electron micrograph inspection could (should) be made after the EBL and etch steps. Finally, any remaining resist is removed in a sputtering process. Optionally, the patterns can be transferred further down into the underlying silica layer utilizing the silicon layer as a mask and/or a thermal oxidation can be performed to smoothen out sidewall/surface roughnesses and increase the degree of vertical symmetry of the structures.

5.2 Electron Beam Lithography

The electron beam facility in the DANCHIP cleanroom is (at present time) a state-of-the art JEOL JBX-9300FS electron beam lithography system[3] featuring a spot-beam focused by a four-stage lens system and a pattern writing combining a vector scan and a step-and-repeat stage movement. The position of the stage is controlled by a laser-interferometer positioning system with a resolution of approximately 0.62 nm. The acceleration voltage of the e-beam from the ZrO/W emitter can be 50 kV or 100 kV and the beam can be moved with a speed of 25 MHz. At a acceleration voltage of 100 kV the writing field is 500 μm $\times$ 500 μm and the stitching and field overlay accuracy is below 30 nm [89]. An overview of the JBX-9300FS e-beam system can be found in the general statement manual provided by JEOL[4].

The e-beam facility has sample carriers for 2" and 4" wafers and a carrier for small chips of custom size. Typically, samples have been cleaved from a 4" SOI wafer with ZEP520A resist to a size of 1 cm $\times$ 5 cm to fit into the 2" carrier. The chip designs have typical sizes of 4 mm $\times$ 4 mm so that 3 chip designs can be written on one sample and easily cleaved to the waveguides afterwards.

5.2.1 Sample Design

As will be presented in chapter 6 the propagation loss in a SOI W1 PhCW is rather severe in size. Therefore, the length of the PhCWs are limited in length to a few hundreds of microns. SOI samples with widths of only a few hundreds of microns are extremely difficult to cleave and handle in practice. Therefore, butt-coupled ridge waveguides are usually used to route light to and from PhC structures. Typically, the total length of the ridge waveguides are $\sim$4 mm and, thus, so is the sample width. The ridge waveguides are tapered from 4 μm at the sample facet to $\sim$ 700 nm at the PhC structures to secure good optical coupling to the

[3] http://www.jeol.com/eb_/eblprods/jbx9300fs.html.

[4] Can be found by googling "general statement" and "JBX9300-FS" at e.g. http://grover.mirc.gatech.edu/equipment/manuals/General%20Statement.pdf.

input/output fibers and to the PhC structures [90], respectively. As the ZEP520A is a positive e-beam resist the ridge waveguides are defined by two closely-spaced trenches with a width of 3μm and the distance between the edge of the trenches being the waveguide width. Compared to the PhC structures these trenches are rather bulky and, hence, do not require to be written with an extremely high resolution. Conveniently, the trenches can be placed in a separate design layer and written with a larger spot size (larger current)[5].

In the design file holes are defined by polygons. The actual number of vertices in the polygons is very important for the writing to be successful. On one hand, restrictions are put by the computer hardware available because the design is partitioned into sub-polygons when converting the design file into the e-beam file format (from GDSII to V30). If the holes are defined by polygons with too many vertices the file conversion fails. On the other hand, due the high resolution of the e-beam too few vertices results in non-circular holes in the resist. Figure 5.2 shows the shot shape displays for holes defined by (a) an octagon (b) a dodecagon and (c) multiple boxes matching the step and e-beam size. As seen, the most homogenous spot distribution is obtained for the holes defined by multiple boxes matching the step and e-beam size. Unfortunately, defining holes in this way limits the size of the actual design due to an enormous amount of polygons for the computer hardware to handle. The figure also shows SEM images of how the holes turn out into the resist after development. It is clear that holes defined by octagons actually turn out to be octagons in the resist. However, no (little) difference is seen between holes defined by a dodecagon and a box structure and both turn out nice and circular[6]. Therefore, holes are defined by dodecagons, which do not limit the size of the design (severely) and do turn out circular in the resist.

5.2.2 Proximity Correction

In EBL electrons scatter when they impinge upon the resist and the SOI structure. This means that areas that are not intended to be exposed will be exposed and that the writing of neighboring structures influence each other. Hence, errors such as line-broadening and fine-detail washouts will be introduced in the resulting pattern. This is addressed as the proximity effect and is mainly split up in a forward-scattering effect, representing a beam-broadening when electrons scatter down into the resist film, and a backward-scattering effect, occurring when electrons bounce back and forth in the resist and the substrate. The resulting effect is highly dependent on the density of the structures and the acceleration voltage of

[5]In order to take full advantage of this "trick" and increase/decrease the current/writing time dramatically the aperture of the e-beam should be changed to a larger one from the 60 μm wide used as standard. This requires to have a remote-control-aperture system installed, which has not been available throughout this project. Thus, ridge waveguides and PhC structures presented in this thesis are written with the same (small) current. However, a remote-control-aperture system is expected to be installed at DANCHIP medio 2006.

[6]Presently, a new software tool for making a quantitative analysis of the hole shape in the SEM picture is being tested. However, in this thesis holes will only be analyzed qualitatively.

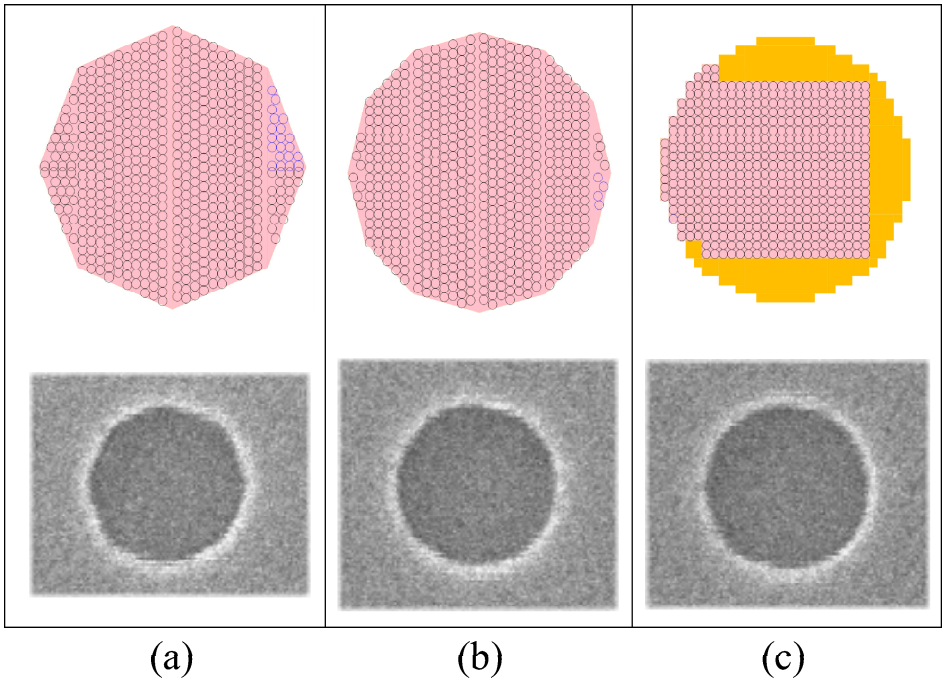

Figure 5.2: Shot shape display and SEM pictures for holes having (a) 8 vertices (b) 12 vertices (c) a box structure (the yellow areas are present due to limitations in the display properties of the computer). The beam width and step size is 8 nm.

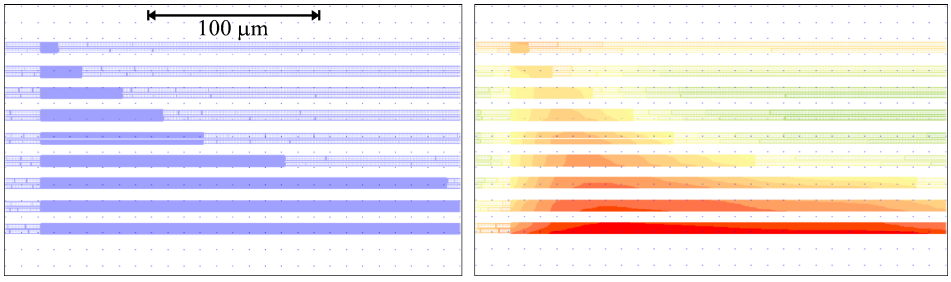

Figure 5.3: Zoom-in on a typical design of PhCWs (dense, blue) and the ridge waveguides (sparse, blue). (a) Without proximity correction. (b) Output from PROXECCO with doses ranging from the nominal dose (green) to 1.34 times the nominal dose (red).

the beam [91]. On one hand, higher acceleration voltages lower the forward scattering but raise the backward scattering range of the electrons and, on the other hand, decreasing feature sizes and higher structure densities require that forward-scattering effects are taken into account. This makes a proximity correction scheme very complex as both effects have to be accounted for in nanophotonics.

Typically, the contributions to the energy distribution in the resist caused by forward and backward scattering are approximated by the sum of two Gaussian-functions [92]:

$$f(r) = \frac{1}{\pi(1+\eta)} \left(\frac{1}{\alpha^2} exp\left(-\frac{r^2}{\alpha^2} \right) + \frac{\eta}{\beta^2} exp\left(-\frac{r^2}{\beta^2} \right) \right) \tag{5.1}$$

with α representing the width of the broadened exposure beam, β the radius of the backward-scattering range, and η the ratio between the exposure coming from the forward and backward scattering electrons. The values of α, β, and η are highly dependent on the beam energy and diameter, the resist chemistry and thickness, and the substrate type. The parameters should be calculated for the exact writing conditions and material parameters using e.g. a Monte Carlo simulator such as *Sceleton*[7]. For the SOI slab configuration in focus the parameters were calculated to $\alpha = 0.0125\,\mu$m, $\beta = 34.12\,\mu$m, and $\eta = 0.521$ [93]. Thus, backward-scattering effects can be expected to be rather severe and to have a radial range of $\sim 34\mu$m from the injection point. Based on the energy distribution several different schemes can be applied to level out local and global differences in the accumulated energy. Here, this is done by partitioning the design into appropriate-sized polygons and assigning different e-beam doses to the polygons.

[7] http://www.aiss.de/sceleton/sceleton-index.html.

In this project, the calculated proximity parameters were used for input to the *PROXECCO*[8] software tool to correct for proximity effects. The accuracy and efficiency of *PROXECCO* are based on a separate treatment of the pattern and correction. The mathematical algorithm uses an improved deconvolution method, which describes the proximity effects very well according to ref. [94]. Figure 5.3(a) shows a zoom-in on a typical design of PhCWs (dense, blue) with different lengths and butt-coupled to ridge waveguides (sparse, blue). If no proximity correction is applied all structures in the design will be written with the same nominal e-beam dose. By experiment, it has been found that if no proximity correction is applied the diameter of the holes along and between the waveguides in fig. 5.3 can differ as much as 20%-30%, which would be devastating for the performance of the PhCW. If proximity correction is applied as shown in fig. 5.3(b) structures, which are in a high-density area, as is the case for the center part of the ridge waveguides, will be written with a low(er) dose (green) and structures, which are in a low-density area as the long(er) PhCWs, will be written with a higher dose up to 1.34 times the nominal dose (red). The fabricated PhCWs written with proximity correction showed no change in hole diameter along the waveguide or between different waveguides. Proximity effects can be accounted for in a crude way by e.g. introducing dummy structures in the design or by fixing the density of structures to get a globally more homogenous energy distribution.

5.2.3 Choice of E-Beam Parameters

For EBL a clearance dose should be decided upon e.g. by experiments in order for the exposed areas to develop correctly and be fully removed. The e-beam dose Q is calculated by

$$Q = \frac{t \times I}{A} \tag{5.2}$$

where t is the dwell time of the beam, I the beam-current, and A the pattern writing area. The small area deflector in the lens system of the e-beam works at a speed of 25 MHz, which means that the minimum dwell time is $t_{min} = 40$ ns. The current should be chosen according to the smallest feature size of the structure as the beam diameter increases with increasing current. The step size should be chosen slightly smaller than or equal to the beam-width in order to obtain a good dose uniformity and a relatively steep dose gradient at the edge of the patterns. Thus, when the needed clearance dose has been found the current and the step size should be chosen to match the feature sizes of the pattern and to comply with the minimum dwell time.

For holes with diameter $D \approx 250$ nm written in a ZEP520A resist, the clearance dose was found to be 200 $\frac{\mu C}{cm^2}$. As the PhC structures may contain fine-details below 20 nm in size a small beam width should be chosen. According to simulations performed by the e-beam manufacturer JEOL a current of 2 nA results in a beam-width of 8 nm, which should be appropriate for $\sim$20 nm features. If the step size

[8] http://www.aiss.de/PROXECCO/PROXECCO.html

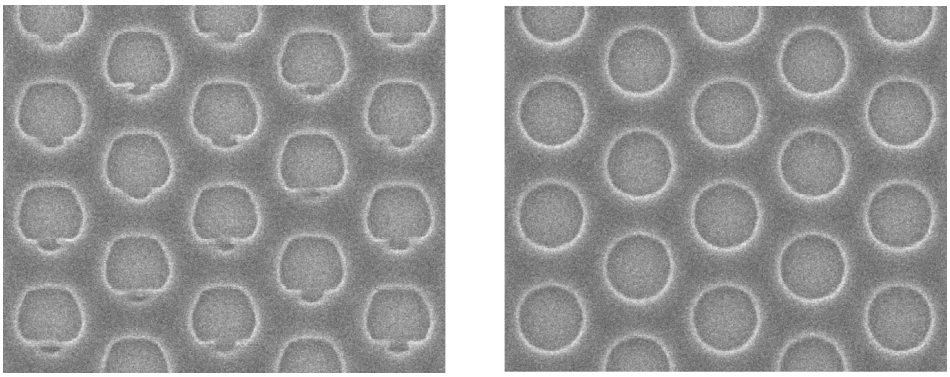

Figure 5.4: SEM pictures of holes written in the e-beam resist with a step size of 4 nm and a current of (a) 2 nA and (b) 0.2 nA.

is chosen equal to the beam-width securing a uniform distribution the dwell time will be

$$t = \frac{A \times Q}{I} = \frac{64\,\mathrm{nm}^2 \times 200\,\frac{\mu C}{cm^2}}{2\,\mathrm{nA}} = 64\,\mathrm{ns} \tag{5.3}$$

which is above $t_{min} = 40$ ns and, hence, makes the chosen parameters legitimate. However, if proximity correction is applied to the design the situation is different. Figure 5.4(a) shows a SEM picture of a proximity corrected PhC structure written in the resist with a dwell time $t = 64$ ns. Clearly, the writing has not been successful as the holes turn out having 'noses'. Decreasing the current to 0.2 nA ($t = 640$ ns) keeping the other parameters fixed removes the 'nose' problem as seen in fig. 5.4(b). This phenomenon has been seen and tested for various e-beam parameters and is caused by the rapid change in dwell time (dose) for proximity corrected structures that pushes the electronics of the small area deflector to its limit. Therefore, if writing a proximity corrected design, the dwell time needs to be far higher than the minimum limit set by the no-minal dose. Typically, a current of 0.2 nA was needed for proximity corrected structures.

5.3 Nanoimprint Lithography

For research applications and mask fabrication EBL is an excellent choice for the lithographic step when fabricating photonic circuits having sub-600 nm features. This is due to the high degree of flexibility and high achievable resolution that EBL offers. However, for the mass-fabrication of nanophotonic circuits EBL fails due to its sequential scanning procedure, hence, making it a very time consuming

and expensive tool to use. As an example, a successful writing of a 4 mm $\times$ 4 mm design with the present equipment available in the DANCHIP cleanroom would take around 10 hours at a cost of $\sim$700 Euro/hour! Thus, EBL is not feasible for fabricating cost-effective nanophotonics.

Nanoimprint lithography (NIL) has received considerable interests in the last few years for fulfilling the demands for a low-cost, high-yield, and high-resolution nano lithographic technique and has been adapted to be a potential technique to deliver the 32 nm node in 2013 [95]. At MIC•DTU there is an on-going research activity to develop NIL techniques for the fabrication of various nano- and micro-systems in the DANCHIP cleanroom. In this section, the progress on the fabrication of PhC structures at DANCHIP will be presented. The fabrication of the NIL mold and the optimization of the imprinting parameters have been carried out by the ph.d. students[9] Brian Bilenberg and Theodor Nielsen associated with MIC•DTU [96].

Figure 5.5 shows the principle of NIL. A silicon stamp is fabricated by utilizing e.g. EBL. The stamp contains the inverted structure to be realized and is imprinted into a resist layer covering the target material (fig. 5.5(a)). A high pressure is applied to the stamp during the imprint that takes place at an e-levated temperature in a vacuum chamber and lasts approximately 10 minutes (fig. 5.5(b)). The high temperature secures that the resist will easily flow away from e.g. the pillars into the cavities of the stamp. Thereafter, the stamp and the substrate are separated from each other leaving an imprint in the resist (fig. 5.5(c)). Subsequently, the patterns can be transferred down into the target material by conventional etching (fig. 5.5(d)). However, as sketched in fig. 5.5(c), a residual layer of resist may be present after imprinting and this should be accounted for when determining the etching parameters, i.e. the etching time should be increased or the resist should be exposed to an initial oxygen-plasma. The advantages of NIL is that once the stamp have been fabricated using a 'slow' high-resolution lithographic step as e.g. EBL, the stamp can be used for imprinting more than 1000 fully-patterned 4" wafers without degrading the fidelity of the pattern transfer.

Figure 5.6(a) shows a SEM image of a topology-optimized PhC Y-splitter in a NIL silicon stamp, which has been prepared by utilizing EBL and writing the inverted design into a 50 nm thick film of a TEBN-1 high resolution, low sensitive, and negative resist[10] at an exposure dose of 9 mC/cm^2 (*milli* coulomb!). The written structures are developed in methyl isobutyl ketone (MIBK) for 20 seconds, rinsed in isopropyl alcohol and subsequently transferred 100 nm into the silicon substrate by a highly anisotropic reactive ion etch. It is seen that the design has been successfully transferred to the stamp with an extremely high resolution as the pillars of diameter $\sim$250 nm turn out as octagons as they were defined as in the design file. Moreover, the sub-20 nm features of the topology optimized structures are nicely replicated in the silicon stamp. The target SOI wafer was spin-coated with a 80 nm thick mr-I T85 (4 wt%) resist and baked at 150^{0}C for

[9]Their work have turned out into the startup company, NIL Technology.
[10]TEBN-1 by Tokuyama Corp., Tokyo, Japan, www.tokuyama.co.jp

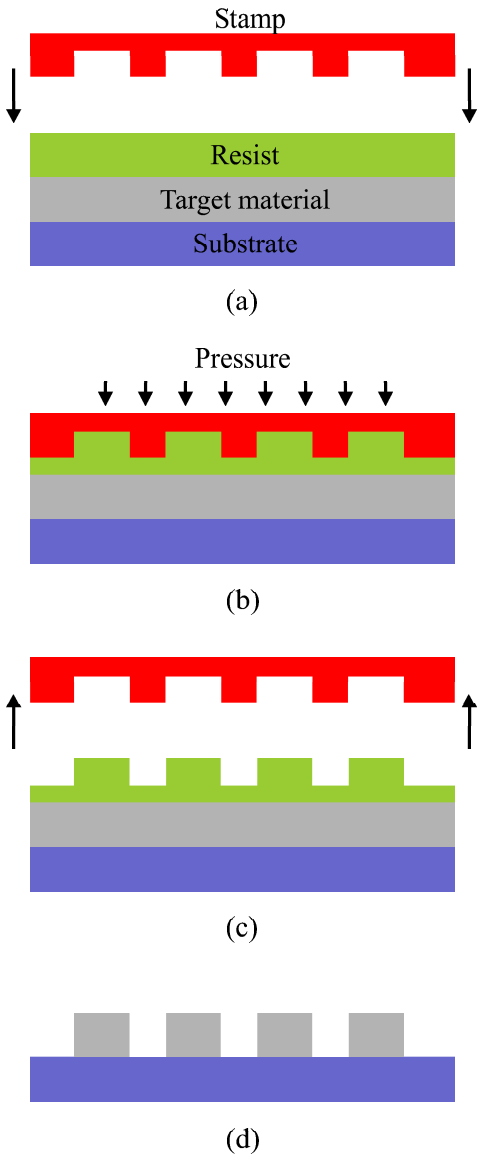

Figure 5.5: Concept of nanoimprint lithography. (a) A predefined stamp (by use of e.g. EBL) with the inverted structures is (b) pressed into the resist at an elevated temperature. (c) The stamp and the resist are carefully separated and an imprint remains in the resist, which (d) can be used as a mask in a following etch.

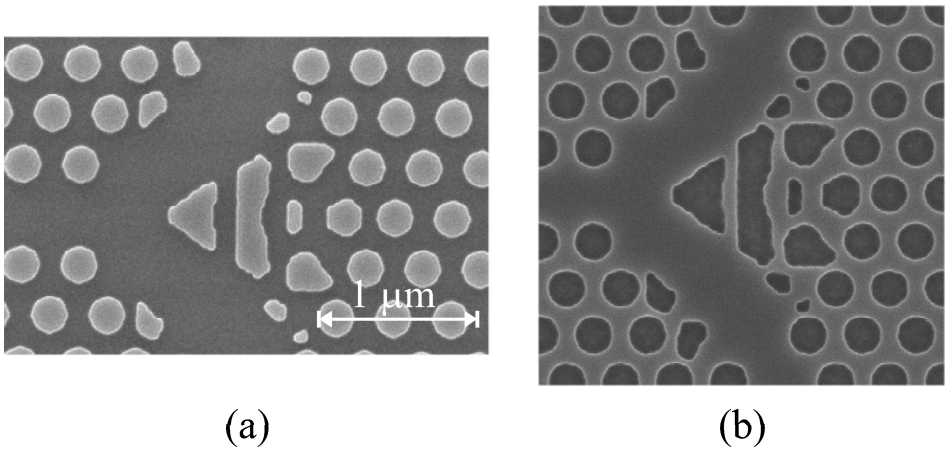

Figure 5.6: (a) SEM zoom-in of a NIL stamp prepared by utilizing EBL showing silicon pillars (light-gray) in air. The pattern is a topology-optimized PhC splitter. (b) SEM image of an imprinted and etched PhC structure in SOI using the stamp shown in (a).

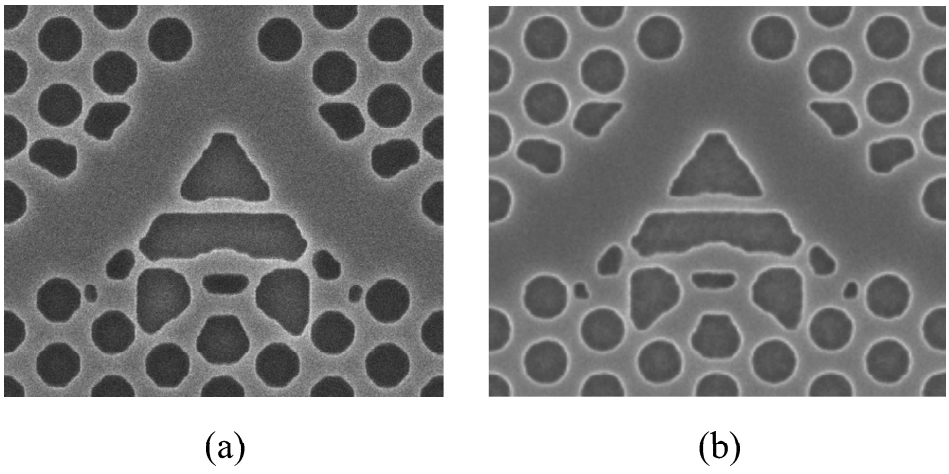

Figure 5.7: SEM images showing an etched topology optimized Y-splitter fabricated utilizing (a) EBL and (b) NIL.

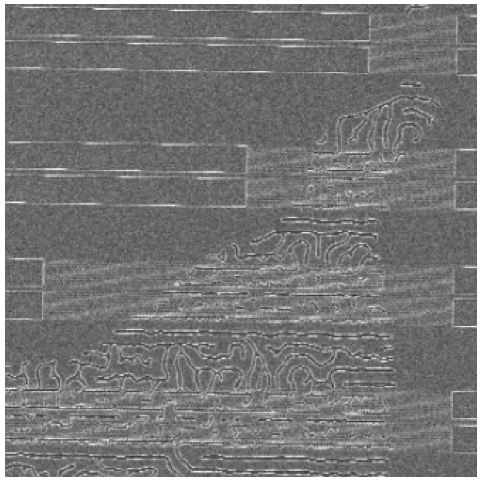

Figure 5.8: A SEM showing the 'sand-work' effect on longer PhCWs which occurs when imprinting structures with abruptly changing and decreasing pattern density.

5 min on a hot plate. The stamp is imprinted using an EVG imprint tool (EVG 520HE) at a temperature of 140^0C and an imprint pressure of 13 bar. The imprint took place in vacuum (0.01 mbar) and the stamp and substrate were separated at a temperature of 60^0C. Figure 5.6(b) shows a SEM image of the imprinted and etched structure utilizing the stamp shown in fig. 5.6(a). Clearly, the PhC and the topology-optimized structures have been imprinted with an exceptional high quality and resolution without any severe line-broadening[11]. A direct comparison between a topology-optimized Y-splitter fabricated utilizing (a) EBL and (b) NIL can be seen in fig. 5.7. As seen from the figure, the NIL process replicates the details in the nano-scale pattern with a quality comparable to or better than utilizing electron beam writing.

However, even though we have shown that NIL indeed can be used for the fabrication of PhC structures, care needs to be taken in the design of the structures to secure that the resist in the imprint completely fills the cavities of the NIL stamp and that the thickness of the residual layer of resist is minimized and homogeneous on the wafer. One major issue is the pattern density on the wafer that can lead to 'sand-worm' effects as shown in fig. 5.8 when the density of patterns locally changes too abruptly. To avoid such effects dummy structures could be placed among the real structures. However, these issues have not been investigated thoroughly and need to be addressed before full wafers with PhC structures can be imprinted successfully. Experimental results for structures fabricated using NIL is presented in chapter 6.

[11]The shown stamp and imprint is actually from the very first test run!

5.4 Reactive Ion Etching

The major issues in an etching process of sub-micron structures are the etching rate, the anisotropy, and the sidewall roughness. First of all, to obtain a high fidelity in the pattern transfer the thickness of the masking material (resist) should be chosen as thin as possible, but thick enough to withstand the etch. Next, it is important that the vertical etch rate ν_v is very much higher than the horizontal etch rate ν_h in order to have a high degree of anisotropy defined by $A \equiv 1 - \frac{\nu_h}{\nu_v}$ and to avoid linebroadening in the patterns. Finally, sidewalls and surfaces should appear with as little roughness as possible as this is a critical issue for the performance of optical devices [40, 61, 62, 97].

In this thesis, the nanophotonic patterns have been transferred to the top-silicon layer of the SOI wafer by using the resist as a soft mask in a SF_6-based highly-anisotropic reactive ion dry-etch (RIE) [98–101] where the etch of silicon is primarily due to free fluorine appearing from a plasma dissociation of SF_6 [98]:

$$e + \mathrm{SF}_x(\mathrm{g}) \longrightarrow \mathrm{SF}_{(x-1)}(\mathrm{g}) + \mathrm{F}(\mathrm{g}) + e \quad (x = 3 - 6). \tag{5.4}$$

The overall stoichiometry of the etching by atomic F is

$$\mathrm{Si}(\mathrm{s}) + 4\mathrm{F}(\mathrm{g}) \longrightarrow \mathrm{SiF}_4(\mathrm{g}). \tag{5.5}$$

The etch takes place in a plasma-etching system [100, 101] where an inherent electrical potential difference between the ions in the plasma and the target substrate will result in a bombardment of ions onto the surface of the substrate. This helps clear the surface for reaction products, thereby enhancing the vertical etch rate. The anisotropy is increased by adding carbon-fluorides or oxygen, which forms protective films on the substrate surfaces. The directional ion bombardment is even more important in removing these films, which are only removed slowly on the vertical surfaces, thus, increasing the vertical/horisontal etch rate ratio. The SF_6-based chemistry etches only silica very slowly, thus, the underlying silica layer of the SOI material can be used as an etch stop.

5.4.1 Traditional RIE

At DANCHIP there is access to two different RIE systems both manufactured by Surface Technology Systems (STS). The STS RIE was installed at DANCHIP in 1993 and has been optimized for deep etching of micron-scale patterns in si-licon with a load of 40%-60% and with a high anisotropy and good selectivity between Si/SiO_2 and Si/photoresist [102]. The parameters of the optimized etch process is listed in table 5.1. The oxygen is added in the process to passivate the surfaces and to increase the fluorine concentration by preventing the atomic F to recombine with SF_x. The recipe was adopted from earlier studies to this project for the etching of the e-beam patterned samples and showed a feasible selectivity between silicon and ZEP520A. Typically, the etch rate of silicon and the ZEP520A is ∼340 nm/min. and ∼60 nm/min., respectively. However, significant day-to-day variations were

Parameter	Value	Unit
SF_6 flow	32	sccm
O_2 flow	8	sccm
Pressure	80	mTorr
Power	30	W

Table 5.1: The deposition parameters used in the STS RIE process. The process was optimized for etching micron-scale structures with a high anisotropy and good selectivity between Si/SiO_2 and Si/photoresist.

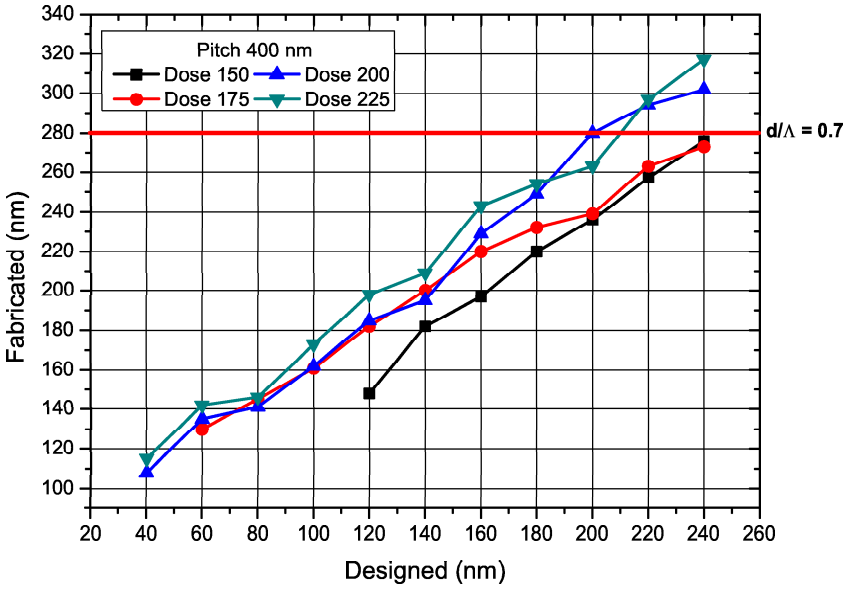

Figure 5.9: Measured diameter as a function of the designed diameter for holes placed in a triangular lattice with pitch $\Lambda = 400$ nm written with four different e-beam doses and etched with the recipe listed in table 5.1.

found in the etch rate due to fluctuating chamber conditions despite thorough preconditioning of the chamber. Figure 5.9 shows the measured diameter as a function of the designed diameter of holes placed in a lattice with pitch $\Lambda = 400$ nm for four different e-beam doses and after etching with the parameters in table 5.1. It is seen that a severe linebroadening is introduced in the etched structures. For the clearance dose of 200 $\frac{\mu C}{cm^2}$ the linebroadening (of the diameter) is ∼80 nm, which is unacceptably high for small-feature structures. In the project, several attempts have been made[12] to reduce the linebroadening in the shallow RIE etch of nano-structured patterns without affecting the selectivity between silicon and ZEP520A. The attempts were based on details found in ref. [98] and included changing: the pressure of the chamber, the platen power, the flow rates of SF_6 and O_2, and the addition of CHF_3 gas. However, the attempts were unsuccessful as e.g. higher flows of the passivating oxygen decreased the selectivity between ZEP520A and silicon, a lower chamber pressure resulted in an increased ion bombardment made the plasma unstable, and as the addition of CHF_3 degraded the anisotropy and selectivity.

Therefore, it is found that if the STS RIE at DANCHIP is going to be used for the fabrication of nano-structured patterns, the design should be corrected in accordance with the expected linebroadening seen in fig. 5.9. However, this is unacceptable for the fine-detailed topology optimized structures.

5.4.2 Inductively Coupled Plasma RIE

The STS Advanced Silicon Etch (ASE) available at DANCHIP utilizes an inductively coupled plasma (ICP) in a RIE process. The plasma in the ASE is generated by the field from a coil surrounding the plasma chamber and not by the capacitively coupled parallel-plates that drives the ion bombardment as in the conventional RIE system. The advantages of the ICP method are the ability to create high plasma densities resulting in 5-10 higher etch rates (up to $\sim 6\frac{\mu m}{min}$) and to keep the chamber pressure very low to avoid increased ion scattering, whereby the directionality of the ion bombardment is maintained [101]. Moreover, the ASE RIE can be operated using the Bosch process, where the etch and passivation chemistries can be separated in time by switching the process continuously between an etching and passivating chemistry in cycles of 2-15 seconds. In this way, sub-micron features can be etched very deep into silicon maintaining a high degree of anisotropy.

The STS ASE at DANCHIP was initially optimized for deep RIE of patterns into silicon, but have been optimized for shallow etches of nano-structured patterns in silicon by process engineer Peixiong Shi at DANCHIP [89]. This etch has been used in the project to etch PhC structures in SOI and the basic parameters of the etch are shown in table 5.2. All parameters for the etching recipe are listed in Appendix D.

[12] In collaboration with ph.d. student Amélie Têtu.

	Etch	Passivation
	Flow	Flow
C_4F_8	50	50
SF_6	50	0
Time	5 secs	3 secs
Pressure	10 mTorr	10 mTorr
Coil Power	500 W	400 W
Platen Power	30 W	0 W

Table 5.2: The deposition parameters used in the ASE RIE process. All etching parameters are listed in Appendix D.

The recipe uses an etching cycle of 5 seconds with a mixture of SF_6 and C_4F_8 and a 3 second passivating cycle with C_4F_8 only. Thus, passivation of the surfaces takes place during the full etch. The chamber pressure is kept low at 10 mTorr[13] during the etch to secure the directionality of the ion bombardment and, thus, obtain a highly anisotropic etch. It has been shown that the conditioning of the ASE chamber and stabilization of the silicon etch rate is more a thermal phenomenon than a chemical one [101]. Thus, preconditioning of the chamber is done by heating up the chamber with a high-energy oxygen plasma for ∼30 minutes. After this, the silicon etch rate is found to stabilize at ∼450 $\frac{nm}{min}$. The selectivity between ZEP520A and silicon in the ASE RIE is found to be similar to that of the conventional RIE. Typically, the recipe listed in table 5.2 is run for 9 cycles to etch through a 340 nm thick silicon layer of the SOI wafer. As the recipe presently is given in 5 seconds etch cycles an over-etch of ∼30-40 nm can be expected. The linebroadening of the hole *diameter* that may be due to the over-etch is typically measured to be below 40 nm and is dependent on the feature size. No lateral undercutting of the resist or notches at the silicon/silica interface have been observed using this etch. However, in order to decrease the linebroadening the etch may be optimized even more by e.g. decrease the time of the etch cycles and re-balance the passivation cycle.

Figures 5.7 and 5.10 show SEM images of PhC structures written with EBL and etched in SOI utilizing the ICP RIE. Clearly, the holes turn out nice and circular and are successfully etched through the 340 nm thick silicon layer with a nice and steep sidewall profile.

[13]In the conventional STS RIE system at DANCHIP the chamber pressure should be above 38 mTorr in order to stabilize the plasma.

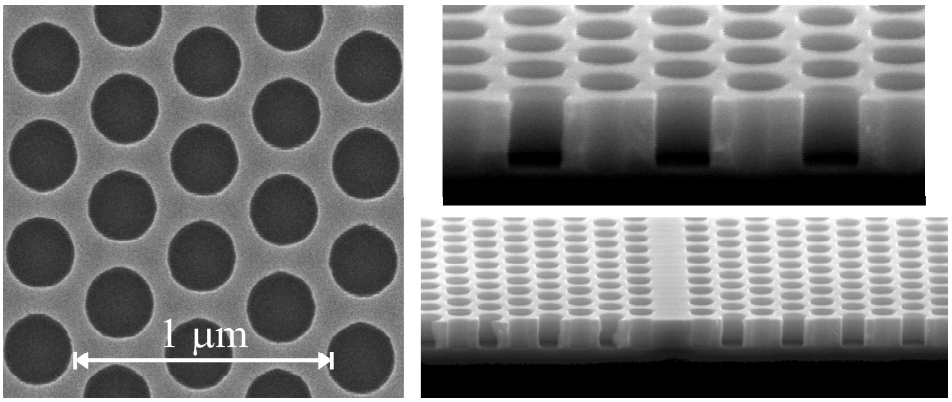

Figure 5.10: SEM images of PhC structures etched using the recipe in table 5.2.

5.5 Summary

The chapter presented the procedure for the fabrication of nanophotonic circuits utilizing electron-beam or nanoimprint lithography. Both lithographic tools have shown to transfer nano-structured patterns to the resist with a very high fidelity down to feature-sizes of 20 nm. However, proximity correction should be applied for the successful electron-beam writing of patterns with non-uniform densities. In nanoimprint lithographic care should also be taken for non-uniform designs e.g. by introducing dummy structures into the design. The inductively coupled plasma reactive ion etching was found to transfer the patterns to the silicon layer with high fidelities and steep side-wall profiles using the recipe given in Appendix D.

To summarize the chapter, a list of the recommended and basic parameters for the successful fabrication of PhC structures in the DANCHIP cleanroom will be listed. A more detailed step-by-step procedure of the fabrication procedure is given in Appendix C.

Design	# of vertices of holes	12
Resist	Thickness (ZEP520A)	∼100 nm
	Spin velocity	6000 rpm
	Spin time	60 secs.
	Spin acceleration	3500 rpm/s
	Acc. Time	5 secs.
	Pre-baking	2 min @ 130^0C
E-beam	E-beam current	0.2 nA
	E-beam step size	4 nm
	Clearance dose	200 $\frac{\mu C}{cm^2}$
	Proximity correction: alfa	0.0125 μm
	Proximity correction: beta	34.12 μm
	Proximity correction: eta	0.521
Develop	Develop time (ZED-N50)	1 min
	Post-baking	3 min @ 110^0C
Etch	Etch recipe	Pxnano1 @ ASE
	Pre-conditioning recipe	sjheat @ 30 min
	Etching time	9 cycles
	Resist stripping recipe	o2clean @ 1 min

Table 5.3: Selected and recommended parameters to use in the fabrication of photonic crystals in the DANCHIP cleanroom.

Chapter 6

Characterization of Photonic Bandgap & Nanophotonic Components

During the three-year project, numerous of different passive components have been designed, simulated, fabricated, and characterized. This chapter presents and discusses the successes from the characterization of fabricated structures. The first section will describe the characterization setups used for transmission and group index measurements and gives a short introduction to the setup used to perform scanning near-field optical microscopy on nanophotonic components[1]. The following sections deal with experimental results on the transmission cha-racteristics of straight photonic crystal waveguides, waveguide bends, T- and Y- splitters, and a coarse wavelength division multiplexor. One section is dedicated to components designed for the utilization of slow-light in photonic crystals and the chapter ends with a brief presentation of experiments done with liquid crystals in the photonic crystal.

6.1 Characterization Setup

The characterization setup used for measuring the transmission characteristics of a nanophotonic component is shown in fig. 6.1. For *broadband* characterization of a PhC device the light source in use is a ANDO AQ4222 light emitting diode (LED) having two diodes emitting at wavelengths centered around 1322 nm and 1538 nm, respectively. In this way, a spectrum for the wavelength range ∼1100 - 1700 nm can be obtained in a single sweep of the optical spectrum analyzer (OSA). Looking for fine details in the spectral behavior of the PhC component a linearly polarized

[1]The setup is located at the university of Aalborg and has been operated by partners in the FTP PIPE project (Valentyn Volkov).

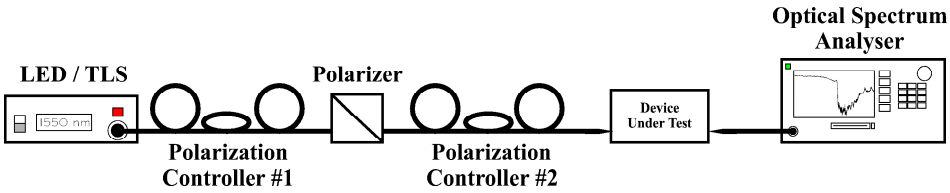

Figure 6.1: Characterization setup for measuring the transmission spectrum for a nanophotonic device.

tunable laser source (TLS) having a narrow bandwidth output in the wavelength range 1480 - 1580 nm (ANDO AQ4321A) or 1520 - 1620 nm (ANDO AQ4321D) is used. The setup shown in fig. 6.1 is used independently on the choice of light source to avoid moving around fibers that connects the components. A polarizer with an extinction ratio better than 35 dB is used to polarize the light. To align the main polarization-axis of light from the source a polarization controller (♯1) is used prior to the polarizer[2]. After the polarizer, yet another polarization controller (♯2) is used to select the proper polarization. To increase the fiber-to-waveguide coupling efficiency we use tapered-lensed fibers with a spot diameter of 2.5 μm (at $1/e^2$) on the facet. The fiber alignments are done using XYZ-stages controlled by piezo-resistive elements. The insertion loss for a ridge waveguide is $\sim$14 dB in the full wavelength region, thus the coupling loss from fiber-to-waveguide is $\sim$7 dB/coupling taking the propagation loss in the $\sim$4 mm ridge waveguide to be negligible. The transmission spectra are recorded by an optical spectrum analyzer with a typical resolution of 10 nm and 0.1 nm for LED and TLS measurements, respectively.

Selecting TE Polarization

Usually, the PhC structures are characterized for the transmission of TE polarized light as the structures have their largest PBG for this polarization. To assist in selecting the TE polarization of the system, the very pronounced drop in transmission expected at the cutoff of the fundamental PBG mode is used[3] (see e.g. fig. 3.13). The procedure for selecting the TE polarization is as follows (for this procedure it can be beneficial to have an old sample at hand with a well-known position of the cutoff):

1. Place the device-under-test (DUT) in position and align the fibers roughly to the waveguide.

[2]Even though the LED should be randomly polarized it has a slightly preferred axis of polarization. Thus, we use a controller to align this axis to the polarizer.

[3]The method has been verified by use of a Glan-Thomson prism, a polarizer, and the Brewster angle in an earlier and more complicated experiment; see e.g. [103].

2. Go to a wavelength in the transmission window of the PhCW, e.g. in the linear regime of the PhCW.
3. Optimize the transmission through the polarizer and the PhCW by use of polarization controller ♯1.
4. Move to a wavelength expected to be longer-than-but-close-to the cutoff wavelength of the PhCW.
5. Minimize the transmission by use of polarization controller ♯2.[4]
6. Take a single spectrum of the transmission and (try to) locate the cutoff wavelength.
7. Fine-tune the fiber-alignment for high transmission.
8. Optionally, optimize the polarization by repeating the procedure from step 4 and selecting a wavelength closer and closer to the cutoff.

6.1.1 Group Index Measurements

The concept of determining the group-index $n_g(\lambda)$ experimentally is based on the Time-Of-Flight (TOF) method where the *difference* in TOFs for signals propagating through a PhCW and a reference ridge waveguide is measured. Thus, we measure a *change* in the group index caused by the PhCW compared to a conventional ridge waveguide as a function of wavelength, $\Delta n_g(\lambda)$, and not the group index directly. However, the absolute group index in the PhCW can be extracted by an appropriate shift of the measured $\Delta n_g(\lambda)$ curve with respect to FDTD calculations and/or 'expected' reference values away from the cutoff wavelength of the PhCW. This method stands in contrast to the modelling method presented in section 3.3.2 where n_g is determined directly by a direct tracking of the pulse.

The experimental setup is shown in fig. 6.2 and was developed by Rune Jacobsen [104], Beata Zsigri [105], and Christophe Peucheret [106]. With the TLS and amplifiers available at COM•DTU, the setup allows to measure the group index in the wavelength range from $\sim$ 1528 nm - $\sim$ 1565 nm.

The group index change $\Delta n_g(\lambda)$ caused by the PhCW is found by measuring the phase delay of a 19 GHz-modulated signal propagating through the setup including the PhCW. In this way, the envelope phase index of the modulated signal corresponds to the group index of the light. The modulation frequency of 19 GHz is chosen in order to obtain the best temporal resolution. The tradeoff of this choice manifests itself in the spectral resolution, as the high-speed modulation of the light introduces sidebands as discussed in refs. [107, 108]. The phase delay of the modulated signal is measured using a network analyzer, which modulates the signal utilizing a $LiNbO_3$ modulator and detects it again after passing the

[4] As we expect that no TE polarized and only TM polarized light will propagate through the PhCW after the cutoff we can tune in onto the TE polarization in this way.

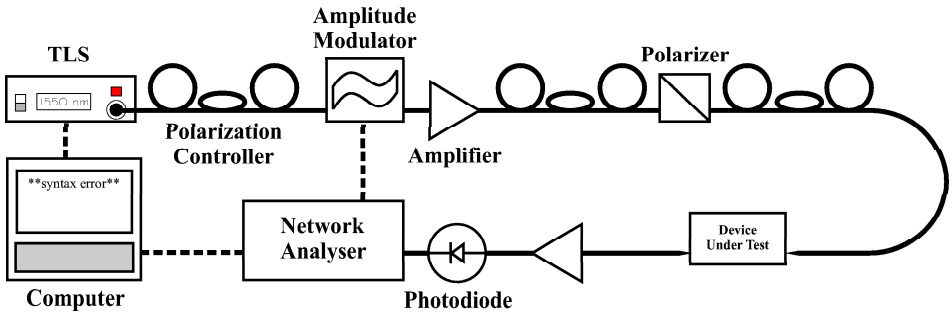

Figure 6.2: Characterization setup for measuring slow-light in nanophotonic waveguides. A TLS delivers a CW signal, which is modulated by a MZ-modulator controlled by a network analyzer. The 19 GHz modulated signal is amplified before its polarization is set using a polarization controller and coupled into the device-under-test using a tapered-lensed fiber. After the device the signal is amplified again before it is detected by a photodiode connected to the network analyzer. A computer controls the laser and reads out the measured phase delay and transmission level as a function of wavelength.

waveguide under test. The measured phase delay of the signal gives the dispersion of the whole setup. In order to obtain the phase delay due to the PhCW alone, $\Delta\phi(\lambda)$, a calibration measurement is made for a conventional ridge waveguide and used for normalization.

The measured phase delay of the modulated signal caused by (the high group index of) the PhCW, $\Delta\phi(\lambda)$, can be used to determine the *change* in group index $\Delta n_g(\lambda)$ of light caused by the PhCW as [108]

$$\Delta n_g(\lambda) = -\frac{\Delta\phi(\lambda)c}{360^0 L_{PhCW} f}. \tag{6.1}$$

Here c is the speed of light, L_{PhCW} is the length of the PhCW, and f is the frequency of the modulated signal. The negative sign is due to that a larger phase delay (more negative $\Delta\phi$) corresponds to a higher group index. The change in the group index determined by this method is partly influenced by Fabry-Perot cavities in the sample, namely between the two end-facets of the sample and the two internal facets between the ridge waveguides and the PhCW. However, these can be accounted for by doing an appropriate averaging of $\Delta n_g(\lambda)$ as discussed in refs. [107, 108]. To obtain absolute values of the group index n_g from the relative change given by eq. (6.1), the vertical offset of the experimental curve is adjusted to match calculated FDTD results obtained from the direct tracking of the pulses and/or to 'expected' values away from the cutoff, i.e. a value around 5 for silicon waveguides.

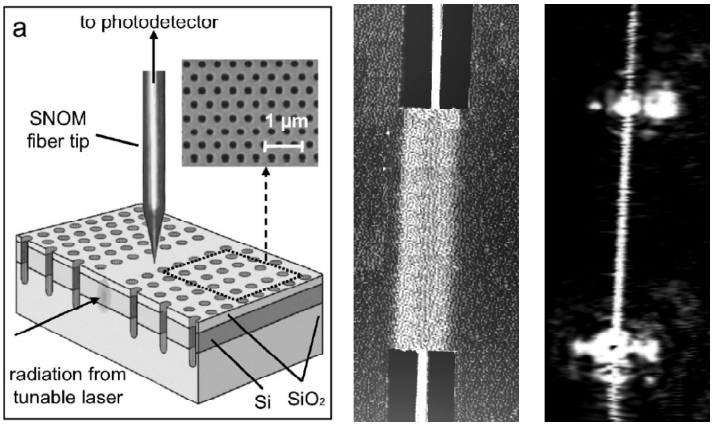

Figure 6.3: (a) Schematic layout of the experimental setup for SNOM. (b) Grey-scale topographical and (c) near-field optical images (22 x 50 μm^2) obtained for TE-polarized light at 1520 nm in a 40-μm-long PhCW. Measurements are done by Valentyn Volkov and published in [113].

6.1.2 Scanning Near-field Optical Microscopy

Scanning near-field optical microscopy (SNOM) can be used to make a direct mapping of light and pulse-tracking in nanophotonic devices [68,109,110]. SNOM measurements have been conducted in the project on selected components by the PIPE partners at the University of Aalborg [111,112]. Figure 6.3 shows a schematic of the setup used for SNOM measurements. It consists of a collection SNOM with an uncoated fiber tip used as a probe and an arrangement for launching tunable 1500 - 1630 nm TE/TM-polarized light into the input ridge waveguide by positioning a tapered-lensed polarization-maintaining single-mode fiber. Following the fiber adjustment, the intensity distribution near the sample surface is probed with an uncoated sharp fiber tip of the SNOM (fig. 6.3(a)). The tip can be scanned along the sample surface at a constant distance of a few nanometers maintained by shear force feedback. Near-field radiation scattered at the tip is partially collected by the fiber itself and propagates to the end of the fiber, where it is detected by a photoreceiver. In this way, near-field images as shown in fig. 6.3(c) for the PhCW shown in fig. 6.3(b) can be obtained. Here, the confinement of light in the PhCW is clearly seen along with severe out-of-plane scattering at the interfaces between the ridge waveguides and the PhCW.

6.2 Straight Photonic Crystal Waveguides

To start things simple, fig. 6.4(a) shows a typical SEM image of a $\sim 11\mu$m W1 PhCW with $D = 290$ nm and $\Lambda = 400$ nm fabricated utilizing EBL and ICP RIE. The widths of the input and output ridge waveguides are 700 nm to ensure an efficient coupling to the PhCWs [90]. Figure 6.4(b) shows the transmission spectrum obtained using the setup shown in fig. 6.1 and a TLS as source for TE-polarized light. The spectrum has been averaged over over 5 measurements (red) and is plotted with the corresponding standard deviations (black). The measurements have been performed during one day in the lab with numerous measurements and fiber-alignments in between. Thus, the average deviation of $\sim$0.14 dB between the 5 measurements in the transmission window of the PhCW from 1480-1530 nm states a typical drift and accuracy of the setup.

Transmission Spectrum

As seen, the PhCW has a transmission plateau for the part of the mode located above the silica-line in the linear-regime ranging from (below) 1480 nm to 1515 nm with the transmission slightly dropping in the slow-light regime towards a $\sim$30 dB drop in transmission around 1533 nm. This drop corresponds to the cutoff wavelength of the fundamental PBG mode as plotted in the 3D band diagram on top of the graph (no shift applied). The dashed line sketches the (I) linear- and (II) slow-light regime of the fundamental mode. The small discrepancy as indicated by the dotted line between the calculated and measured mode-cutoff is due to uncertainties in the experimental parameters and the limited resolution of the calculation grid. The small peak in transmission located just before the cutoff may correspond to the part of the PBG mode that is below the silica-line and, thus, is fully confined to the PhCW in all dimensions. Above 1533 nm only TM-polarized light and slab modes are present and, hence, the transmission is low as the setup is optimized for the transmission of TE-polarized light.

SNOM images

Figure 6.5 shows images obtained by using the SNOM technique to characterize the transmission through a PhCW with frame (a) showing the topographical image of the waveguide. The left image of the figure shows frames obtained for TM-polarized light at the wavelengths (b) 1500 nm,(c) 1530 nm,(d) 1570 nm,(e) 1600 nm, and (f) 1630 nm. Obviously, TM-polarized light is confined to the waveguide core for all wavelengths. This is no surprise as the average index of the PBG cladding is lower than the waveguide core and TM-polarized light can be guided by total-internal-reflection with low-losses [114]. The PBG effect is nicely illustrated in the right image, which shows SNOM images for TE-polarized light at wavelengths (b) 1500 nm,(c) 1570 nm,(d) 1572 nm,(e) 1590 nm, and (f) 1630 nm. At small wavelengths TE-polarized light is confined to the core and nicely guided. At longer wavelengths the mode starts to penetrate into the PhC cladding

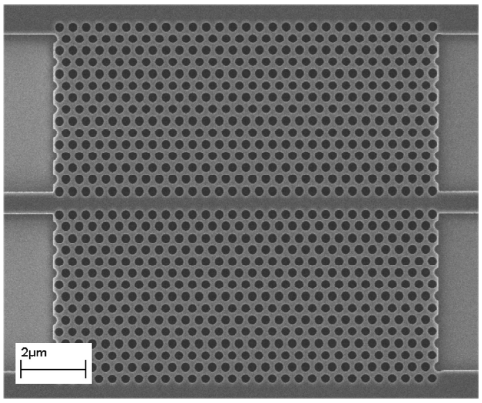

(a)

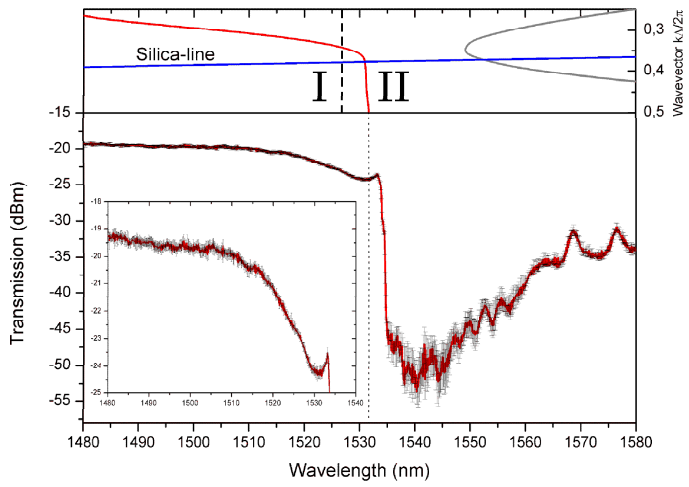

(b)

Figure 6.4: (a) SEM image of a typical $\sim 11\mu$m W1 PhCW with $D/\Lambda = 0.725$ fabricated using EBL. (b) Transmission spectrum for TE-polarized light in the PhCW averaged over 5 measurements (red). The black error bars represent the standard deviation ~ 0.14 dB from 1480 - 1530 nm. Inset shows the zoom-in on the transmission window. Top figure shows the fundamental PBG mode (red) and slab mode(s) (gray). Dashed line marks the (I) linear- and (II) slow-light regime of the fundamental mode.

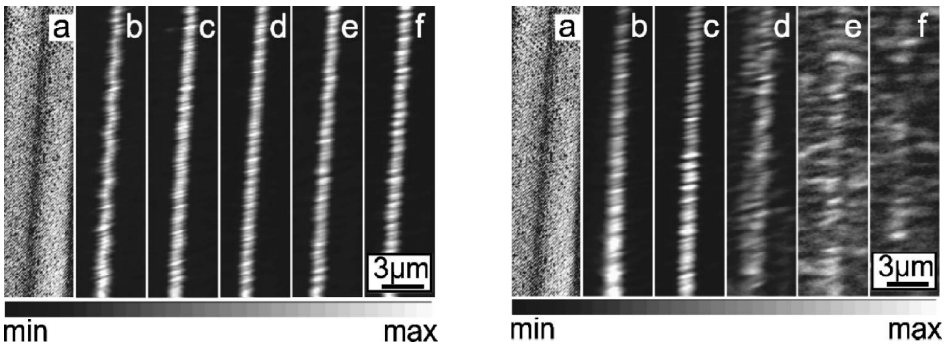

Figure 6.5: (a) Grey-scale topographical and (b-f) near-field optical images ($6 \times 26\mu m^2$) obtained in a 40-μm-long PhCW for [Left] TM-polarized light at the wavelength (b) 1500 nm, (c) 1530 nm, (d) 1570 nm, (e) 1600 nm, (f) 1630 nm and [Right] TE-polarized light at the wavelength (b) 1500 nm, (c) 1570 nm, (d) 1572 nm, (e) 1590 nm, (f) 1630 nm. Measurements done by Valentyn Volkov and published in [110].

and eventually becomes unconfined. After the mode-cutoff around 1572 nm (d) light is expelled from the structure or distributed throughout the structure as a slab-mode.

Nanoimprinted PhCW

In the end of the project, we succeeded in fabricating PhC structures utili-zing NIL and ICP RIE. Unfortunately, the yield of the imprinted structures was rather low and only a few straight waveguides were successfully fabricated. Figures 6.6(a)+(b) show a SEM image of a PhCW fabricated using NIL and the normalized TE-transmission spectrum for the waveguide, respectively. As seen on the SEM image, the imprint of the waveguide turned out nice and rather homogeneous, though, small fluctuations in the hole diameter are observed in the outskirts of the PhC. However, the footprint of the fundamental PBG mode-cutoff around 1600 nm is clearly seen as the sharp ∼20 dB drop in the transmission spectrum. Thus, it is possible to utilize NIL to fabricate nanophotonic waveguides that holds a PBG effect making NIL a promising technique for mass-fabricating PhCWs. However, as discussed in sec. 5.3 there are issues to overcome in order to increase the yield of successfully fabricated structures.

Propagation Loss in the W1 PhCW

To estimate the propagation loss for TE-polarized light in a SOI W1 PhCW several waveguides of different lengths have been fabricated and characterized. Figure

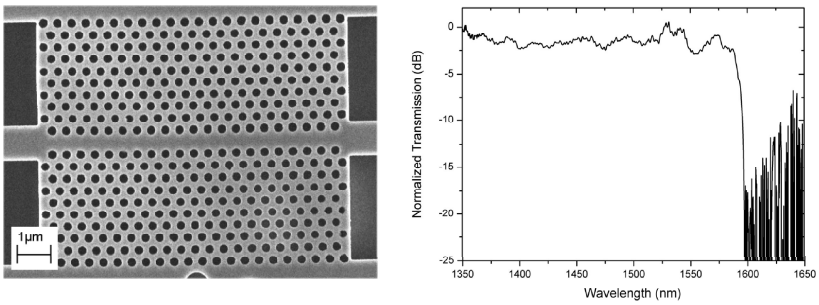

(a) (b)

Figure 6.6: (a) SEM image of a typical $\sim 10\mu$m W1 PhCW with $D/\Lambda = 0.625$ fabricated using NIL. (b) Transmission spectrum for TE-polarized light in the PhCW.

6.7(a) shows the obtained transmission spectra in the wavelength region of interest recorded with a resolution of 0.1 nm for PhCWs fabricated utilizing EBL with lengths 10, 25, 50, 75, and 100 μm. The spectra have been normalized to the transmission spectrum of a ridge waveguide of similar length, and it is apparent, that the SOI PhCW shows a rather high propagation loss for all wavelengths. Approaching the cutoff wavelength at 1533 nm the transmission level decreases rapidly from $\sim$ 1510 nm. No low-loss window arising from the part of the mode lying below the silica-line is evident. The measured propagation loss for the fabricated PhCWs is shown in fig. 6.7(b). The propagation loss takes a minimum value of 'astonishing' $\sim$175 dB/mm. This does not come as a surprise as most of the mode is located above the silica-line and, thus, is leaky in the vertical direction. Near the cutoff wavelength the propagation loss seems to increase, however, the error bars resulting from the increased noise (lower transmission level), make it difficult to interpret. Thus, the SOI PhCW is indeed a lossy candidate for routing light and has, if any, a very narrow low-loss bandwidth. Even if the PhC devices only need to be tens of micrometers in length the loss figures presented here are unacceptably high.

For comparison fig. 6.8 shows the calculated propagation losses utilizing 3D FDTD for W1 PhCWs realized in the SOI (blue) and membrane (red) configurations. The error bars represent the standard deviation. The maximum length of the PhCW used in the 3D calculation was limited to 30 μm due to high memory requirements. The 3D band diagram for the fundamental PBG mode is plotted on top in the figure (no shift applied) along with the light-line (red) and the silica-line (blue). Clearly, the FDTD calculation for the SOI configuration predicts a minimum loss around 140 dB/mm, which is in agreement with the measured loss. As sketched by the dashed lines in the figure, the minimum loss for the SOI PhCW

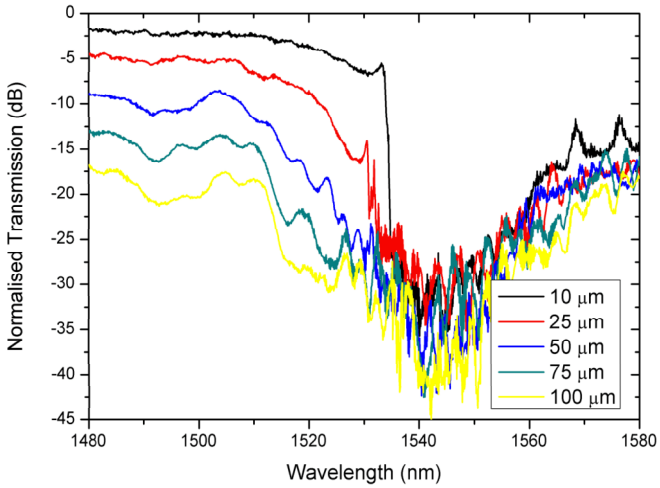

(a)

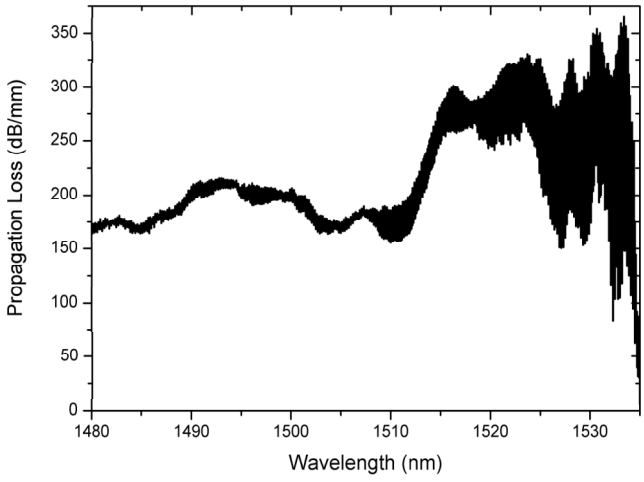

(b)

Figure 6.7: (a) Transmission measurements for PhCWs of different lengths with $D/\Lambda = 0.725$ fabricated utilizing EBL. (b) Measured propagation loss with error bars for the SOI W1 PhCW.

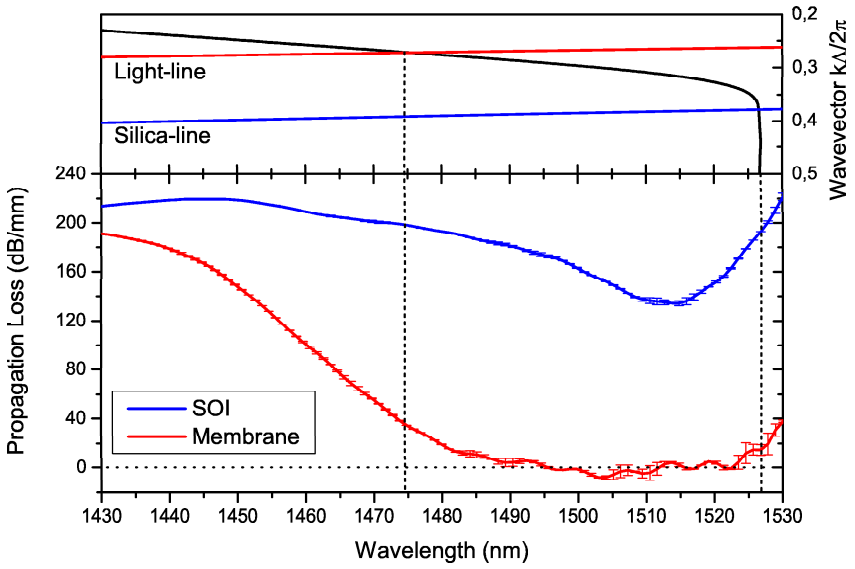

Figure 6.8: [Bottom graph] Calculated propagation losses for the SOI (blue) and membrane (red) W1 PhCW. [Top graph] The 3D band diagram for the fundamental PBG mode (black), the silica-line (blue), and the light-line (red). The lowest propagation losses are obtained in the wavelength region where the mode is below the light-line.

is obtained in the wavelength range where the mode is below the *light-line* of the slab and, thus, can only scatter to the silica as it is still above the *silica-line*. The membrane waveguide is predicted to have a ∼30 nm wavelength region with a propagation loss lower than 10 dB/mm, which is attributed to the placement of the light-line in respect to the fundamental mode. The ripples in the spectrum and negative losses stems from numerical artifacts when calculating near-zero losses and using limited lengths of the PhCWs.

At present time, no experiments have been conducted at COM•DTU on PhC devices in membranes. However, different research groups have indeed obtained low propagation losses below 10 dB/cm (yes, centimeter!) in such PhCWs in bandwidths up to ∼50 nm [34, 90, 115, 116]. The propagation loss in membrane PhCWs is, presumably, limited only by the sidewall and surface roughness of the PhC structure [61]. Thus, membrane PhCWs may be utilized to obtain low propagation losses in PhC devices.

Approaches in reducing the propagation loss in PhCWs have typically included changing the waveguide width utilizing e.g. W0.7, W1.1, or W2.7 PhCWs [116–118]. However, as mentioned in section 3.2.5 changing the width of the PhCW also changes the dispersion properties and should be accounted for if e.g. low-loss devices utilizing slow-light is to be realized.

6.3 Photonic Crystal Waveguide Bends

In PhC devices it may be inevitable to have waveguide bends in order to redirect or skew light into a given direction. However, bends form severe discontinuities in the PhCW and may excite higher-order modes, which are not necessarily guided in the PhCW. Moreover, the behavior of PhCW bends are resonant in nature and have limited bandwidths one order of magnitude smaller than the bandgap with bend losses down to 1-2 dB at single frequencies [119–122]. Thus, the designing of PhCW bends is non-trivial and needs to be done with care. This section presents experimental results on 60^0, 90^0, and 120^0 PhCW bends.

6.3.1 The 60 Degree Bend

Due to the triangular lattice configuration utilized in this project, PhCWs are naturally bent in steps of 60^0, thus, making the 60^0 PhCW bend a key component. Therefore, a large effort has been put into optimizing the transmission characteristic of the 60^0 PhCW bend.

The investigated PhCWs have two consecutive 60^0 bends in order to have the output of the PhCW parallel to the input. The distance between the two bends has been chosen arbitrarily, but sufficiently long, to achieve steady-state behavior of the PBG mode in the waveguide section separating the bends so that the bends can be treated as separate components. To extract the bend losses, the measured transmission spectrum is normalized to the transmission spectrum for a straight PhCW of similar length.

The Edisonian Bends

Figure 6.9(top) shows the SEM image of a generic 60^0 bend and its corresponding measured bend loss. As seen, the bend introduces a loss around 7-8 dB in a broad wavelength range and only goes below 1 dB in a $\sim$20 nm bandwidth with an average bend loss of 0.6 ± 0.2 dB from 1463-1486 nm. Naturally, for a PhC device designed to operate in a broad wavelength these loss figures are unacceptably high.

Early in the project, we relied on the Edisonian approach when optimizing PhC structures. Figures 6.9(middle) and (bottom) show two of such examples trying to expand the low-loss bandwidth of the generic 60^0 bend. The design strategy was to smoothen the bend in order to decrease reflections and to avoid higher-order modes to be excited in the bend-junction [72]. Basically, the optimized designs include holes which have been moved, removed, or enlarged. As seen from the graphs, it has been possible to affect the loss figure for the generic 60^0 bend. The middle design shows an average bend loss of 0.6 ± 0.2 dB in the wavelength range from 1368-1407 nm and, in practice, a near-zero bend loss from 1560 - 1575 nm (experimental values below zero are artifacts originating from the normalization). These low-loss bandwidths are also predicted by 3D FDTD calculations (red) as shown in the middle graph. The optimized bend shown in fig. 6.9(bottom) have a noteworthy broad and spectrally flat bandwidth from 1510-1550 nm with an average bend loss of 1.12 ± 0.09 dB.

The Topology-Optimized Bend

As presented in chapter 4 we have utilized topology optimization to optimize the broadband performance of the 60^0 PhCW bend. Figure 4.2(b) showed the resulting topology-optimized design along with the steady-state behavior in fig. 4.3(b). The topology optimization was done by Jakob S. Jensen at MEK•DTU. A comparison between the actual fabricated bend shown in fig. 6.10(a) and the design in fig. 4.2(b) reveals that the fine-details in the design has not been transferred to the silicon in the fabrication process. This is mainly caused by broadening of the PhC structures in the conventional RIE etch. Despite this, the measured bend loss shown in fig. 6.10(b) (green) is below 1 dB in a 200 nm spectrally flat wavelength range from 1250 - 1450 nm with an average bend loss of 0.43 ± 0.27 dB. For comparison, the bend loss for the generic bend is also plotted (red) and, thus, it is evident that the topology optimization has dramatically boosted the broadband performance of the 60^0 bend. However, the choice of wavelengths used in the optimization have resulted in a poorer performance of the topology-optimized bend in the slow-light regime near the cutoff wavelength; here around 1490 nm. In a later section, it will be presented how the topology optimization scheme can be applied to optimize the 60^0 bend for the transmission of slow-light.

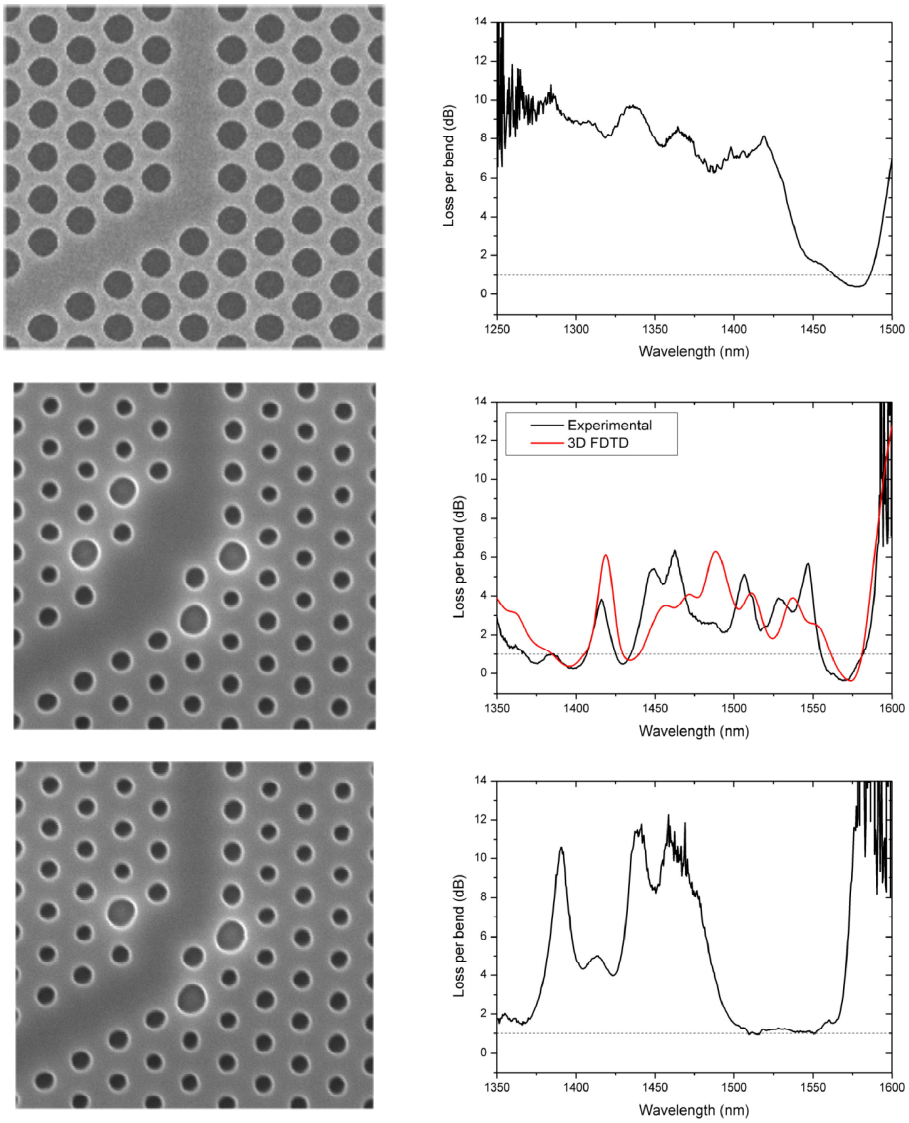

Figure 6.9: SEM images (left) and bend losses (right) for the (top) generic and two (middle)+(bottom) optimized 60^0 PhCW bends. Published in ref. [70](middle) and ref. [123](bottom). The dotted lines mark a bend loss of 1 dB. The filling factor of the PhC structures is not the same for the structures.

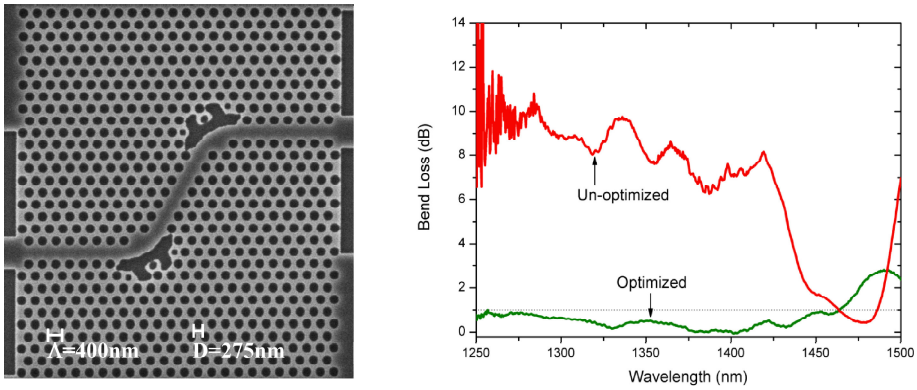

Figure 6.10: (a) SEM image of a fabricated PhCW containing two topology-optimized 60^0 bends. Fabricated in collaboration with ph.d. student Anders Harpøth. (b) Measured bend loss for the optimized (green) and the generic (red) bend. Dotted line marks a bend loss of 1 dB. Published in ref. [86].

6.3.2 The Double 90 Degree Bend

A double 90^0 bend in a PhCW may be used to provide an offset transition to a waveguide over a very short distance. Such a bend is unnatural in a triangular hole configuration due to the inherent lack of 90^0 symmetry and a satisfactory performance is difficult to obtain. Again, we adopt the topology optimization scheme for the optimization of broadband transmission through the double 90^0 bend shown in the top-left SEM image of fig. 6.11. The chosen design area in the optimization done by Jakob S. Jensen at MEK•DTU is marked in red. The optimized design is seen in the top-right SEM image of the figure and is quite non-trivial and different from traditional photonic crystal structures. Nevertheless, the measured bend loss (green) for the topology-optimized structure is found to be below 1 dB in the wavelength range form 1250-1450 nm with an average bend loss of 0.78 ± 0.19 dB. This is in contrast to the un-optimized bend having a bend loss (red) above 5 dB in the whole range.

6.3.3 The Double 120 Degree Bend

Although a PhCW with two consecutive 120^0 bends (Z-bend) may have limited practical applicability, it is a difficult and challenging design problem [125] that served as an excellent benchmark in the project to demonstrate/test the use of topology optimization in nanophotonics. Figure 6.12(a) shows a SEM image of the resulting Z-bend from the topology optimization done by Jakob S. Jensen at

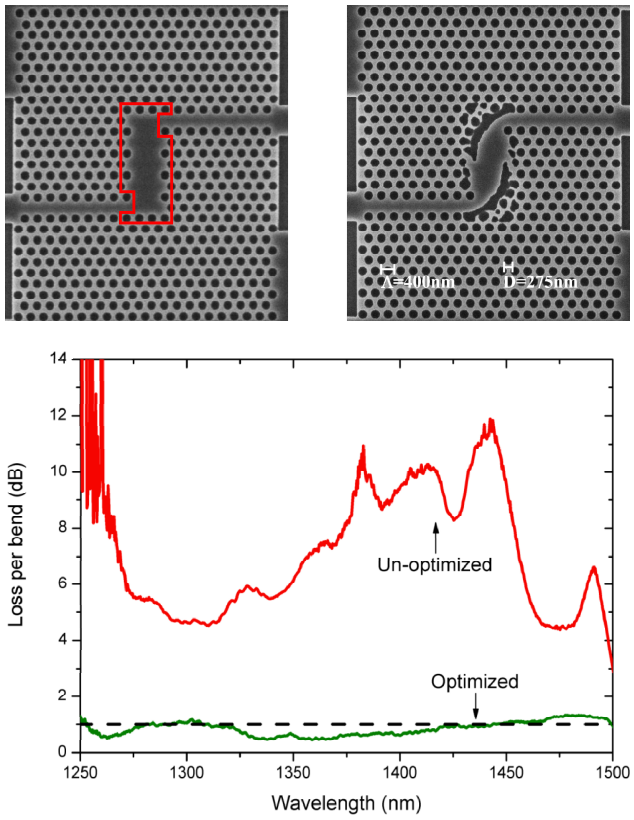

Figure 6.11: SEM images of the double 90^0 bend to be optimized (top-left) utilizing topology optimization with the design area marked in red and the resulting optimized structure (top-right). The graph shows the measured bend loss for the generic bend (red) and the topology-optimized bend (green). Fabricated in collaboration with ph.d. student Anders Harpøth. Published in ref. [124].

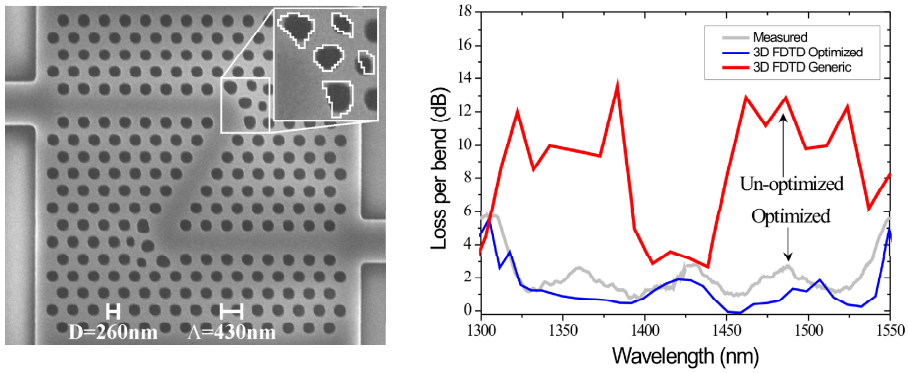

(a) (b)

Figure 6.12: (a) SEM image of the fabricated Z-bent PhCW. The white contours in the inset illustrate the shape of the optimized PBG elements in the design. (b) The measured (gray) and 3D FDTD calculated (red) loss per bend for TE-polarized light in the fabricated structure. Also shown is the 3D FDTD calculated bend loss for the un-optimized (black) Z-bend. Fabricated in collaboration with ph.d. student Anders Harpøth. Published in ref. [81].

MEK•DTU. The white contours in the inset show the shape and form in the design file of the 5 optimized PBG elements in the bend-junction of the waveguide. By inspection, it can be seen that the fabricated holes in the junction are different from those in the design file. This is caused by an unfocused e-beam during fabrication due to imperfect filament conditions[5]. Comparing the topology-optimized design for the Z-bend to the previously presented 60^0 and 90^0 bends it is noted that the bend-junction still has structural features more similar to a PhC structure. This is in contrast to the smoothened junctions of the 60^0 and 90^0 bends, resembling more conventional strip waveguide bends with an etched mirror [126]. This demonstrates the major strength of the topology optimization design-method: the superior type of structure does not need to be known in advance; it will appear from the optimization procedure. The measured loss per bend for TE-polarized light sent through the fabricated Z-bend (gray) is shown in fig. 6.12(b). Also shown in the figure are the calculated losses, obtained by employing 3D FDTD calculations, for the fabricated (red) and the un-optimized (black) Z-bend. The most prominent feature of the spectra is the extremely broad wavelength range of more than 200 nm having a low bend loss just above $\sim$1 dB. Without topology optimization 3D FDTD calculations show up to $\sim$10 dB higher loss per bend. It is worth noting that the low bend loss is obtained experimentally even though the fabricated structure deviates slightly from the optimized design as was also the case for the 60^0 bend. This fact proves the robustness of the topology-optimized design for experimental fabrication tolerances; at least for components optimized for broadband performance.

6.4 T- and Y-Splitters

Efficient splitting of light is widely used in photonics in e.g. interferometers and (de)multiplexors. Specifically, the important Mach-Zehnder interferometer requires splitting of light 50/50 into two waveguides, in nano-photonics preferably using as little space as possible. In the project, photonic wire T-splitters and photonic crystal Y-splitters have been investigated and the results are presented here.

6.4.1 Photonic Crystal Waveguide Y-Splitters

Inherently in the present configuration, the PhC Y-splitter formed by the intersection of three PhCWs at 120^0 is the most convenient configuration for the splitting of light. However, the Y-junction constitutes a severe discontinuity in the input PhCW and the splitting efficiency may suffer from scattering effects, reflections, and the generation of unsupported higher-order modes. To date, only few structures realizing splitters in the PhC platform have been reported [73, 127–130].

[5]These structures were written while the e-beam faciilty was still located at Zarlink Semiconductors in Stockholm, Sweden.

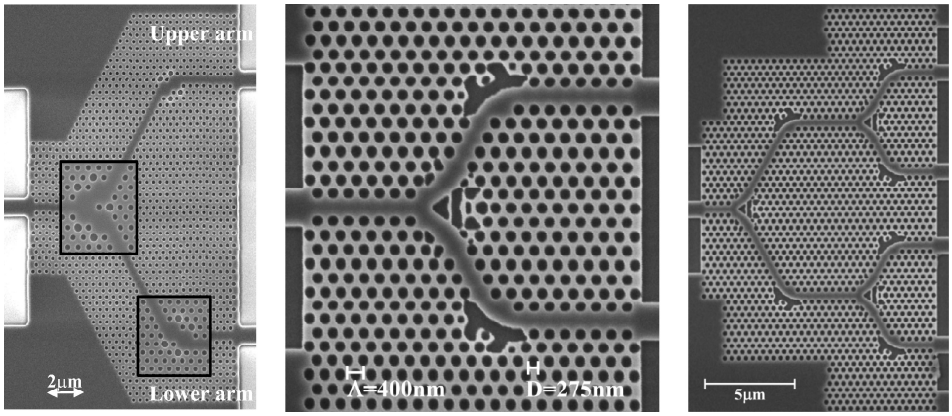

Figure 6.13: SEM image of PhC Y-splitter optimized using (a) a Edisonian approach and (b) topology optimization. (c) 1x4 PhC splitter constructed from three topology-optimized PhC Y-splitters. Published in refs. [131], [132], and [133], respectively.

These are typically realized in Wx (x>1) PhCWs and/or with low splitting efficiencies in limited (single frequency) bandwidths.

Figure 6.13 shows SEM images of two fabricated PhC Y-splitters optimized using (a) the Edisonian approach and (b) topology optimization. Both Y-splitters have been connected to optimized 60^0 bends to have the output wave-guides running parallel to the input waveguide. The splitters are very compact in size with footprints smaller than (a) 15μm $\times 20\mu$m and (b) 10μm$\times 15\mu$m. The Edisonian Y-splitter has been fabricated using DUV lithography in collaboration with partners in the PICCO project. The design strategy for the Edisonian Y-splitter has been to smoothen out the discontinuities of the Y-junction by removing and enlarging holes on both sides of the junction similarly to what was done for the 60^0 bend in use and shown in fig. 6.9(middle). A hole is added in the splitting region, whereby the size of the junction cavity is reduced, thus, avoid creating a multi-moded cavity in the Y-junction. The topology-optimized Y-splitter has been fabricated using EBL and standard RIE at DANCHIP and has been optimized for broadband performance. It is seen that the resulting design has been smoothened on the outer side of the junction and has several complex structures forming a Bragg-like Y-junction. The topology optimization has been done by Jakob S. Jensen at MEK•DTU.

The normalized transmission spectra for the Edisonian (black) and the topology-optimized (blue) Y-splitters are shown in fig. 6.14 with the dashed 3-dB line corresponding to zero excess loss for the splitters. Each curve represents the aver-

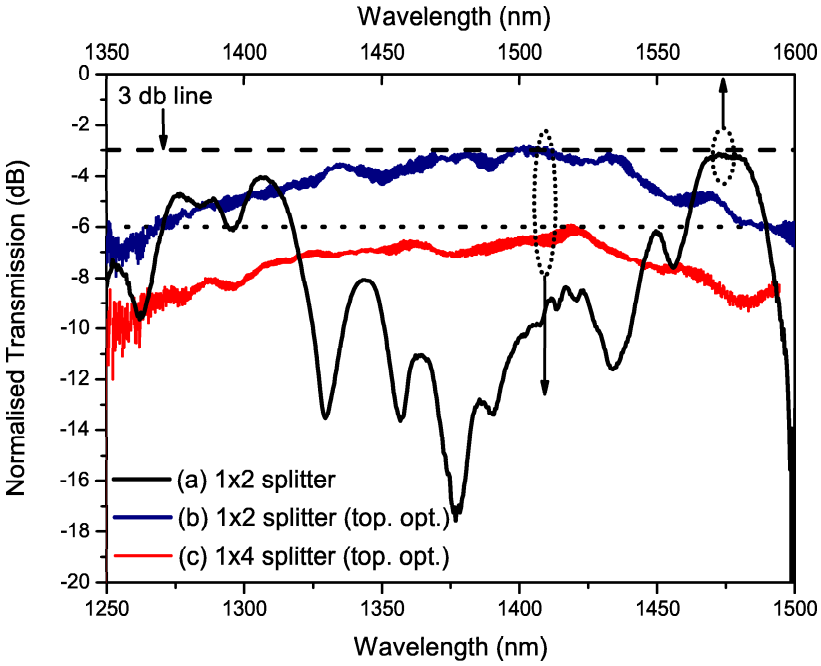

Figure 6.14: Normalized transmission spectra for the Edisonian Y-splitter (black), the topology-optimized Y-splitter (blue), and the 1×4 splitter (red). The spectra are the average of the output ports of the splitters. The dashed and dotted lines represent zero and 3 dB excess losses, respectively.

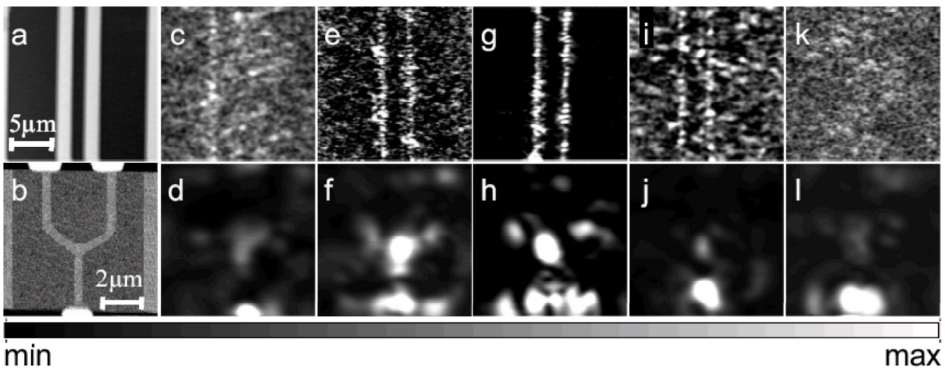

Figure 6.15: Gray-scale topographical of (a) the output ridge waveguides (light gray) of a (b) PhC Y-splitter. (c-l) Near-field optical images taken of (a) and (b) at the wavelengths (c, d) 1530, (e, f) 1540, (g, h) 1550, (i, j) 1560 and (k, l) 1570 nm for TE-polarized light propagating upwards in the vertical direction. Measurements done by Valentyn Volkov and published in [134].

age taken over the two output ports and include losses introduced by the bends. For the Edisonian Y-splitter, the average excess loss is found to be 0.26±0.06 dB in the range 1560-1585 nm and 2-3 dB from 1370-1410 nm. Both of these regions overlap with the low-loss regions of the 60^0 bend as presented in fig. 6.9(middle). Thus, the performance of the Y-splitter may be improved by optimizing the bends further. In contrast to the rather resonant behavior of the Edisonian splitter, the topology-optimized splitter displays a smooth and low-loss 100 nm bandwidth with an average excess loss of 0.44±0.29 dB from 1350-1450 nm. Hence, the topology-optimized design opens up for a practical implementation of the PhC Y-splitter without the need for delicately matching a narrow operational bandwidth of the Y-junction to the bandwidth of other parts of the PhC component.

Figure 6.13(c) shows a SEM image of a 1×4 PhCW splitter constructed from three topology-optimized PhC Y-splitters without drawing special attention to the spacing between adjacent junctions representing discontinuities in the component. The average transmission from the four output ports normalized to the spectrum for a PhCW of similar length is shown in fig. 6.14 (red) with the dotted 6-dB line corresponding to zero excess loss. The curve shows an average excess loss of 1.55 ± 0.54 dB for a 100 nm bandwidth and includes losses from two Y-junctions and two bends. This excess loss may be acceptable in a real circuit but can be decreased by reducing the roughness of the topology-optimized elements, hence, reducing scattering effects in the junctions. The 1×4 PhCW splitter is a nice demonstration of how individual topology-optimized parts can be used as building blocks to realize nanophotonic circuits.

The splitting of light in a PhC Y-splitter has been mapped utilizing SNOM.

Figure 6.15 shows a topographical of (a) the output ridge waveguides of a (b) PhC Y-splitter[6]. Figure 6.15(c-l) show the near-field optical images taken at the wavelengths (c,d) 1530 nm, (e,f) 1540 nm, (g,h) 1550 nm, (i,j) 1560 nm, and (k,l) 1570 nm for TE-polarized light propagating upwards in the vertical direction through (c,e,g,i,k) the output waveguides and (d,f,h,j,l) the splitting region. As seen, the performance of the Y-splitter is very wavelength dependent, which is a clear evidence of the PBG effect in the structure[7], and only splits light effectively in a narrow bandwidth centered around (g,h) 1550 nm with rather symmetrical field distributions in the output waveguides. It is obvious that the Y-junction and the bends make up severe scattering centers in the component as light is heavily scattered out-of-plane. Presently, the second generation of topology-optimized splitters presented in this section is being characterized by SNOM and the images may reveal new information of the splitters and help in further optimizations.

Wavelength Dependent PhC Y-Splitter

Optical filters are of great importance in wavelength-division multiplexing systems e.g. for filtering out specific signals carried by different wavelengths. As a first demonstration, we have utilized topology optimization to design a simple and coarse nanophotonic filter based on PhCs that splits incident light into lower and higher wavelengths. The design has been employed into a PhC Y-splitter so that TE-polarized light at lower wavelengths is directed to one arm and light at higher wavelengths is directed to the second arm of the PhC Y-splitter. The design and optimization has been done by Jakob S. Jensen, MEK•DTU and fabricated at DANCHIP. Figures 6.16(a)+(c) show the SEM images of the PhC wavelength dependent Y-splitter fabricated utilizing (a) NIL and (c) EBL. Ridge waveguides are used for routing light to and from the Y-splitter. As seen, the topology-optimized Y-junction contains several complex elements that would be impossible to reach by using the Edisonian approach. A clear physical explanation of the resulting design is presently not known. The inset of fig. 6.16(c) shows the looks of the Y-junction in the design file. By careful inspection it may be seen that the fabricated PBG elements in the junction have been smoothened due to line-broadening in both fabrication procedures. Figures 6.16(b)+(d) show the normalized transmission spectra measured with a LED for the lower (solid black) and upper (solid red) arm of the splitters. Also plotted in fig. 6.16(d) are the FDTD calculated spectra (dotted black and dotted red) with a 2% blue-shift for the fabricated component. Clearly, the splitters show wavelength dependent transmission in the arms, which is nicely predicted by the FDTD calculation and have extinction ratios reaching $\sim$15 dB. However, the performance and bandwidth of the splitters may be degraded by the line-broadening in the fabrication procedure that has smoothened

[6]This is a first generation topology-optimized PhC splitter, which is not presented in the thesis. It was one of the 'poor performers'.

[7]SNOM images obtained for TM-polarized can be found in [134] and does not show this strong wavelength dependency of the transmission through the PhC structure. However, they show rather asymmetrical splitting.

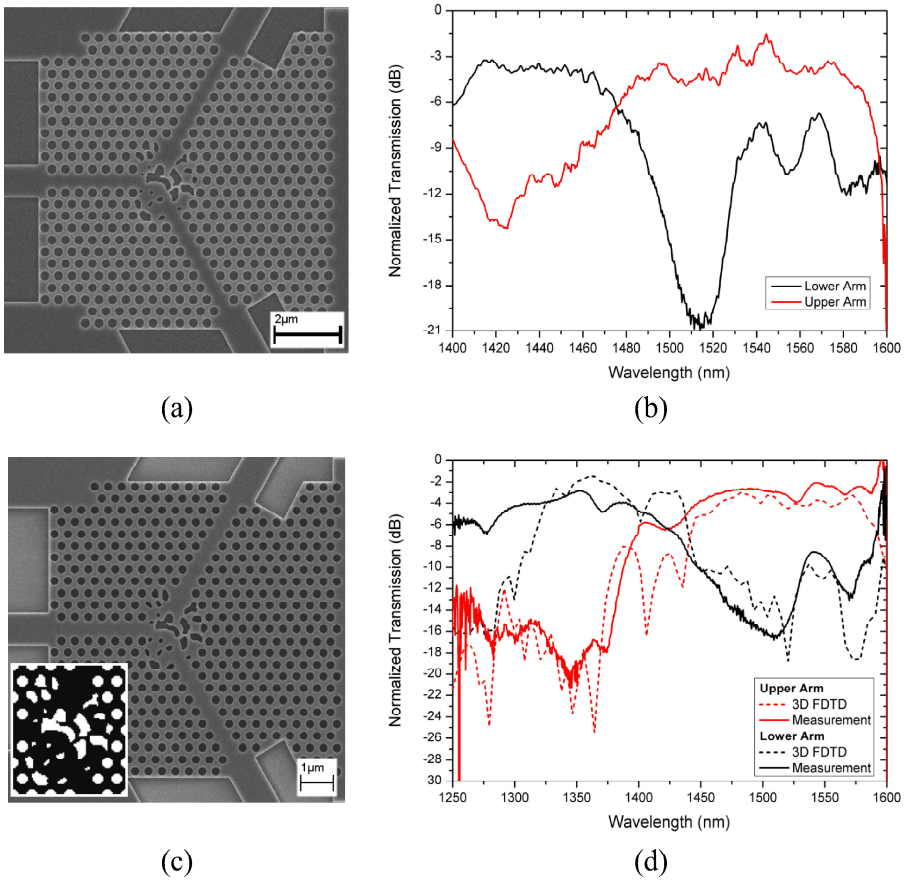

Figure 6.16: SEM image of the fabricated wavelength dependent PhC Y-splitter utilizing (a) NIL and (c) EBL. Inset of (c) shows the Y-junction in the design file. Experimental and normalized transmission spectra for the lower arm (solid black) and upper arm (solid red) of the splitter fabricated by (b) NIL and (d) EBL. Dotted curves in (d) are the corresponding 3D FDTD calculated transmission spectra.

the critical and fine-details in the Y-junction of the design. Thus, the robustness of the topology optimization scheme may be limited when narrow-bandwidth devices is to be realized. Therefore, the topo-logy optimization scheme is presently being improved to comply to fabrication tolerances and to improve the robustness of the method for narrow-bandwidth functionalities.

6.4.2 Photonic Wire T-Splitter

Presently, the relatively high propagation losses in SOI W1 PhCWs may be too high to make them practical for use in simple routing, bending, and splitting of light in nanophotonic circuits. In the recent years, the fabrication of conventional ridge waveguides in silicon have developed rapidly and propagation losses down to 0.2-5 dB/cm and bend losses of ∼0.1 dB with a bending radius of 1 μm have been demonstrated [1, 5]. Thus, simple passive devices can be realized in ridge waveguides with loss figures superior to the PhCWs.

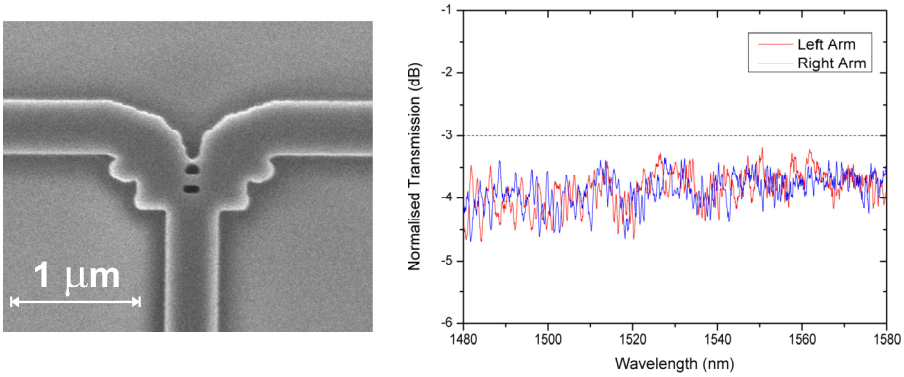

Figure 6.17: (a) SEM image of the fabricated PhW T-splitter. (b) Normalized transmission spectra for the two output arms. Published in ref. [135].

For that reason, we initiated an investigation of utilizing the topology optimization scheme for optimizing photonic wire (submicron-wide ridge waveguides) components with focus on the photonic wire T-splitter splitting light 50/50. The generic photonic wire (PhW) splitter is constructed by combining three PhWs of width 440 nm to form a T-junction with a footprint of only ∼1 μm^2. The topology optimization method is applied to the T-junction to obtain a broad and flat 3-dB splitting of incident light to the two output ports. Figure 6.17(a) shows the fabricated and optimized design. It is seen that the optimized splitter has non-trivial structured parts on the inner side of the bends and small holes in the middle of the

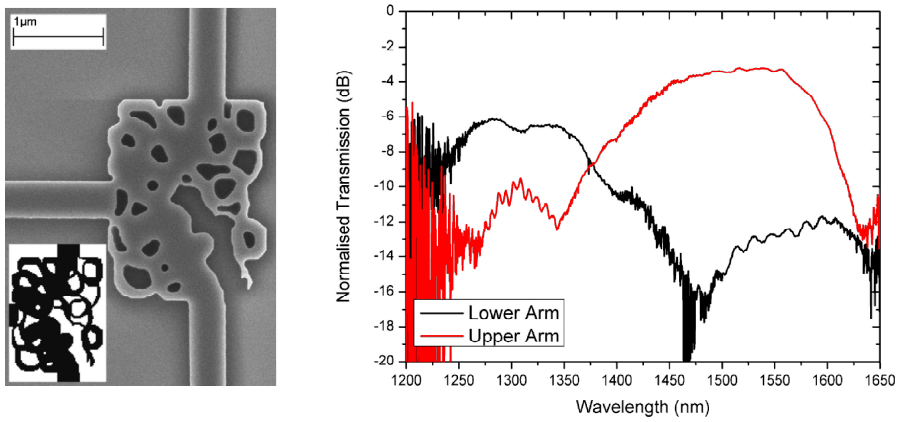

Figure 6.18: (a) SEM image of the fabricated PhW wavelength dependent T-splitter. Inset shows how the T-junction looks in the design file. (b) Normalized transmission spectra for the two output arms.

junction. The normalized transmission spectra for the two output arms are shown in fig. 6.17(b) and reveal similar transmission levels with an average excess loss of 0.88±0.26 dB and 0.86±0.30 for the right and left arm in the full wavelength region, respectively. This is better than previously published PhW T-splitters having larger footprints on the chip with losses of 2.6 ± 0.7 dB [136].

Wavelength Dependent PhW T-Splitter

As was the case for the PhC Y-splitter we also tested the possibility to employ wavelength dependent functionalities into the PhW T-splitter. Thus, the design goal in the topology optimization of the T-junction was to split lower and higher wavelengths to each of their arm. Figures 6.18(a)+(b) show the SEM image and the transmission spectra of the topology-optimized T-splitter. Obviously, the complex structure of the T-junction lead to a wavelength dependent behavior of the T-splitter as lower and higher wavelengths indeed are directed to each their arm, though, the extinction ratio in the arms are lower than that for the PhC splitter. Again, the inset of fig. 6.18(a) indicates that the fine-details of the topology-optimized design have not been transferred to the silicon. Thus, the performance of the splitter may be optimized by reducing the line-broadening introduced in the fabrication procedure and/or implement a fine-detail-filter in the topology optimization scheme to comply to the fabrication tolerances.

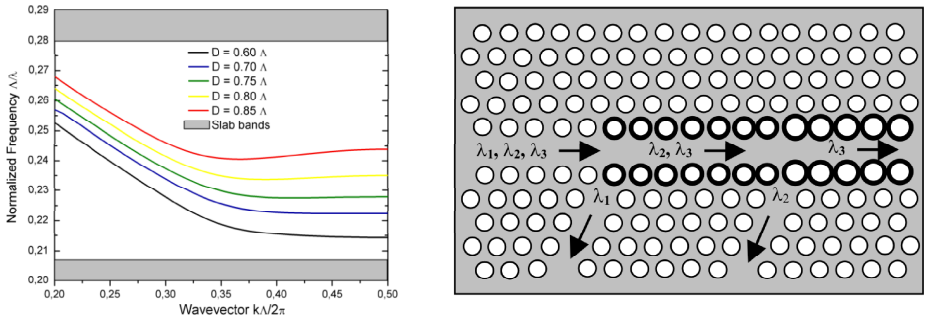

Figure 6.19: (a) Shift of the cutoff frequency of the fundamental photonic bandgap mode for different diameters of the borderholes. (b) Scheme of a 2-channel de-multiplexer realized using a planar photonic crystal waveguide with consecutive sections of large border holes. With this configuration wavelengths are demultiplexed in the order $\lambda_1 > \lambda_2 > \lambda_3$.

6.5 Photonic Crystal Coarse Wavelength Division Multiplexor

The wavelength dependent T- and Y-splitters presented in the previous section constitutes simple demonstrations of how an incoming signal may be divided in space dependent on the wavelength of the signal. As such, the practical usage of these may be limited, however, the concepts may be optimized to perform narrow-bandwidth filtering of optical signals. In this section, a different approach for performing coarse wavelength division multiplexing (WDM) utilizing the PBG effect in PhCWs is presented.

The operation principle of the PhC multiplexor presented here is based on a shift of the cutoff frequency of the fundamental PBG mode in a PhCW and developed by Tapio Niemi [137]. The shift is realized by varying the size of the borderholes adjacent to the waveguide core as presented in section 3.2.7 and shown in fig. 6.19(a) for a PhCW with $D = 0.60\Lambda$. As the diameter of the borderholes is increased, the edge of the transmission band shifts to shorter wavelengths. By enlarging the size of the borderholes in consecutive sections along the PhCW, this effect can be used to successively block a narrow wavelength band near the low-frequency transmission edge for being transmitted. The wavelength shift of the fundamental mode related to the diameter of the borderholes has been found to be $\sim$2 nm/nm in our device. Wavelengths falling outside the transmission band cannot propagate further in the waveguide. Hence, the main part of the

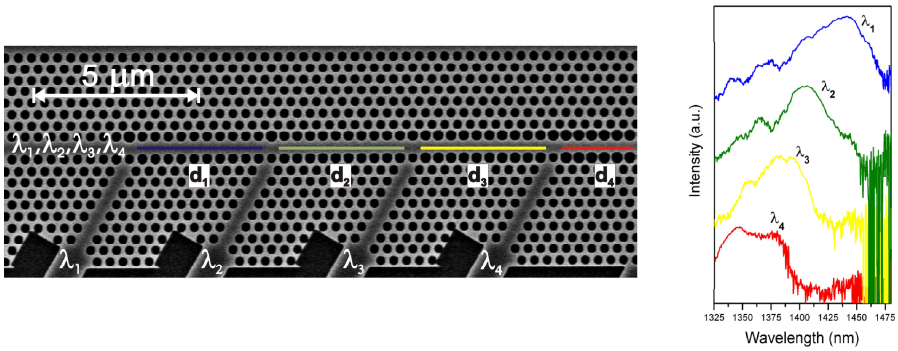

Figure 6.20: (a) Scanning electron micrograph of the fabricated 4-channel de-multiplexer with different borderhole diameters in consecutive sections. Here $d_4 > d_3 > d_2 > d_1$ and dropping of wavelengths will occur in order $\lambda_1 > \lambda_2 > \lambda_3 > \lambda_4$. The length of each of the waveguide sections d_{1-4} is 10Λ. (b) De-multiplexed wavelength channels from the fabricated component. Published in ref. [138].

light is reflected back and may be collected by an appropriately placed PhCW. In effect, a wavelength channel is de-multiplexed from the incident signal to the adjacent PhCW. Therefore, a PhCW having consecutive sections with modified borderholes can be applied as a multichannel optical de-multiplexer. The scheme and the operation principle of a two-channel de-multiplexer are displayed in fig. 6.19(b). The key issue in the operation of the proposed de-multiplexer is to collect the signals to the drop channels. In the present configuration, the intersections between two waveguide sections with different borderhole diameters are slightly optimized by applying a large hole opposite to the drop channel.

A SEM image of a fabricated four-channel de-multiplexer is displayed in fig. 6.20(a). The figure shows the input PhCW and the four drop channels, which are connected to ridge waveguides that are bent smoothly to have the exit ports aligned parallel to the direct transmitted channel of the WDM component. The bulk holes of the PhC have a diameter of 260 nm and the pitch $\Lambda = 380$ nm. The diameter d_{1-4} of the borderholes in the PhCW is designed to gradually increase in steps of 20 nm between consecutive sections with lengths of 10Λ.

The measured spectra for each of the de-multiplexed channels are displayed in fig. 6.20(b) and indeed verifies the operational principle. The different drop channels peak around 1345, 1385, 1405, and 1440 nm for the channels λ_4, λ_3, λ_2, and λ_1, respectively. However, the width of each dropped wavelength channel, the loss, the crosstalk, and the varying channel spacing calls for further improvement and optimization before this component can be utilized in practical applications.

Also, further modelling is needed to understand and optimize the complex coupling mechanism of the reflected light to the drop-channels, which include evanescent waves and resonance effects. For this, topology optimization may be utilized to improve the general characteristics of the component.

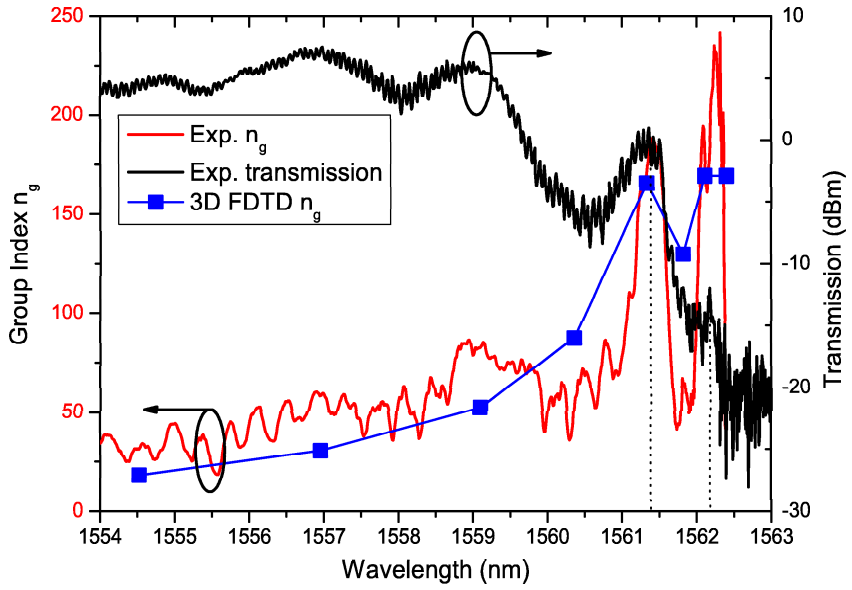

Figure 6.21: Measured (red) and 3D FDTD calculated (blue) group index for a W1 PhCW. Also shown is the measured transmission of the waveguide (black) with the cutoff wavelength located around 1562 nm. The numerical data have been shifted 2.7 % to match the wavelength scale of the experimental data. Calculation has been done by Andrei Lavrinenko and measurements have been done by Rune Jacobsen. Published in ref. [65].

6.6 Slow-Light in Photonic Crystal Waveguides

Experimental investigations of slow-light phenomena in photonic crystal waveguides were initiated in the end of the project. The term 'slow-light' is here defined as light having a group velocity remarkably lower than $\sim c/4$, which is the speed for light in a conventional silicon ridge waveguide. The work done so far

will be presented in this section and has included measuring the group indices for various straight waveguides, optimizing the coupling of slow-light to PhCWs, and improving the PhCW 60^0 bend for transmission of slow-light.

6.6.1 Straight Waveguides

The group index n_g for light propagating in a PhCW is inversely proportional to the group-velocity v_g of light. The group index as a function of wavelength in PhCWs is measured using the setup and method presented in fig. 6.2. To date, we have investigated two types of PhCWs: the conventional W1 and a perturbated W1 waveguide, which was presented in section 3.2.7.

The Conventional W1 PhCW

The holes of the investigated 20 μm W1 PhCW are filled with silica and has a diameter $D = 280$ nm spaced in a lattice with period $\Lambda = 435$ nm. The silicon waveguide core has a thickness of ~216 nm and is encapsulated between glass claddings of approximately 1 μm thicknesses, i.e. the investigated PhCW has (in practice) symmetry in the vertical direction[8]. The transmission spectrum obtained simultaneously to measuring the phase delay of the 19 Ghz-modulated signal is shown in fig. 6.21 (black). The cutoff wavelength of the fundamental PBG mode is seen to be around 1562 nm. Also plotted in the figure are the measured (red) and 3D FDTD calculated (blue) group indices for the PhCW. The 3D FDTD spectrum has been blue-shifted 2.7% and obtained using the TOF method presented in section 3.3.2. The short-period oscillation in the measured group index is due to Fabry-Perot resonances in the waveguide system.

The most distinct feature of the measured curves is the direct experimental observation of an extremely high group index exceeding 230 in a narrow wavelength region near the cutoff wavelength, i.e. light is slowed down by a factor of ~50 in the PhCW compared to a ridge waveguide. This value is one order of magnitude higher than the experimental values we previously obtained using SNOM techniques [110]. The high group index behavior is nicely predicted by the 3D FDTD calculation, however, 'only' reaching a value of 166. Another inte-resting observation is that even though the transmission in general is decreasing when approaching the cutoff wavelength, we clearly measure and calculate local maxima for the transmission in the wavelength ranges where the group index displays local maxima. This observation does not agree with the behavior proposed in ref. [61], where the loss is predicted to grow with increasing group index. The local minimum of the group index around 1561.7 nm is likely to be caused by the finite length of the waveguide. However, it is not yet fully understood and needs further investigations on several PhCWs of different lengths.

[8]The PhCW was encapsulated in silica as it was used in a later experiment requiring electrical contacts on top and isolated from the silicon core.

The practical utilization of slow-light in a PhCW has been demonstrated in a novel experiment[9] including a silicon waveguide having a significant linear electro-optic (χ^2) effect [7]. In the paper, we show that the slow-light properties of the PhCW indeed enhance the light-matter interaction resulting in an exceptionally high χ^2-value for a PhCW fabricated in silicon! The experiment is the first experimental verification of the theoretically predicted [49] linear relationship between group-index and an enhanced non-linear coefficient.

Perturbated W1 PhCWs

Waveguides have been fabricated having their first and second rows of holes changed in diameter compared to the bulk PhC. The chosen parameters are based on the modelling of perturbated waveguides presented in section 3.2.7. Specifically, PhCWs with lengths 10, 25, 50, 75, 100, 150, 250, 500, and 1000 μm, bulk holes of diameter $D = 290$ nm, and $\Lambda = 400$ nm were fabricated. The first/second row of holes is changed by -30/+40 nm in diameter. Figure 6.22 shows the SEM image of a 10 μm perturbated PhCW. The 3D band diagram has been calculated for this set of waveguides and is shown in fig. 6.23(left). Also plotted in the band diagram is the fundamental mode for a W1 PhCW (orange) with similar PhC parameters (inherently, with no change of the first and second row). Figure 6.23(right) shows the measured transmission spectra for the perturbated waveguides of lengths 10 μm (black), 500 μm (red), and 1000 μm (green). For comparison, the transmission spectrum for a 10 μm W1 waveguide (orange) is also plotted. The 3D band diagrams have been shifted $\sim 0.5\%$ in frequency so that the calculated mode-cutoff for the W1 waveguide matches the measured transmission cutoff. The bands for the perturbated waveguide show that the PBG mode is degenerate and is split-up into an even (red) and an odd (blue) mode. The degeneracy of the mode is caused by too large holes of the PhCW and, thus, the modes has been pulled down in frequency allowing for the fundamental mode to interact with the slab-modes as presented in fig. 3.4. Nevertheless, the perturbated waveguides show to have a transmission window nicely matching the bandwidth of the even mode below the silica-line in the band diagram (indicated by the black dotted line). Figure 6.24 shows the measured propagation loss for the perturbated waveguide system and is found to be 4.2 ± 1.4 dB/mm in the range from 1533 nm - 1540 nm[10]. Compared to the W1 mode, the even mode of the perturbated waveguide has been pulled down in frequency and obtained a non-zero slope, which (by simple differentiation) predicts a group index just above 20 in the $\sim$20 nm bandwidth of the mode below the silica-line. However, due to the degeneracy of the mode the optimal profile of the band similar to that shown in fig. 3.10 is not obtained.

The transmission through a 20 μm perturbated PhCW has been calculated using 2D FDTD and is shown in fig. 6.25 (solid blue). Also shown is the measured

[9]The experiment was conducted in collaboration with Rune Jacobsen et al. and the results have been accepted for publication in Nature (2006). Thus, they will not be presented here.

[10]The propagation loss has been calculated by including transmission spectra for all lengths and not only those lengths shown in fig. 6.23.

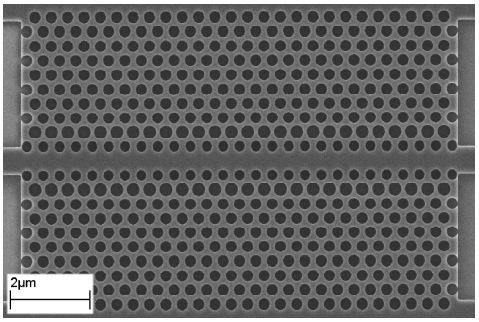

Figure 6.22: SEM image of a 10μm PhCW with D = 290 nm and Λ = 400 nm. The diameter of the first/second row of holes d_1/d_2 have been changed by -30/+40 nm.

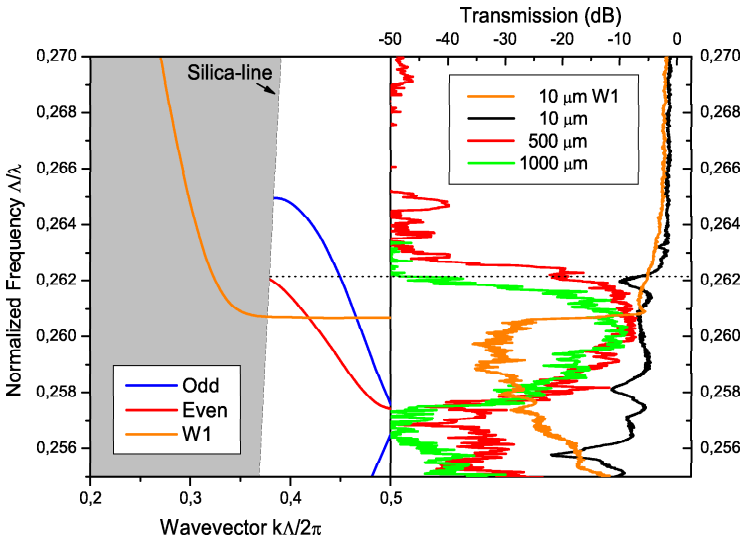

Figure 6.23: [Left] 3D band diagram for the PhCW with diameters -30/+40 nm of the first/second row of holes. The fundamental mode is degenerate resulting in an even mode (solid red) and an odd mode (solid blue). The mode of the W1 PhCW (orange) is also plotted. [Right] Measured transmission spectra for a 10 μm (black), 500 μm (red), and 1000 μm long perturbated PhCW. For comparison the transmission for a 10 μm W1 PhCW is also plotted (orange).

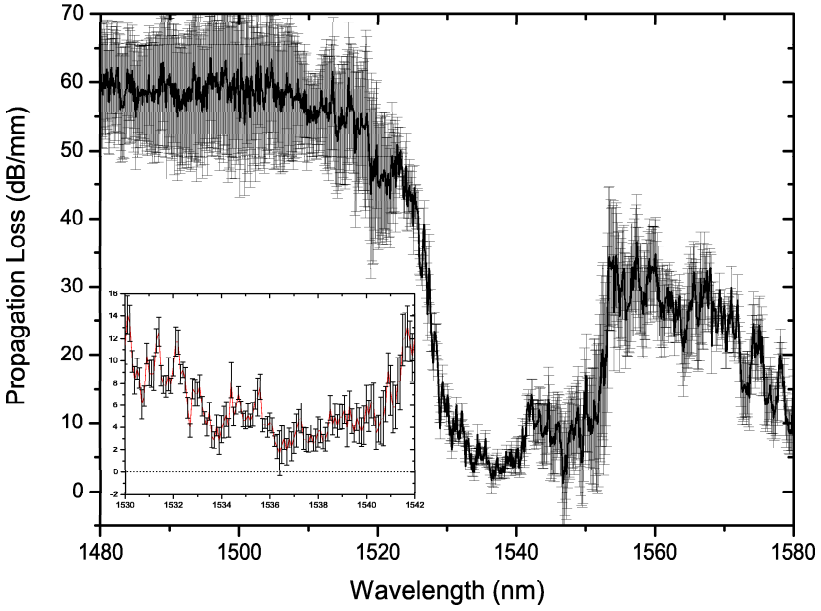

Figure 6.24: Measured propagation loss for the perturbated waveguides with the first row of holes decreased 30 nm and the second row of holes increased by 40 nm. Inset shows a zoom-in on the region 1530 nm - 1542 nm. The average loss is found to 4.2 ± 1.4 dB/mm in the range from 1533 nm - 1540 nm.

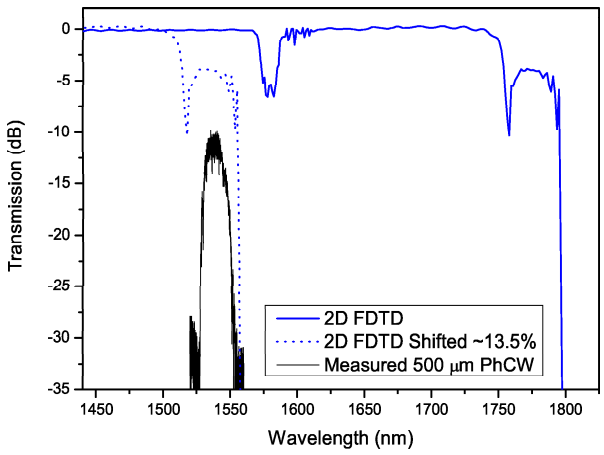

Figure 6.25: 2D FDTD calculation (solid blue) of the transmission through a 20 μm PhCW with perturbed first and second row of holes. The measured transmission (black) through a 500μm perturbated PhCW. The 2D FDTD calculated spectrum is shifted $\sim$ 13.5% (dotted blue) to match the measured transmission.

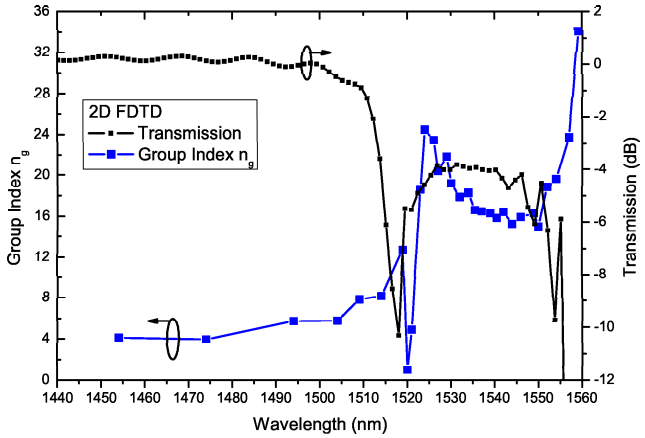

Figure 6.26: The 2D FDTD calculated group index (blue) and transmission spectrum (black) for a 20 μm perturbated PhCW. Both spectra have been blue-shifted ~13.5%.

transmission (black) for the 500 μm perturbated PhCW. In order to match the cutoff wavelength of the 2D calculation to the experiment the 2D FDTD spectrum needs to be shifted ~13.5% (dotted blue). By using the method presented in sec. 3.3.2 the group index of the 20 μm perturbated PhCW has been calculated by using 2D FDTD[11] and the wavelengths have been shifted accordingly to fig. 6.25 to match the experimental wavelength region. Figure 6.26 shows the calculated group index curve (blue) and the 2D FDTD spectrum.

Far away from the mode-cutoff in the linear-regime around ~ 1455 nm the group index is nicely calculated to be around 5 similar to that of a conventional ridge waveguide [20]. The transmission plateau from ~1525 nm - 1555 nm is predicted to have a group index in the range of 20. However, the calculated group index for the waveguide configuration is not constant over the full transmission plateau as desired and shown in fig. 3.10. At the mode-cutoff around 1555 nm the group index rises to extreme values similar to what is the case for the W1 PhCW.

The measured group index of a 500 μm perturbated PhCW is shown in fig. 6.27 (red) along with the calculated group index (blue), the measured transmission (black), and the even mode from fig. 6.23 shown in the top graph. The absolute measured group index has been obtained by shifting the measured group index-change vertically to match the level of the calculated values. Unfortunate, for determining the group index of the perturbated waveguides using this TOF method

[11] Narrow pulses with a width of 1 nm were used calculating over 524288 time-steps.

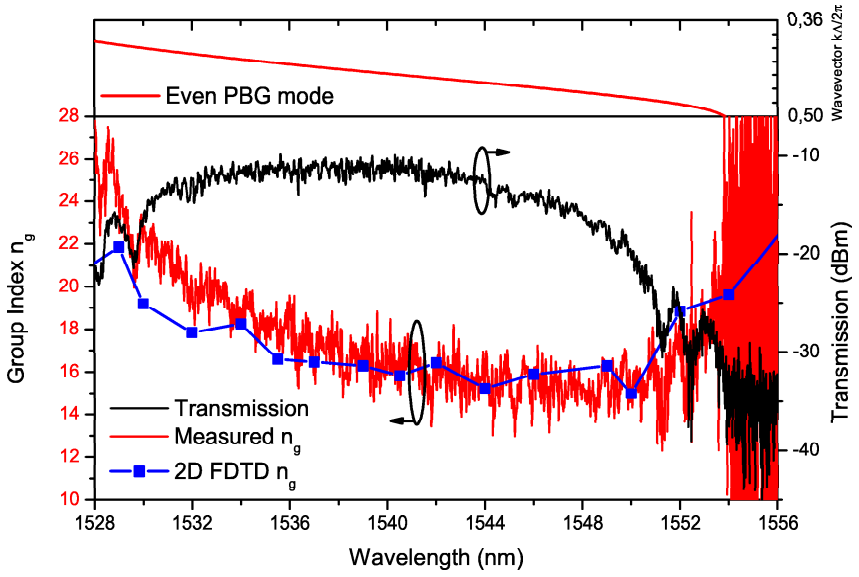

Figure 6.27: The measured (red) and calculated (blue) group indices for a perturbated PhCW. The measured group index-change caused by the PhCW has been shifted vertically to match the calculated values. Also shown is the measured transmission spectrum for the 500 μm long waveguide. The top graph shows the fundamental even mode.

is that the bandwidth of the setup does not allow one to measure in the linear-regime of the PhCW, thus no reference plateau having a 'normal' group-index is available. In this way, the vertical shift is here solely based on the FDTD calculated values. However, the FDTD nicely predicts the measured flat group index around 16-18 in a ∼15 nm bandwidth with a small curvature toward the transmission cutoffs. The experiment reveals that the mode has a constant group index of ∼15, a factor of 3 higher than in conventional waveguides, in a 9 nm bandwidth from 1542 nm - 1551 nm overlapping with the linear part of the mode plotted on top in the figure.

From fig. 6.24 the propagation loss can be found to 8.9 ± 2.8 dB/mm in this constant-group index region. It may be expected that the low-loss region 1533 nm - 1540 nm from fig. 6.24 would overlap with the constant (and lower) group index region. This is, however, not the case and is likely caused by a higher coupling between the even and the odd mode as they approach each other at longer wavelengths (see fig. 6.23(left)). It is believed that the propagation loss can be decreased and the group index increased by avoiding the degeneracy of the perturbated PhCW.

For comparison and used for approving the set of measurements, fig. 6.28 shows the measured group index (red) for a 10 μm W1 PhCW with similar parameters of the PhC as the perturbated PhCW. The transmission spectrum (black) reveal that the cutoff wavelength is located around 1541.5 nm. The group index has been shifted in the vertical direction so that the group index at 1528 nm far away from the cutoff wavelength in the linear-regime is 5. As was the case for the W1 waveguide shown in fig. 6.21 the group index increases dramatically when approaching the cutoff wavelength of the PhCW reaching values above 400. It is seen that the long-period (∼1.5 nm) ripples in the measured group index corresponds to the ripples in the transmission spectrum and, thus, stems from Fabry-Perot cavities in the waveguide system.

Figure 6.29(left) and (right) show the 3D band diagram and the measured transmission spectra for a second set of perturbated waveguides. These have perturbated first and second row of holes matching that of fig. 3.9 in section 3.2.7, i.e. the diameter of the first/second row has been changed -40/+25 nm. Again, the mode for the W1 PhCW is also plotted (orange) in the band diagram and used to shift the bands $\sim 0.5\%$ in frequency to match the calculated and measured mode-cutoffs. Comparing the transmission spectra of the 500 μm (red) and 1000 μm (green) to the band diagram it is seen that the transmission window of the waveguides match the even mode below the silica-line. Figure 6.30 shows the measured propagation loss of 4.8 ± 1.3 dB/mm in the wavelength range 1558 nm - 1562 nm for this waveguide system. Presently, the group index has not been measured for these waveguides as the mode profile for the fabricated waveguide is far from optimal as shown in fig. 3.9.

Conclusively, it is indeed possible to affect the dispersion properties of the fundamental mode in the PhCW and obtain low-loss ~ 10 nm-bandwidths below the silica-line with relatively high and constant group index. This is obtained by

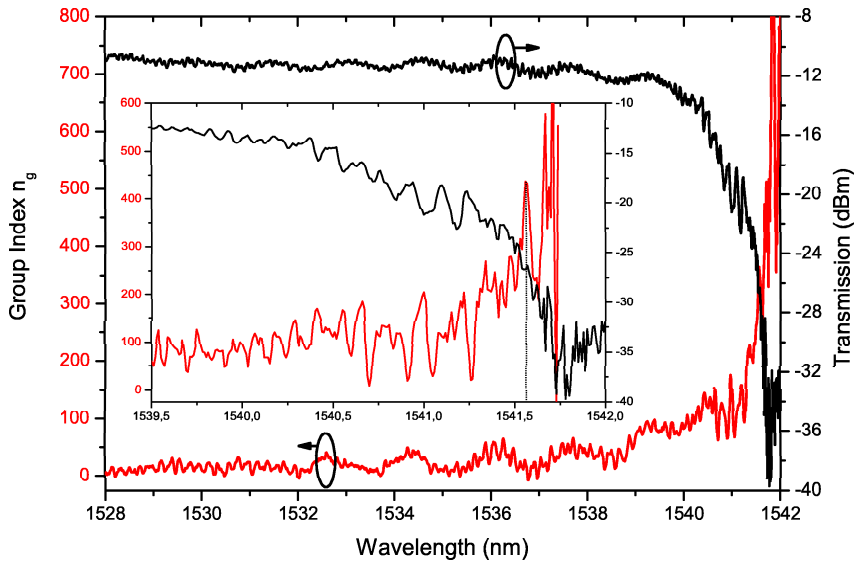

Figure 6.28: The measured group index (red) for a 10 μm W1 PhCW has been shifted so that the group index at 1528 nm is 5. The transmission spectrum (black) show that the cutoff wavelength is around 1541.5 nm.

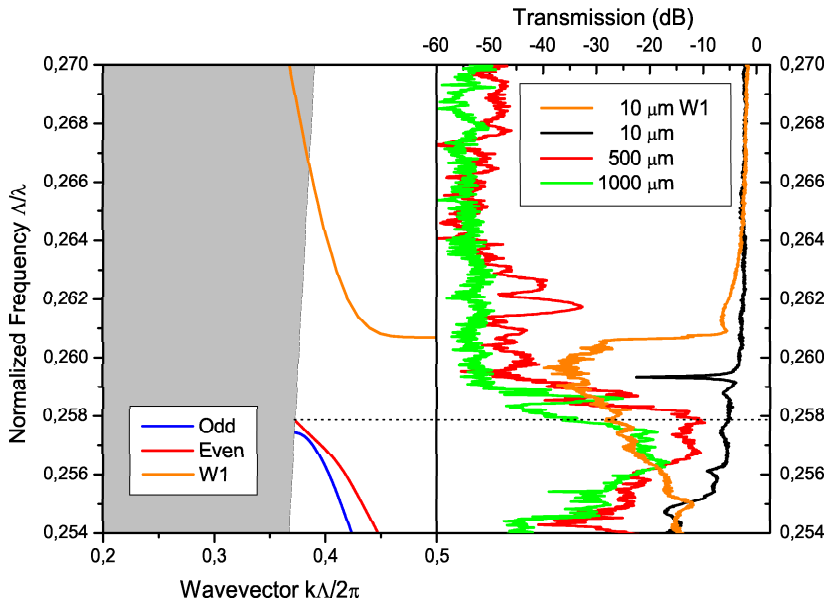

Figure 6.29: [Left] 3D band diagram for the PhCW with diameters -40/+25 nm of the first/second row of holes. [Right] Measured transmission spectra for a 10 μm (black), 500 μm (red), and 1000 μm long PhCW with perturbated first and second row of holes. For comparison the transmission for a 10 μm W1 PhCW is also plotted (orange).

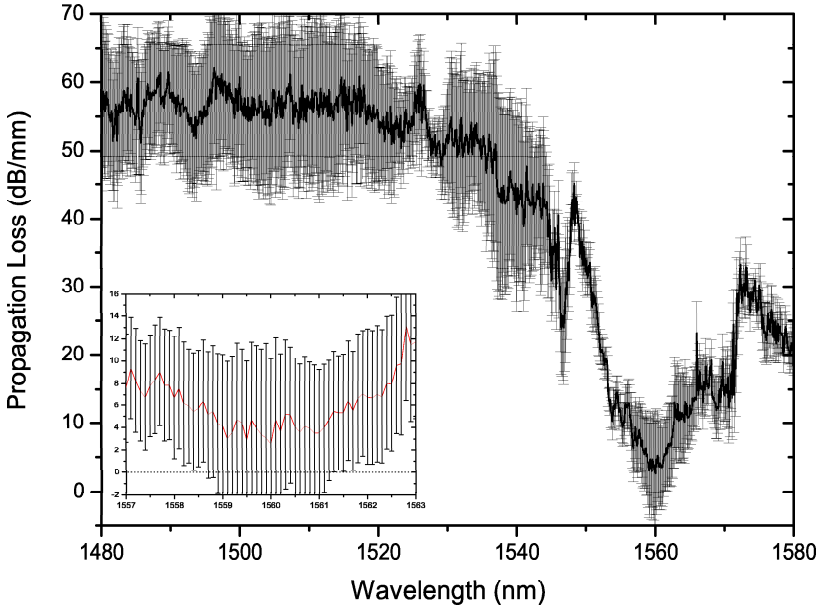

Figure 6.30: Measured propagation loss for the perturbated waveguides with the first row of holes decreased 40 nm and the second row of holes increased by 25 nm. Inset shows a zoom-in on the region 1557 nm - 1563 nm. The average loss is found to 4.8 ± 1.3 dB/mm in the range from 1558 nm - 1562 nm.

changing the diameter of the first and second row of holes. For further investigations, the pitch and PhC hole diameter should be changed (of the *fabricated* waveguide) to move the guided mode away from the slab-bands and avoid degeneracy of the PBG mode. Improvements of the design method may include also changing the core width of the PhCW (see sec. 3.2.5).

6.6.2 Coupling of Slow-Light to the PhCW

Having demonstrated the presence and utilization of slow-light in the PhCW we turn to the coupling efficiency for slow-light to a PhCW from a photonic wire, which is typically used for routing light across a chip. The large impedance mismatch between such prevents efficient coupling and depends on localized surface states and the exact termination of the photonic crystal lattice at the coupling interface [56–60]. Previous optimizations of the coupling efficiency have relied on the Edisonian approach where the interface termination has been shifted and/or altered based on human intuition [56, 57].

We apply the topology optimization scheme to optimize the coupling efficiency from a PhW to a PhCW for light in the slow-light regime of the PhCW. The goal-criterium is to optimize for high transmission through the PhCW for light excited in a butt-coupled PhW and having a wavelength close to the cutoff wavelength of the PhCW. Three different terminations of the PhW/PhCW interface have been investigated as shown in fig. 6.31(bottom): the interface being (a) in the middle of first column of holes and the interface shifted $\Lambda/7$ to the (b) right and (c) left. The design area is sketched (dotted yellow) in fig. 6.31(b). The optimizations have been performed by student Yang Lirong and the resulting and fabricated designs are shown in fig. 6.31(top). The transmission spectra for PhCWs having input- and output- regions as given in figs. 6.31(a-c) are shown in fig. 6.32 (red). Indeed, the termination of the generic interface has an impact on the coupling efficiency as the absolute transmission level differ $\sim$4 dB between the generic terminations at the cutoff wavelength. Thus, the termination of the PhCW should be accounted for in a device utilizing slow-light. In general, it is seen that the transmission through the PhCW for slow-light is higher for the topology-optimized interfaces (black) compared to waveguides having the reference generic interfaces (red). The largest enhancement of $\sim$5 dB is achieved for the termination shown in fig. 6.32(b). The topology-optimized structures seem to have converged to give essentially the same transmission performance near the cutoff independently of the initial un-optimized starting point. The converged transmission level for the topology optimized designs enhances the coupling $\sim$ 1.5 dB compared to the best of three reference configurations used here. Though not a dramatic increase, topology optimized interfaces may be convenient to use in order to secure a high coupling efficiency between a PhW and a PhCW for light in the slow-light regime of the PhCW.

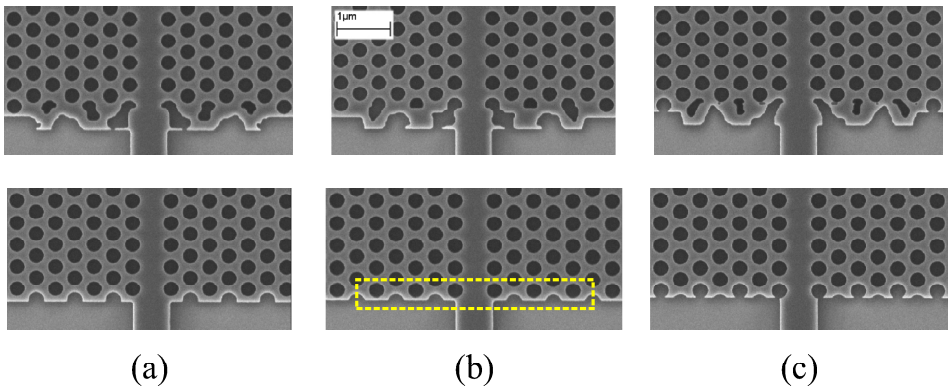

Figure 6.31: SEM images of the (top) topology-optimized and (bottom) reference couplings with the interface between the ridge waveguide and the photonic crystal waveguide intersecting the center of the first column holes (a) on the spot (b) right-shifted $\Lambda/7$ and (c) left-shifted $\Lambda/7$. The design area in the optimization is sketched in (b) (dashed yellow). Published in ref. [139].

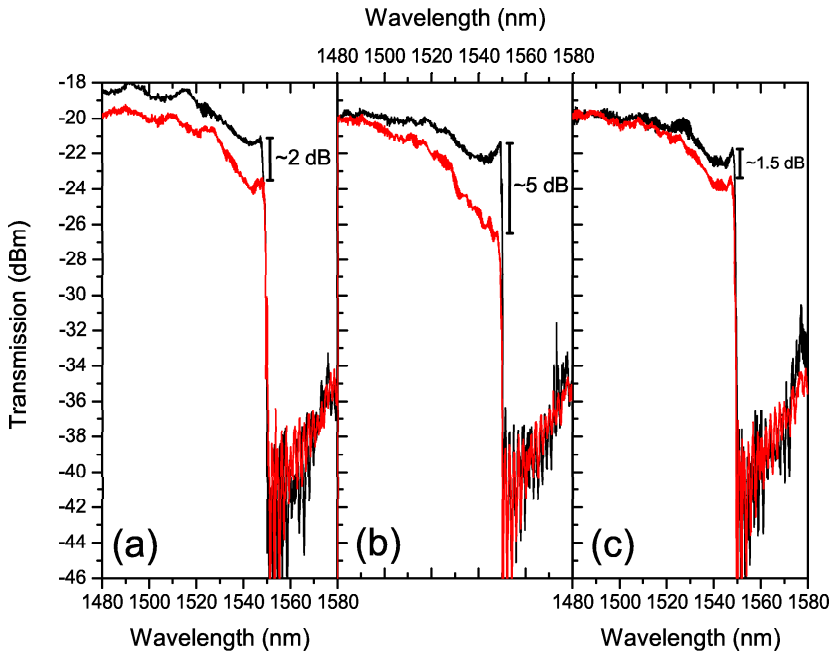

Figure 6.32: Transmission spectra of the topology-optimized (black) and reference (red) waveguide couplings for (a),(b), and (c) in fig. 6.31.

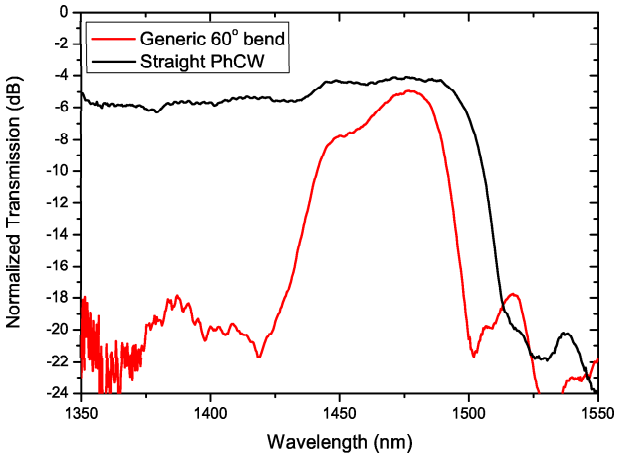

Figure 6.33: Normalized transmission spectra for a straight PhCW (black) and a PhCW with two consecutive generic 60^0 bends (red).

6.6.3 Bends for Slow-Light

Bending slow-light in a PhCW around corners is not a trivial task. Figure 6.33 shows the measured and normalized transmission spectra for a straight PhCW (black) and a PhCW having two consecutive generic (as shown in fig. 6.9(top-left)) 60^0 bends (red). As seen, the transmission window of the bends does not overlap with the slow-light regime of the PhCW near the cutoff wavelength, i.e. one can expect slow-light to be scattered and lost in the bends. Thus, special care needs to be taken when incorporating bends in a PhCW utilizing slow-light.

In a conventional curved ridge waveguide, the mode is pulled away from the center of curvature toward the outer edge of the bend, thus seeing a lower average refractive index with respect to the mode in the straight waveguide [20, 140]. Extending this picture to PhCWs, slow-light in bends will be blue-shifted and lost. This corresponds perfectly with the behavior shown in fig. 6.33. Previously, optimizations of bends for slow-light transmission have compensated for the decrease in effective index of the mode by increasing the index of the wave-guide bend. This is typically done by reducing the diameter of the borderholes selectively in the bend region [141, 142]. This is in analogy to what is done when increasing the width of a conventional ridge waveguide in a bend. However, the blue-shift compensation in PhCWs is obtained at the cost of transmission bandwidth as the mode distribution in the PhCW is more complex and should be taken into account

in the optimization. Therefore, it is not sufficient only to change the effective index locally in the first row of holes but it is also needed to include the second, or even the third, row of holes in the optimization to obtain a bend having broadband transmission and applicable for slow-light.

Figure 6.34(a) shows a SEM image of a waveguide with $D/\Lambda = 0.71$ having two of the 60^0 bends optimized for slow-light transmission as presented by Assefa et al. in ref. [142]. In this design, the diameter D_1 of first row of holes have been reduced to $D_1/\Lambda = 0.53$. A naive design done by Andrei Lavrinenko [23] based on the idea in ref. [142] *and* taking into account also the second row of holes is shown in fig. 6.34(b). Here, five holes in the second row of the bend have been replaced with smaller holes of diameter D_1 to reduce the effective index. Moreover, one hole on the inner side of the bend has been removed. Resulting designs from topology optimizations for broadband and slow-light transmission are shown in figs. 6.34(c) and (d), where (c) both rows and (d) only the second row of holes have been included in the design area. The topology optimization has been done by ph.d. student Amélie Têtu.

The measured and normalized transmission spectra for the waveguides are shown in fig. 6.35. As seen, the generic bend (black) cuts off transmission ∼20 nm before the cutoff wavelength for a corresponding PhCW (dotted line). Clearly, the naive design (red) from fig. 6.34(b) performs better in a broadband range compared to the bend presented in ref. [142] (orange) but cuts off transmission earlier in the slow-light regime. Both of the topology-optimized bends (blue and green) support transmission closer to the cutoff wavelength of the PhCW than does the bend from ref. [142]. Moreover, both topology-optimized bends have a wide transmission range stretching far into the linear-regime of the waveguide. This may be important for devices utilizing slow-light *and* light with conventional dispersion. Best performance is achieved by including both rows of holes in the topology optimization (blue) as this bend support transmission close to the cutoff wavelength and extends into the linear-regime. Again, one can speculate about the behavior of the complex topology-optimized design, which surely does not take into account only the effective index in the bend region, but also the mode distribution. For this configuration, the loss per bend is measured to 0.78 ± 0.48 dB in the wavelength range from 1520-1565 nm, which is twice as broad as the bend described in [142]. However, bending of slow-light call for further improvements and experiments e.g. including group index measurements to quantify the loss of slow-light in the bends.

6.7 Liquid Crystals in PhCWs

To end the chapter, I will shortly present some preliminary work done in collaboration with ph.d. Thomas Tanggaard Alkeskjold at COM•DTU on liquid crystals in a PhCW. The work has not been a part of my ph.d. project-description and was initiated in curiosity and inspired by previous work presented in refs. [144–146].

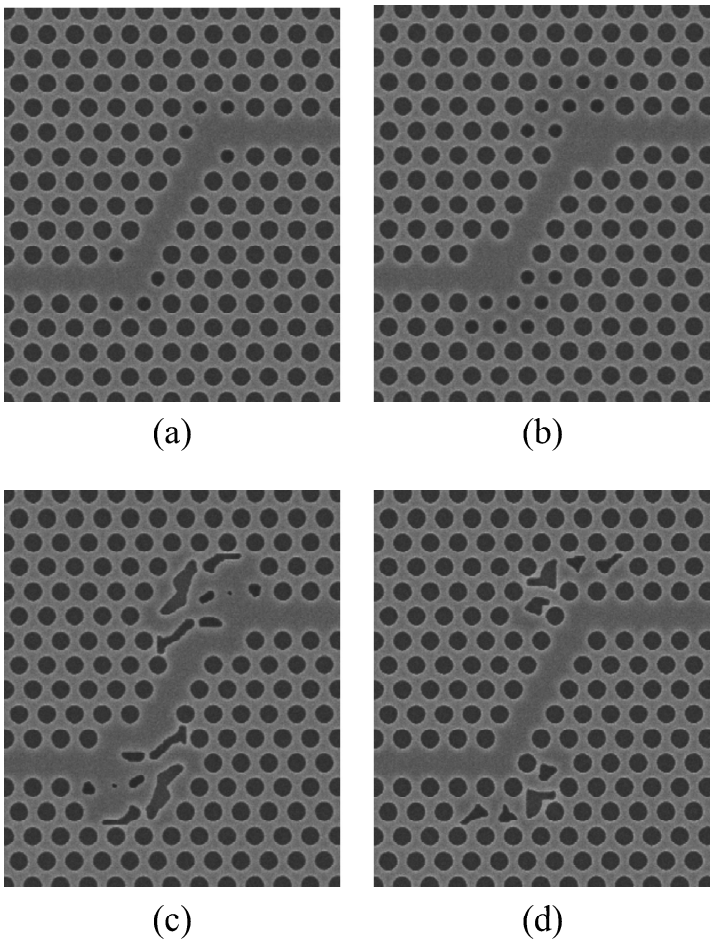

Figure 6.34: SEM image of PhCWs with $D/\Lambda = 0.71$ with two consecutive 60^o bends. (a) Taken from [142]. (b) Naive optimization. Topology-optimized bends with design areas including (c) two rows of holes and (d) only the second row of holes.

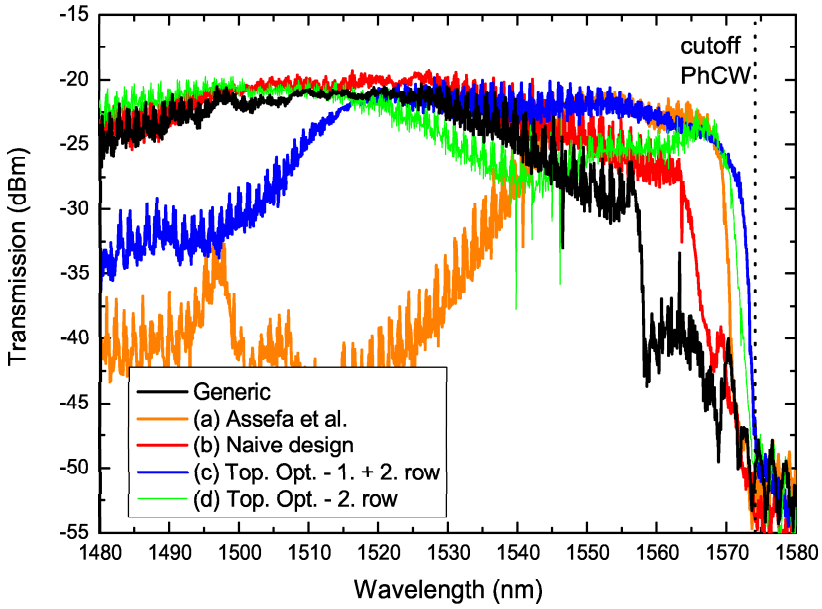

Figure 6.35: Normalized transmission spectra for the waveguides having two consecutive 60^0 bends corresponding to those shown in fig. 6.34. Dotted line marks the cutoff wavelength of a corresponding straight W1 PhCW. Published in ref. [143].

Liquid crystals (LCs) are organic materials consisting of molecules, which are geometrically anisotropic and possesses long-range orientational order [147, 148]. The long-range orientational order gives rise to a variety of meso-phases dependent on the orientation of the molecules and have physical properties intermediate between those of pure liquids and those of pure solids. A *thermotropic* LC undergoes a transition between meso-phases when the temperature is changed and is the most widely used in e.g. all sorts of flat-panel displays. The effective refractive index of the LC is linked to the molecular polarizability of the LC and, thus, the temperature, and can vary from ∼1.5 to ∼1.7 going from a temperature of 15^0C to 55^0C. The phase transitions may also be triggered by an applied electrical field with switching voltages around 1-10 $\frac{V}{\mu m}$ and is mostly used in commercial applications.

The basic idea is to infiltrate the holes of a planar PhC structure with a LC so that the effective index of the PhC can be changed by changing the temperature and/or applying an electrical field across the structure. Figure 6.36(a) shows a 2D FDTD calculation of the transmission through a PhCW having holes with an effective index of 1.5 (black) and 1.7 (red). As seen the cutoff wavelength red-shifts ∼15 nm when the index of the holes is increased 0.2. Thus, a signal at a wavelength near the cutoff of a heated waveguide ($n_{eff.} = 1.7$) could be switched on and off by cooling and heating the waveguide[12] and, thus, operate as an optical modulator. In a real device, however, the thermo-optic effect might be too slow and an electrical triggering of the LC would be preferred.

Experiments were done on a 10 μm long PhCW, which was cleaned in acetone, methanol, and isopropanol, and subsequently infiltrated with the LC MDA-00-1444, which is a well-tested thermo- and electro-optic LC with a refractive index $n_{25} \approx 1.5$ at room temperature. The infiltration was performed at atmospheric pressure at an elevated temperature to change the viscosity of the LC. Figure 6.36(b) show the measured transmission spectra of the PhCW before (black) and after (red) infiltration with the LC. Clearly, the PhC changes its effective index and the PhCW its properties when infiltrated with LC as the cutoff wavelength red-shifts ∼40 nm. It does not seem to introduce any severe excess loss to the waveguide as the transmission level is unchanged. The thermal properties of the infiltrated PhCW was tested by placing the sample on a hotplate and measuring the transmission through the waveguide at room temperature and at an elevated temperature. Figure 6.36(c) shows the measured spectra at 25^0C and 45^0C. As seen, the cutoff wavelength did not red-shift as hoped. The ripples in the spectrum taken at 45^0C are due to vibrations introduced by the hotplate. Thus, we did not see any effect of any phase transition, i.e. an index change of the PhC.

One reason for this could be that the LC did not find any long range order in the holes of the PhC as the quality of the PhC shown in fig. 6.36(d) was very poor[13]. Moreover, the hotplate could only heat up to 45^oC, which could be too

[12] A slow response time, yes, but to keep things simple we did not study the dynamics of the system and investigated only the thermo-optic effect.

[13] At that time we did not have many available samples that could be 'sacrificed' for an exper-

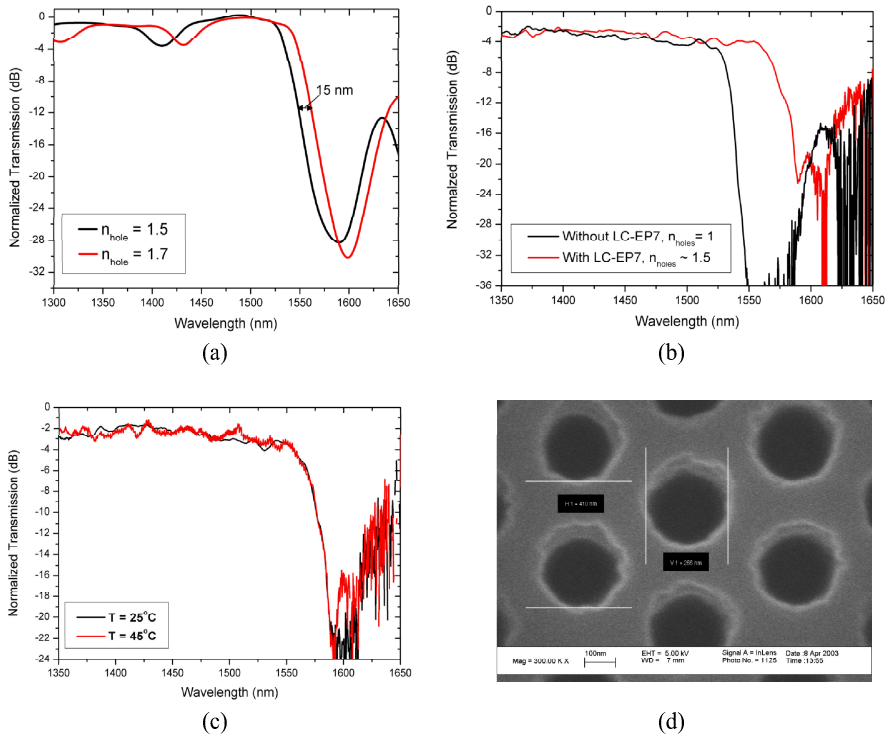

Figure 6.36: (a) 2D FDTD calculated transmission spectra for a PhCW having holes with an effective refractive index of 1.5 (black) and 1.7 (red). (b) Measured transmission spectra for a PhCW before (black) and after (red) infiltrated with the liquid crystal. (c) Measured transmission spectra for a PhCW infiltrated with a liquid crystal at a temperature at 25^0C (black) and 45^0C (red). (d) SEM of the PhC having rough holes before infiltration.

low in order for a phase transition to occur. Thus, the experiment calls for further and more detailed studies of LCs in PhCWs.

iment like this.

6.8 Summary

During the three-year project a wide range of different passive photonic crystal components have been fabricated utilizing nano-imprint, electron-beam, and deep-ultra violet lithography. The chapter has also presented SNOM images of the photonic crystal waveguide and Y-splitter that has been obtained in collaboration with partners within the PIPE project. These images showed a clear mapping of the photonic bandgap effect in the photonic crystal waveguide and evidence of severe scattering junctions in the Y-splitter and at interfaces between ridge waveguides and the photonic crystal waveguide.

In general, topology-optimized components showed noteworthy bandwidths with low excess losses. Also demonstrated was the ability to incorporate wavelength filtering into photonic crystal components either by shifting the cutoff wavelength along the waveguide or by applying the topology optimization scheme to T- and Y-splitters. However, the robustness of topology optimization may be improved to comply to the achievable resolution of fine-details in the fabrication. Finally, the presence of slow-light in the photonic crystal waveguide was proven experimentally measuring the group index for at W1 photonic crystal waveguide around 400. It was also demonstrated that it is possible to realize silicon-on-insulator waveguides with low-losses in small $\sim$10 nm bandwidths having a group index around 15.

The table on the next page summarizes the main results from the optical characterization of the waveguide components presented in this chapter. It should be noted that the wavelength regions wherein a given figure has been obtained can be scaled to a different region by an appropriate choice of parameters of the photonic crystal.

	Type	Figures	Bandwidth (nm)	Comments
Propagation Loss				
	W1 SOI	175 dB/mm	-	Above the silica-line.
	Perturbated #1	4.2 ± 1.4 dB/mm	7	With high group index ~20.
	Perturbated #2	4.8 ± 1.3 dB/mm	4	
Group Index				
	W1 SOI	400	-	
	Perturbated #1	16	7	May be incresed by avoiding degeneracy.
	Perturbated #2	-	-	
Slow-light Coupling				
	Top.-Opt.	5 dB	-	Best enhancement achieved.
Bend loss				
	60			
	Generic	0.6 ± 0.2 dB	20	
	Edisonian #1	0.6 ± 0.2 dB	40	Has an additional 15 nm low-loss bandwidth.
	Edisonian #2	1.12 ± 0.09 dB	40	
	Top.-Opt.	0.43 ± 0.27 dB	200	
	Top.-Opt. for slow-light	0.78 ± 0.48 dB	45	Overlapping with cutoff wavelength.
	90			
	Generic	> 5 dB	-	
	Top.-Opt.	0.78 ± 0.19 dB	200	
	120			
	Generic	> 10 dB	-	
	Top.-Opt.	~1 dB	200	
Splitting loss				
	PhC			
	Y Edisonian #1	0.26 ± 0.06 dB	25	Average excess loss of the 2 arms.
	Y Top.-Opt.	0.44 ± 0.29 dB	100	Average excess loss of the 2 arms.
	1x4 Top.-Opt.	1.54 ± 0.55 dB	100	Average excess loss of the 4 arms.
	PhW			
	T Top.-Opt.	0.87 ± 0.28 dB	>100	Average excess loss of the 2 arms.
De-multiplexing				
	PhC			
	EBL Lambda	5/15 dB	350	Worst/best extinction ratio.
	NIL Lambda	3/15 dB	200	Worst/best extinction ratio.
	CDWM	40, 20, 30 nm	-	Channel spacing.
	PhW			
	EBL Lambda	3/13 dB	350	Worst/best extinction ratio.

Figure 6.37: Main results obtained during the project.

Chapter 7

Conclusion

Within the last few years the world has seen a 'nano' revolution, which has been driven by mankind's ability to control materials on the nanometer scale. Within photonics, nanotechnology have developed 'bulky' integrated optical circuits into sophisticated and multi-functional photonic elements. Specifically, the recent advances within *silicon* photonics have thrived researchers to 'siliconize' photonics. This thesis have dealt with the designing, modelling, fabrication, and characterization of planar photonic crystal waveguide components defined by a triangular arrangement of holes in the silicon layer of a silicon-on-insulator slab. Such components may make nanophotonic circuits feasible in many applications.

The modelling part of the thesis applied the plane-wave expansion method and the finite-difference time-domain scheme to present and demonstrate a few of the numerous ways to affect and characterize the dispersion and guiding properties of the photonic crystal waveguide. One of the most promising features of such, the slow-light phenomenon, was presented and discussed. Specifically, for a waveguide defined by a single line-defect it was shown that a group index around 65 (a group velocity equal to $0.015c$) can be obtained in a $\sim$5 nm bandwidth by applying appropriate changes in the diameters of the first and second row of holes. In a typical wavelength division multiplexing system with 100 GHz channel spacings such waveguide could support 5 channels utilizing e.g. non-linear effects. A nice correlation between 2D/3D band diagrams and calculated 2D/3D transmission spectra for photonic crystal waveguides have been presented and it was shown that the characteristics of real fabricated waveguides can be predicted by finite-difference time-domain simulations. Ending the modelling part, the Time-Of-Flight method was presented and it was shown how the group index as a function of wavelength for the photonic crystal waveguide can be obtained by reading out the time-delays for the propagation of narrow-width pulses centered around different wavelengths.

Optimizing the performance of photonic crystal waveguide components may

be a non-trivial task. Two approaches of doing so were presented in the thesis. One is based on iterative attempts combined with human intuition to shift and/or enlarge selected photonic crystal elements. Though, this Edisonian method can be used with success it has proven to be non-optimal and resource-consuming. In the thesis, it was demonstrated how the inverse design strategy called topology optimization can be applied for the optimization of photonic crystal components. The method proved its strength within nanophotonics for optimizing the broadband performance of various photonic crystal components including bends, splitters, and coarse wavelength filters.

The optical performance of photonic crystal components is highly sensitive to the nanometer feature sizes of the components and even small deviations may be devastating for the functionality and/or the target operating frequency. Main parts of the project have dealt with the fabrication of photonic crystal structures in the DANCHIP cleanroom utilizing electron-beam lithography and inductively coupled reactive ions etching. Proximity correction in the electron-beam process was found to be of major importance for non-uniform pattern densities, e.g. when having closely-spaced waveguides of different lengths. Having found the appropriate clearance dose of 200 $\frac{\mu C}{cm^2}$, the critical issues in the electron-beam process is the spot-size of the beam (beam current) in respect to the feature-size and the dwell-time of the beam. When applying proximity correction a current of 0.2 nA (resulting in a spot-size around 4 nm) should be used. Higher currents may lead to errors in the written design as the small-area deflector is being pushed in speed to its limit. The thesis also presented the successful utilization of nanoimprint lithography for the fabrication of photonic crystal structures that open for the mass-fabrication of such, though care needs to be taken in the design. Conventional reactive ion etching available at DANCHIP was found to be unsuitable for the etching of photonic crystal structures as the anisotropy provided by the system is too low due to the rather high chamber pressure needed to have a stable etching plasma. On the contrary, if the etching plasma is generated away from the chamber to keep the chamber pressure low, a highly anisotropic etch can be obtained. The inductively coupled plasma reactive ion etching utilizing a Bosch process was proved to transfer nano-structured features from the resist to the silicon with high fidelities and steep side-wall profiles. Details on the fabrication and the etching recipe are given in Appendices C and D.

The thesis has presented numerous of experimental results obtained from fabricated photonic crystal components. The propagation loss of the photonic crystal waveguide realized in the silicon-on-insulator material was measured to be in the range of 175 dB/mm above the silica-line. No footprints of the expected narrow leakage-free bandwidth below the silica-line was seen. Thus, for normal low-loss photonic crystal waveguides to be realized the membrane configuration is found to be superior. Low excess losses below 1 dB in record-breaking bandwidths for the topology-optimized 60^0, 90^0, and 120^0 photonic crystal waveguide bends and

the topology-optimized Y-splitter have been realized. Also the T-splitter realized in the photonic wire proves to have excess losses below 1 dB. Moreover, the topology optimization scheme shows to be applicable for designing components with wavelength dependent behavior. However, the robustness of the method needs to be improved for narrow-bandwidth functionalities and to comply to fabrication tolerances. The loss figures for these simple components demonstrates the applicability of photonic bandgap components in nanophotonic circuits. Topology optimization also proved to be successful in the optimization of the coupling efficiency for slow-light from a photonic wire to a phototonic crystal waveguide as well as the transmission of slow-light through a 60^0 waveguide bend. A simple scheme for realizing a 4-channel coarse wavelength division multiplexing device by perturbating the borderholes was presented and the concept was demonstrated experimentally. Perturbation of the borderholes *and* the second row of holes in a photonic crystal waveguide was also shown to be a strong tool for tailoring the dispersion properties of the waveguide. In this way, a low-loss waveguide with a constant group index around 15 in a $\sim$9 nm bandwidth was obtained. In this region the propagation loss was found to be 8.9 ± 2.8 dB/mm. Outside this high-and-constant group index region the propagation loss was found to be 4.2 ± 1.4 dB/mm in a 7 nm bandwidth having a slightly higher but non-constant group index. These loss figures and values of the group index are believed to be improved by avoiding degeneracy of the mode. For a normal W1 photonic crystal waveguide the group index was measured to go beyond 400 in a very narrow bandwidth. Thus, for slow-light applications the photonic crystal platform seems very promising.

Epilogue

The basic photonic crystal structures presented in this thesis reflect the vision in the start of the project to utilize photonic crystal waveguides for routing light on and across an optical chip. Despite the experimental realizations of excess losses below 1 dB in broad wavelength ranges for various bends and splitters, the practical use of photonic crystal waveguides for such simple task is arguable as index-guided photonic wires offer a more feasible solution. However, the exotic dispersion properties of modes in a photonic crystal defect *do* offer new and novel ways of realizing sophisticated nanophotonic components utilizing slow-light phenomena and high-Q values applicable in modulator-, sensor-, switching-, and laser-applications. Disputable, research on the dynamic and *fast*-moving field of photonic crystals should go into *slow*-mode.

Lars Hagedorn Frandsen
Kgs. Lyngby, March 6, 2006

Appendix A

Band Diagrams with MPB

The manual for the MPB software [38] contains a nice tutorial and introduction to the band calculation of photonic crystals. As a quick start for future users, two important parameters need to be decided in order to obtain converged results: the resolution of the calculation grid and the size of the supercell, both of which are limited by the computer power available. Figure A.1 show the zoom-in on the fundamental even and odd PBG mode obtained in a 2D band calculation for the resolution of 8 (black), 16 (red), and 32 (green). As seen from the figure, the placement of the modes have converged using a resolution of 16, which is used for band diagrams shown in this thesis.

Another question in mind is the size of the supercell in order to obtain uncoupled modes. Figure A.2 show the movement of the bands when increasing the size of the supercell. As no surprise the slab modes are seen (left) to change dramatically when changing the supercell size. The fundamental mode plotted in the right graph seems to have converged in frequency for a supercell size of 11 which have been used for all diagrams shown in this thesis.

Figures A.3 and A.4 show typical control-files for the calculation of 2D and 3D band diagrams, respectively, for a W1 PhCW defined by a line-defect in a triangular lattice of air holes. The 3D calculation is setup for a SOI structure having a 320 nm thick silicon core placed on a 400 nm thick silica layer (as thick as the pitch) and with 400 nm of air above.

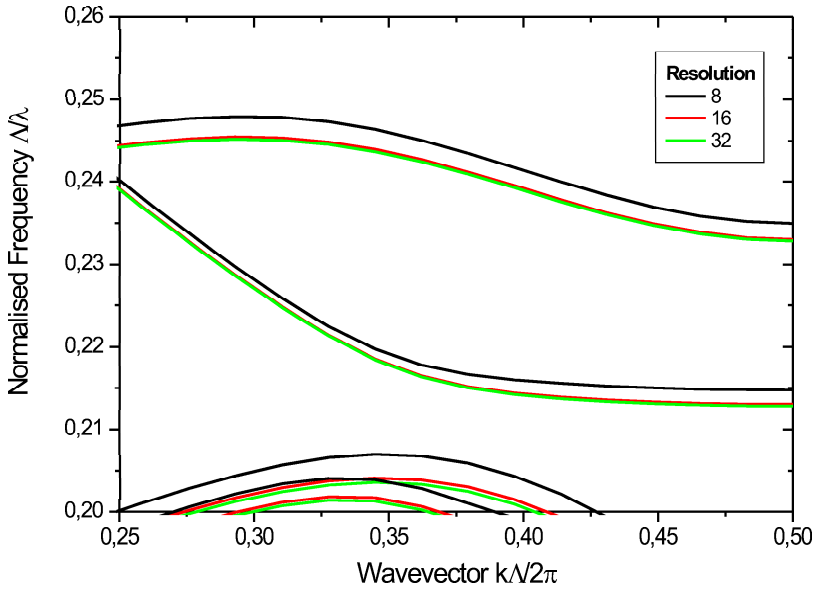

Figure A.1: Movement of the modes when changing the resolution of the calculation grid.

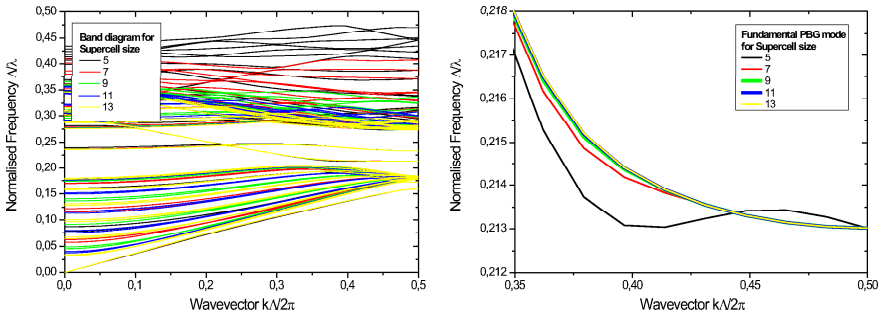

Figure A.2: Calculated 2D bands for different sizes of the supercell.

```
(define-param eps 12.0826) ; the dielectric constant of the slab
(define-param loweps 2.0851) ; dielectric constant of silica

(define-param r 0.35375) ; the radius 141.5 nm of the r holes for L=400nm

(define-param supercell-y 11) ; y-size of the supercell (odd number)

; triangular lattice with vertical supercell:

(set! geometry-lattice (make lattice (size 1 supercell-y no-size)
                         (basis1 (/ (sqrt 3) 2) 0.5)
                         (basis2 (/ (sqrt 3) 2) -0.5)))

(set! default-material (make dielectric (epsilon 1)))

(set! geometry
        (list
        (make block
                (material (make dielectric (epsilon eps)))
                  (center 0 0 0)
                        (size 1 11))

; the holes

        (make cylinder
                (material (make dielectric (epsilon 1)))
                  (center 0 1 0)
                        (radius r) (height infinity))
        (make cylinder
                (material (make dielectric (epsilon 1)))
                  (center 0 2 0)
                        (radius r) (height infinity))
        (make cylinder
                (material (make dielectric (epsilon 1)))
                  (center 0 3 0)
                        (radius r) (height infinity))
        (make cylinder
                (material (make dielectric (epsilon 1)))
                  (center 0 4 0)
                        (radius r) (height infinity))
        (make cylinder
                (material (make dielectric (epsilon 1)))
                  (center 0 5 0)
                        (radius r) (height infinity))

        (make cylinder
                (material (make dielectric (epsilon 1)))
                  (center 0 -1 0)
                        (radius r) (height infinity))
        (make cylinder
                (material (make dielectric (epsilon 1)))
                  (center 0 -2 0)
                        (radius r) (height infinity))
        (make cylinder
                (material (make dielectric (epsilon 1)))
                  (center 0 -3 0)
                        (radius r) (height infinity))
        (make cylinder
                (material (make dielectric (epsilon 1)))
                  (center 0 -4 0)
                        (radius r) (height infinity))
        (make cylinder
                (material (make dielectric (epsilon 1)))
                  (center 0 -5 0)
                        (radius r) (height infinity))))

; 1st Brillouin zone of a triangular lattice:
(define Gamma (lattice->reciprocal (vector3 0 0 0)))
(define K' (lattice->reciprocal (vector3 0.5 0 0)))


(set-param! resolution 16)
(set-param! num-bands 20)

(define-param only-K false) ; run with only-K=true to only do this k-point

(define-param k-interp 28)   ; the number of k points to interpolate

(if only-K
    (set! k-points (list K'))
    (set! k-points (interpolate k-interp (list Gamma K'))))


(run-te (output-at-kpoint K' fix-hfield-phase output-hfield-z))
(run-tm (output-at-kpoint K' fix-efield-phase output-efield-z))
```

Figure A.3: Control-file for 2D band diagram.

```
(define-param tcore 0.80) ; core thickness 320nm for L=400nm
(define-param tbuffer 1) ; buffer thickness 400 nm for L=400nm

(Define-param eps 12.0826) ; the dielectric constant of the slab
(define-param loweps 2.0851) ; dielectric constant of silica

(define-param r 0.35375) ; the radius 141.5 nm of the r holes for L=400nm

(define-param supercell-y 11) ; y-size of the supercell (odd number)

; triangular lattice with vertical supercell:

(set! geometry-lattice (make lattice (size 1 supercell-y 2.80)
                     (basis1 (/ (sqrt 3) 2) 0.5)
                     (basis2 (/ (sqrt 3) 2) -0.5)))

(set! default-material (make dielectric (epsilon 1)))

(set! geometry
        (list
        (make block
                (material (make dielectric (epsilon eps)))
                  (center 0 0 0)
                        (size 1 11 tcore))
        (make block
                (material (make dielectric (epsilon loweps)))
                  (center 0 0 -0.90)
                        (size 1 11 1))
; the holes
        (make cylinder
                (material (make dielectric (epsilon 1)))
                  (center 0 1 0)
                        (radius r) (height tcore))
        (make cylinder
                (material (make dielectric (epsilon 1)))
                  (center 0 2 0)
                        (radius r) (height tcore))
        (make cylinder
                (material (make dielectric (epsilon 1)))
                  (center 0 3 0)
                        (radius r) (height tcore))
        (make cylinder
                (material (make dielectric (epsilon 1)))
                  (center 0 4 0)
                        (radius r) (height tcore))
        (make cylinder
                (material (make dielectric (epsilon 1)))
                  (center 0 5 0)
                        (radius r) (height tcore))

        (make cylinder
                (material (make dielectric (epsilon 1)))
                  (center 0 -1 0)
                        (radius r) (height tcore))
        (make cylinder
                (material (make dielectric (epsilon 1)))
                  (center 0 -2 0)
                        (radius r) (height tcore))
        (make cylinder
                (material (make dielectric (epsilon 1)))
                  (center 0 -3 0)
                        (radius r) (height tcore))
        (make cylinder
                (material (make dielectric (epsilon 1)))
                  (center 0 -4 0)
                        (radius r) (height tcore))
        (make cylinder
                (material (make dielectric (epsilon 1)))
                  (center 0 -5 0)
                        (radius r) (height tcore))))

; 1st Brillouin zone of a triangular lattice:
(define Gamma (lattice->reciprocal (vector3 0 0 0)))
(define K' (lattice->reciprocal (vector3 0.5 0 0)))

(set-param! resolution 16)
(set-param! num-bands 20)

(define-param only-K false) ; run with only-K=true to only do this k-point

(define-param k-interp 28)   ; the number of k points to interpolate

(if only-K
    (set! k-points (list K'))
    (set! k-points (interpolate k-interp (list Gamma K'))))

(run-zeven (output-at-kpoint K' fix-hfield-phase output-hfield-z))
(run-zodd (output-at-kpoint K' fix-efield-phase output-efield-z))
```

Figure A.4: Control-file for 3D band diagram.

Appendix B

Transmission Spectra with CrystalWave

When calculating transmission spectra for PhC structures using CrystalWave there are certain issues to take care of. First of all, the waveguide structure needs to be put-up in a correct way! Figure B.1 shows a typical screendump of CrystalWave for a ∼20 μm long PhCW excited from a ridge waveguide and with the refractive index of silicon and silica to 3.476 and 1.444, respectively. The following points should be followed to obtain optimal results (more can be found in the manual of CrystalWave):

- Make sure all sides of the component is aligned to the device borders (use the *resize aligment tool*).
- If light is excited in a ridge waveguide, make sure that there is no gap between the ridge waveguide and the PhC (use the *resize aligment tool*).
- The excitor and the sensors should be aligned to each other in respect to the x-coordinate (place them by using coordinates).
- Sensors should be placed exactly aligned to the center of a hole.
- Avoid placing exciters and sensors close to interfaces.
- In 3D, having one-period-thick (here 400 nm) cladding layers have proven to give converged results.

Having put-up the structure appropriately, two important parameters need to be decided in order to obtain converged results: the grid-spacing and the number of time steps. Figure B.2 show the calculated transmission spectra using 2D FDTD and a grid-spacing of $\Lambda/32$ (solid lines) and $\Lambda/16$ (dotted line) for 16384 (black), 32768 (red), 131072 (blue), and 262144 number of time-steps. As seen, a converged

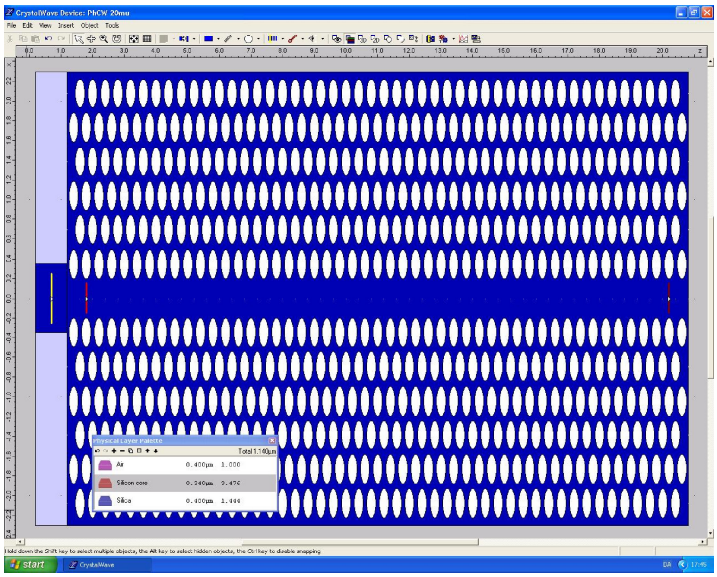

Figure B.1: Screendump from CrystalWave showing the setup for at ∼20 μm long PhCW.

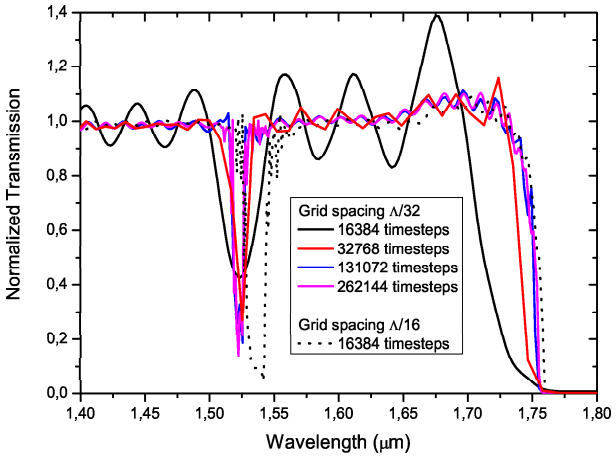

Figure B.2: Calculated transmission spectra for the waveguide.

result is not obtained having a grid-spacing $\Lambda/32$ and 16384 time-steps as the slow-light part of the mode has not reached the end of the waveguide. For this choice of resolution and length of the waveguide, 131072 number of time-steps is appropriate for having converged results, i.e. all frequency components have propagated through the waveguide. However, if the grid-spacing is chosen to $\Lambda/16$ 16384 number of time steps are okay, though having a rather broad virtual anti-crossing effect around 1.525 μm. The reason for this lies in the stability of CrystalWave that is automatically ensured by setting the time interval δt small enough to fulfill the *Courant stability criterion* [63]:

$$\delta t = 0.99\sqrt{\frac{3}{7}}\left(\frac{q_x}{c}\right) \tag{B.1}$$

where q_x is the grid-spacing in the x-direction and c is the speed of light. Thus, due to this correlation between the resolution and the size of each time step, the values for these should be chosen carefully in order to obtain converged results for the exact device to be modelled. Before doing heavy 3D calculations it is a good idea to test for convergence in 2D first!

Appendix C

Fabrication of Photonic Crystals @ DANCHIP

The appendix at hand is to be taken as a quick, short, and 'dirty' step-by-step guide to the fabrication of photonic crystal structures in silicon-on-insulator material at DANCHIP. It is assumed that the user has gotten the proper training in using the specific piece of equipment!

Preparing the GDSII design file

The design file should be prepared with the *L-Edit* layout editor from Tanner Eda[1] and saved as GDSII files. The software is fairly easy to use for people experienced with Windows and has a comprehensive manual on 1500 pages, which can be addressed through the Help menu. Following is a list of guide lines to the design phase:

- Grid size should be 1 nm and is set in *Setup/Design/Grid/Manufacturing Grid*.
- Different structures could be put in different layers in order to write micro-scale structures with a high current and nano-scale structures with a low current.
- Use *instances* as much as possible to decrease the size of the design file. The conversion to the e-beam file format may fail if the file is too large.
- Holes should preferably be represented by polygons with 12 vertices.
- Check whether imported structures (e.g. topology optimized structures) are polygons and NOT wires!

[1] http://www.tannereda.com

- To import topology optimized structures use e.g. the demo-version of the CAD program *Graffy*[2] to create GDSII files from B&W bitmap pictures.
- Scaled, mirrored, and rotated structures *are* compatible with the e-beam file format.
- The use of text in the layout could be a good idea, but takes time to write!

Wafer cleaning

Even though the wafers are taken from a new box they should be cleaned prior to spinning on the resist. The wafers are cleaned in a spin-cleaning process on the resist spinner (presently the III-V spinner in cleanroom 4). The procedure is as follows:

- Setup an *open*-spin program at ∼800 rpm and time-code 33 (program ends when enter is pressed).
- Put-on the appropriate chuck and make sure it can rotate freely without touching the plastic bin.
- Get bottles with acetone, methanol, and iso-propanol (IPA).
- Put the wafer to be cleaned on the chuck and start the program (the program will not start if the vacuum is not on).
- While spinning: blow the wafer for approximately 1 min. with N_2.
- With the wafer rotating; pour acetone, methanol, and IPA on the wafer in that order. Avoid acetone and methanol to dry out on the wafer. Blow-dry after IPA with nitrogen.

Resist spinning

Subsequently to the wafer cleaning the resist should be spun-on. The aim is to obtain a thickness of ∼100 nm 5.5% ZEP520A resist. The resist is diluted 1:1 with anisole and is normally stored in the fridge in serviceroom 3. Pour a few ml of diluted ZEP520A in one of the small (and clean!) plastic bottles found in cleanroom 3 (the one with a long tip). Preferably, rinse the bottle with IPA to remove any dust particles. Best results are obtained if you pour from the open bottle without the tip.

The spinner should be programmed as follows

- closed-spin
- speed: 500 rpm

[2] http://www.durst.de/produkte_graffybas.html

- acceleration: 100 rpm/s
- time: 5 seconds
- closed-spin
- speed: 6000 rpm
- acceleration: 2000 rpm/s
- time: 60 seconds
- 000

Turn on the hotplate next to the spinner and set the temperature to 160^0C. When the temperature has been reached the spinning process can be started. It is recommended to do a test-spin on a silicon wafer with similar parameters before doing a "real" spin on a SOI wafer to test ones spinning skills and the homogeneity of the resist. The test-wafer can be used to test the thickness of the resist and in later etch-tests.

1. Pour on an amount of diluted ZEP520A so that the full wafer/chip is covered.
2. Immediately after start the spinning program (avoid as little resist as possible to evaporate, i.e. be quick).
3. Take a step back and relax for the next 60 seconds.
4. When the spinning has stopped, place the wafer on the hotplate and pre-bake for 2 minutes.

After pre-baking, go measure the film thickness of the wafer at the FilmTek in cleanroom 2.

E-beam

The GDSII-file from L-Edit should be converted to the V30 file format of the e-beam. This is done at the e-beam in the cleanroom and Peixiong Shi can assist in doing that. However, the following lists the steps:

1. Transfer the design file with FTP from the central computer in the control room to the left computer (named DS10). Put it in /usr/users/eb0/ebtest/data/jeolsvc.
2. Open the JBXFILER-window on DS10. Get the file information by right-clicking the GDSII-file and select "Information".
3. Convert the GDSII-file to a JEOL .v30 work file and a .DAT-file by again right-clicking the file and select "conv". Paste the main structure name, the coordinates of the layout, and the layer number from the previous "Information" screendump and click OK.

4. Change the .v30 and the .DAT file names to whatever appropriate and put the field sizes to 500 μm. Change the output step (from 40) to 1000. If proximity correction is applied change the "Special conv." to "Shot Modulation 1". Rotate and mirror the design if necessary. Click OK.

5. When the conversion has finished (typically after ∼20-40 minutes) convert the .v30 file to a graphical .pchk file by right-clicking the file and select "convert to graphic data". Check the graphic file (.pchk) by right-clicking the file and select "Display graphic data". Press "Draw".

6. Transfer the layout to the right computer (XP1000) with FTP via the middle computer.

7. Now make the Job Description File (.jdf) and Structure Description File (.sdf). The sdf-file describes the position of and how many times a single design (a .v30 file) is to be written and on which carrier it is going to be written. Moreover, the sdf-file does also hold the dose and the e-beam step size. The sdf-file points to the jdf-file that determine *which* .v30 is to be written, the current it is to be written with (actually only used for estimating the writing time - Peixiong will adjust the e-beam to the needed current) and, optionally, the different doses associated with different datatypes, if proximity correction is applied.

8. Compile the sdf-file with the command: schd "sdf-file-name".

9. The writing time can be simulated by using the "wrtestui" command. Check also that the e-beam dwell time does not approach the 40 ns limit - this may, by experience, lead to e.g. small noses when writing holes.

During the conversion of the files, the wafer with resist can be cleaved into appropriate-sized pieces and mounted on the carrier.

Peixiong Shi will change/optimize the e-beam current and the chamber conditions.

Development and post-baking

After the e-beam lithographic step the samples are developed and post-baked as follows:

- Turn on the hotplate and set the temperature to 110^0C.
- Pour the developer ZED-N50 and IPA in each their small and flat beaker.
- Develop the sample 1 minute in ZED-N50.
- Rinse immediately thereafter for 15 seconds in IPA.
- Blow-dry the sample with nitrogen.

- Post-bake the sample 3 minutes at 110^0C.

After developing and post-baking the sample could be inspected in the SEM. HOWEVER, be careful not to zoom too much in on critical structures and use a low EHT voltage as you are dealing with a resist, which is sensitive to the scanning electron beam of the SEM!!!

Etching

As described elsewhere best results are obtained when using the STS ASE and the recipe in appendix D.

As the etch rate may fluctuate from day-to-day care should be taken to estimate the correct number of cycles for the recipe to run in order not to over-etch the sample. We use small test pieces of silicon with resist (preferably, pieces from the test-wafer in the resist spinning process) to determine the etch rate of silicon and that of the resist. The procedure is as follows:

1. Run the pre-conditioning recipe *SJHEAT* for ∼30 minutes.
2. Abrade the resist on 2-3 test pieces of silicon with the tweezer and go measure the depths of the scratches in the DEKTAK profiler to obtain the actual resist thickness.
3. Etch the test pieces one after another for a given number of cycles, say 9 cycles, using the recipe given in appendix D (pxnano1).
4. After the etches make new scratches on the samples and go measure the depth of these and of the first scratches made. Along with the known initial resist thickness, the depth of the new scratches gives the etch rate of the ZEP520A. The depths of the old scratches along with the depths of the new scratches give the etch rate of silicon. Check that the found etch rates are rather similar (stable etch rate).
5. If the found etch depths of silicon and ZEP520A are inappropriate change the number of cycles and test again the actual etch depth of silicon.
6. Optionally, run a short *SJHEAT* for ∼5 minutes to heat up the chamber again to secure a stable etch rate.
7. Etch the SOI sample with the found number of cycles. Usually, 9 cycles is found to etch through 340 nm of silicon and etch away ∼60 nm of ZEP520A.
8. Remove the remaining resist with the *02clean* process for ∼1 minute.

Cleaving

After etch and SEM inspection the sample can be taken out of the cleanroom (if no post-processing is to be done) to the cleaver in the optical lab.

Paper writing

The results hopefully speak for themselves.

Enjoy!

Appendix D

ICP Recipe

	Parameter	Setting				
Chiller	Temperature	10 °C				
General	Pump down	00:00:20				
	Gas stabilization	00:00:10				
	Process time	xx:xx:xx				
	Advanced	Parameter switching active				
	Start	Passivation				
	End	Etch				
	Cycles	xx				
	Parameter	Etch	5.0	0.0		
		Passivation	3.0	0.0		
	Recipe Process	Discreet				
Pressure	APC	Auto				
	Pressure	10 mTorr				
	Tolerance	50%				
	Base Pressure	0.1 mTorr				
	Pressure Trip	94.0 mTorr				
Gases			Etch		Passivation	
		Gas	Flow	Tol.	Flow	Tol.
		C4F8	50	25	50	25
		SF6	50	25	0	5
		O2	0	0	0	0
		Ar	0	0	0	0

RF	Coil	Power	Etch	500 W
			Passivation	400 W
			Tolerance	50%
			Matching	Auto
			Match load	36%
			Match tune	60%
	Platen	Power	Etch	30 W
			Passivation	0 W
			Tolerance	50%
			Matching	Auto
			Match load	45%
			Match tune	61%
	Range	0 - 30 W		
HBC	HBC Active	X		
	He Flow	Pressure		10 Torr
		Tolerance		50%
		Max. Flow		40 sccm
		Min. Flow		10 sccm
	Perform test	X		
	Test Time	0:00:30		
	Max Leak rate	60 mTorr/min		

Bibliography

[1] M. Lipson. Guiding, modulating, and emitting light on silicon–challenges and opportunities. *Lightwave Technology, Journal of*, 23(12):4222–4238, 2005.

[2] H. Rong, A. Liu, R. Jones, O. Cohen, D. Hak, R. Nicolaescu, A. Fang, and M. Paniccia. An all-silicon raman laser. *Nature*, 433(7023):292–4, 2004.

[3] Ansheng Liu Mario Paniccia Oded Cohen Haisheng Rong, Ying-Hao Kuo. High efficiency wavelength conversion of 10 gb/s data in silicon waveguides. *Optics Express*, 14(3):1182–1188, 2006.

[4] Ling Liao, Dean Samara-Rubio, Michael Morse, Ansheng Liu, Dexter Hodge, Doron Rubin, Ulrich D. Keil, and Thorkild Franck. High speed silicon mach-zehnder modulator. *Optics Express*, 13(8):3129–3135, 2005.

[5] Y. A. Vlasov and S. J. McNabb. Losses in single-mode silicon-on-insulator strip waveguides and bends. *Optics Express*, 12(8):1622–1631, 2004.

[6] L.R. Nunes, T.K. Liang, H.K. Tsang, M. Tsuchiya, D. Van Thourhout, P. Dumon, and R. Baets. Ultrafast non-inverting wavelength conversion by cross-absorption modulation in silicon wire waveguides. *Group IV Photonics, 2005. 2nd IEEE International Conference on*, pages 154–156, 2005.

[7] R. Jacobsen, K. Andersen, P.I. Borel, J. Fage-Pedersen, L.H. Frandsen, O. Hansen, M. Kristensen, A. Lavrinenko, G. Moulin, H. Ou, C. Peucheret, B. Zsigri, and A. Bjarklev. Strained silicon as a new electro-optic material. *Accepted for publication in Nature*, 2006.

[8] E. Yablonovitch. Inhibited spontaneous emission in solid-state physics and electronics. *Phys. Rev. Lett.*, 58(20):2059–2062, 1987.

[9] S. John. Strong localization of photons in certain disordered dielectric super lattices. *Phys. Rev. Lett.*, 58(23):2486–2489, 1987.

[10] M. Svalgaard, C.V. Poulsen, A. Bjarklev, and O. Poulsen. Direct uv writing of buried singlemode channel waveguides in ge-doped silica films. *Electronics Letters*, 30(17):1401–1403, 1994.

[11] D. Zauner, K. Kulstad, J. Rathje, and M. Svalgaard. Directly uv-written silica-on-silicon planar waveguides with low insertion loss. *Electronics Letters*, 34(16):1582–1584, 1998.

[12] M. Loncar, D. Nedeljkovic, T. Doll, J. Vuckovic, A. Scherer, and T.P. Pearsall. Waveguiding in planar photonic crystals. *Applied Physics Letters*, 77(13):1937–9, 2000.

[13] J. D. Jackson. *Classical Electrodynamics*. Wiley, New York, 1962.

[14] John D. Joannopoulos, Robert D. Meade, and Joshua N. Winn. *Photonic Crystals, Molding the flow of light*. Princeton University Press, 1995.

[15] Bent Elbek. *Elektromagnetisme*. Niels Bohr Instituttet, Copenhagen University, 1992.

[16] S. G. Johnson and J. D. Joannopoulos. Block-iterative frequency-domain methods for maxwell's equations in a planewave basis. *Opt. Exp.*, 8(3):173–190, 2001.

[17] R. D. Meade, A. M. Rappe, K. D. Brommer, J. D. Joannopoulos, and O. L. Alerhand. Accurate theoretical analysis of photonic band-gap materials. *Phys. Rev. B*, 48(11):8434–8437, 1993.

[18] S. G. Johnson and J. D. Joannopoulos. The MIT Photonic-Bands package home page.
http://ab-initio.mit.edu/mpb/.

[19] Allen Taflove. *Advances in Computational Electrodynamics, The Finite Difference Time Domain Method*. Artech House Publishers, 1998.

[20] Richard Syms; John Cozens. "Optical guided waves and devices". *Mcgraw-Hill Book Company*, 0-07-707425-4.

[21] Photon Design. Company home page.
http://www.photond.com.

[22] A.J. Ward and J.B. Pendry. A program for calculating photonic band structures, green's functions and transmission/reflection coefficients using a non-orthogonal fdtd method. *Computer Physics Communications*, 128(3):590–621, 2000.

[23] Andrei Lavrinenko. Department of Communications, Optics, and Materials, DTU, Private communication, ala@com.dtu.dk.

[24] A. Lavrinenko, P. I. Borel, L. H. Frandsen, M. Thorhauge, A. Harpøth, M. Kristensen, T. Niemi, and H. M. H. Chong. Comprehensive FDTD modelling of photonic crystal waveguide components. *Optics Express*, 12(2):234–248, 2004.

[25] Anders Harpøth. *Design and Fabrication of Photonic Crystal Materials and Components*. PhD thesis, Research Center COM, Technical University of Denmark, 2005.

[26] S. G. Johnson, S. Fan, P. R. Villeneuve, and J. D. Joannopoulos. Guided modes in photonic crystal slabs. *Phys. Rev. B*, 60(8):5751–5758, 1999.

[27] C. Jamois, R. B. Wehrspohn, L. C. Andreani, C. Hermann, O. Hess, and U. Gösele. Silicon-based two-dimensional photonic crystal waveguides. *Photonics and nanostructure, Fundamentals and Applications*, 1:1–13, 1003.

[28] M.A. Duguay, Y. Kokubun, T.L. Koch, and L. Pfeiffer. Antiresonant reflecting optical waveguides in sio_2-si multilayer structures. *Applied Physics Letters*, 49(1):13–15, 1986.

[29] A.V. Lavrinenko, L.H. Frandsen, J. Fage-Pedersen, and P.I. Borel. Photonic crystal waveguides based on an antiresonant reflecting platform. *Transparent Optical Networks, 2005, Proceedings of 2005 7th International Conference*, 1:273–276, 2005.

[30] Y.L. Yang and et al. Arrow-based photonic crystal waveguides for efficient coupling with fibers. *Proceedings of ECIO-2005*, pages 642–645, 2005.

[31] H. Takano, Y. Akahane, T. Asano, and S. Noda. In-plane-type channel drop filter in a two-dimensional photonic crystal slab. *App. Phys. Lett.*, 84(13):2226–2228, 2004.

[32] B-S. Song, S. Noda, and T. Asano. Photonic devices based on in-plane hetero photonic crystals. *Science*, 300:1537, 2003.

[33] H-Y. Ryo, M. Notomi, and Y-H. Lee. High-quality-factor and small-mode-volume hexapole modes in photonic-crystal-slab nanocavities. *Appl. Phys. Lett.*, 83(21):4294–4296, 2003.

[34] M. Notomi, A. Shinya, S. Mitsugi, E. Kuramochi, and H-Y. Ryu. Waveguides, resonators and their coupled elements in photonic crystal slabs. *Optics Express*, 12(8):1551–1561, 2004.

[35] S. Noda, A. Chutinan, and M. Imada. Trapping and emission of photons by a single defect in a photonic bandgap structure. *Nature*, 407:608–610, 2000.

[36] Hatice Altug and Jelena Vuckovic. Photonic crystal nanocavity array laser. *Optics Express*, 13(22):8819–8828, 2005.

[37] T. Asano T. Uesugi, B. Song and S. Noda. Investigation of optical nonlinearities in an ultra-high-q si nanocavity in a two-dimensional photonic crystal slab. *Optics Express*, 14:377–386, 2006.

[38] S. G. Johnson. The mit photonic-bands manual. *http://ab-initio.mit.edu/mpb/doc/*.

[39] T. Soendergaard, A. Bjarklev, J. Arentoft, M. Kristensen, J. Erland, J. Broeng, and S.E. Barkou Libori. Designing finite-height photonic crystal waveguides: confinement of light and dispersion relations. *Optics Communications*, 194(4-6):341–351, 2001.

[40] Wim Bogaerts. *Nanophotonic Waveguides and Photonic Crystals in Silicon-on-Insulator*. PhD thesis, Vakgroep Informatietechnologie (INTEC), Faculteit Toegepaste Wetenschappen, University Gent, 2004.

[41] C. Y. Kao, S. Osher, and E. Yablonovitch. Maximizing band gaps in two-dimensional photonic crystals by using level set methods. *Applied Physics B*, 81(2-3):235–244, 2005.

[42] H. Benisty, C. Weisbuch, D. Labilloy, M. Rattier, C.J.M. Smith, T.F. Krauss, R.M. de la Rue, R. Houdre, U. Oesterle, C. Jouanin, and D. Cassagne. Optical and confinement properties of two-dimensional photonic crystals. *Lightwave Technology, Journal of*, 17(11):2063 –2077, 1999.

[43] L. Wu, M. Mazilu, J.-F. Gallet, and T.F. Krauss. Square lattice photonic-crystal collimator. *Photonics and Nanostructures - Fundamentals and Applications*, 1(1):31–36, 2003.

[44] H. Kosaka, T. Kawashima, A. Tomita, M. Notomi, T. Tamamura, T. Sato, and S. Kawakami. Superprism phenomena in photonic crystals: toward microscale lightwave circuits. *Lightwave Technology, Journal of*, 17(11):2032 –2038, 1999.

[45] A. G. Kirk L. Wu T. F. Krauss R. M. De La Rue A. S. Jugessur, A. Bakhtazad. Compact and integrated 2-d photonic crystal super-prism filter-device for wavelength demultiplexing applications. *Optics Express*, 14(4):1632–1642, 2006.

[46] S. G. Johnson, P. R. Villeneuve, S. Fan, and J. D. Joannopoulos. Linear waveguides in photonic-crystal slabs. *Phys. Rev. B*, 62(12):8212–8222, 2000.

[47] P.I. Borel, L.H. Frandsen, A. Harøpth, J.B. Leon, H. Liu, M. Kristensen, W. Bogaerts, P. Dumon, R. Baets, V. Wiaux, J. Wouters, and S. Beckx. Bandwidth engineering of photonic crystal waveguide bends. *Electronics Letters*, 40(20):1263–4, 2004.

[48] M. Soljacic, S.G. Johnson, Shanhui Fan, M. Ibanescu, E. Ippen, and J.D. Joannopoulos. Photonic-crystal slow-light enhancement of nonlinear phase sensitivity. *Journal of the Optical Society of America B (Optical Physics)*, 19(9):2052–9, 2002.

[49] Marin Soljacic and J.D. Joannopoulos. Enhancement of nonlinear effects using photonic crystals. *Nature Materials*, 3(4):211–219, 2004.

[50] Shin-Ichiro Inoue and Yoshinobu Aoyagi. Design and fabrication of two-dimensional photonic crystals with predetermined nonlinear optical properties. *Physical Review Letters*, 94(10):1–4, 2005.

[51] N. Notomi, K. Yamada, A. Shinya, J. Takahashi, C. Takahashi, and I. Yokohama. Extremely large group-velocity dispersion of line-defects waveguides in photonic crystal slabs. *Phys. Rev. Lett*, 87(25), 2001.

[52] Mehmet Fatih Yanik, Wonjoo Suh, Zheng Wang, and Shanhui Fan. Stopping light in a waveguide with an all-optical analog of electromagnetically induced transparency. *Physical Review Letters*, 93(23):233903–1–233903–4, 2004.

[53] Yurii A. Vlasov, Martin O'Boyle, Hendrik F. Hamann, and Sharee J. McNab. Active control of slow light on a chip with photonic crystal waveguides. *Nature*, 438(7064):65–69, 2005.

[54] A.Y. Petrov and M. Eich. Efficient approximation to calculate time delay and dispersion in linearly chirped periodical microphotonic structures. *Quantum Electronics, IEEE Journal of*, 41(12):1502–1509, 2005.

[55] A.Yu. Petrov and M. Eich. Dispersion compensation with photonic crystal line-defect waveguides. *Selected Areas in Communications, IEEE Journal on*, 23(7):1396–1401, 2005.

[56] Y. A. Vlasov and S. J. McNab. Coupling into the slow light mode in slab-type photonic crystal waveguides. *Optics Letters*, 31:50–52, 2006.

[57] Eiji Miyai and Susumu Noda. Structural dependence of coupling between a two-dimensional photonic crystal waveguide and a wire waveguide. *Journal of the Optical Society of America B: Optical Physics*, 21(1):67–72, 2004.

[58] Jun Ushida, Masatoshi Tokushima, Masayuki Shirane, and Hirohito Yamada. Systematic design of antireflection coating for semi-infinite one-dimensional photonic crystals using bloch wave expansion. *Applied Physics Letters*, 82(1):7–9, 2003.

[59] R. Baets, P. Bienstman, P. Dumon, B. Luyssaert, J. Mart, and P. Sanchis. Analysis and design of efficient coupling in photonic crystal circuits. *Optical and Quantum Electronics*, 37(1-3):133–147, 2005.

[60] P. Kramper, M. Agio, C.M. Soukoulis, A. Birner, F. Muller, R.B. Wehrspohn, U. Gosele, and V. Sandoghdar. Highly directional emission from photonic crystal waveguides of subwavelength width. *Physical Review Letters*, 92(11):113903–1–113903–4, 2004.

[61] S. Hughes, L. Ramunno, Jeff F. Young, and J.E. Sipe. Extrinsic optical scattering loss in photonic crystal waveguides: Role of fabrication disorder and photon group velocity. *Physical Review Letters*, 94(3):1–4, 2005.

[62] S. Hughes, L. Ramunno, E. Kuramochi, T. Watanabe, A. Shinya, and M. Notomi. Disorder-induced optical scattering loss in planar photonic crystal waveguides: theory and experiment. *ARFTG Conference Digest, Spring 2002. 59th*, 1:467–469 Vol. 1, 2005.

[63] *Crystal wave*-manual.

[64] B. Cluzel, D. Gerard, E. Picard, T. Charvolin, V. Calvo, E. Hadji, and F. De Fornel. Experimental demonstration of bloch mode parity change in photonic crystal waveguide. *Applied Physics Letters*, 85(14):2682–2684, 2004.

[65] R.S. Jacobsen, A.V. Lavrinenko, L.H. Frandsen, C. Peucheret, B. Zsigri, G. Moulin, J. Fage-Pedersen, and P.I. Borel. Direct experimental and numerical determination of extremely high group indices in photonic crystal waveguides. *Optics Express*, 13(20):7861–7871, 2005.

[66] K. Inoue, N. Kawai, Y. Sugimoto, N. Carlsson, N. Ikeda, and K. Asakawa. Observation of small group velocity in two-dimensional algaas-based photonic crystal slabs. *Physical Review B (Condensed Matter and Materials Physics)*, 65(12):1–4, 2002.

[67] Takashi Asano, Kazuaki Kiyota, Daisuke Kumamoto, Bong-Shik Song, and Susumu Noda. Time-domain measurement of picosecond light-pulse propagation in a two-dimensional photonic crystal-slab waveguide. *Applied Physics Letters*, 84(23):4690–4692, 2004.

[68] H. Gersen, T.J. Karle, R.J.P. Engelen, W. Bogaerts, J.P. Korterik, N.F. Van Hulst, T.F. Krauss, and L. Kuipers. Real-space observation of ultraslow light in photonlc crystal waveguides. *Physical Review Letters*, 94(7):1–4, 2005.

[69] P.F. Xing, P.I. Borel, L.H. Frandsen, A. Harpøth, and M. Kristensen. Optimization of bandwidth in 60^0 photonic crystal waveguide bends. *Optics Communications*, 248(1-3):179–184, 2005.

[70] M. Thorhauge, L.H. Frandsen, P.I. Borel, A. Harpøth, Y.X. Zhuang, M. Kristensen, W. Bogaerts, P. Dumon, R. Baets, V. Wiaux, J. Wouters, and S. Beckx. Novel low-loss 60 degrees bends in photonic crystal waveguides. *Conference on Lasers and Electro-Optics (CLEO)*, page 2 pp. vol.1, 2004.

[71] L.H. Frandsen, P.L Borel, M. Thorhange, J. Cheng, M. Kampanis, M. Kristensen, A. Lavrinenko, Y. Zhuang, and H.M.H. Chong. Propagation of te and tm polarised light through smoothed sixty degree bends in planar photonic

crystal waveguides. *Lasers and Electro-Optics Europe, 2003. CLEO/Europe. 2003 Conference on*, page 677, 2003.

[72] A. Chutinan, M. Okano, and S. Noda. Wider bandwidth with high transmission through waveguide bends in two-dimensional photonic crystal slabs. *Applied Physics Letters*, 80(10):1698–700, 2002.

[73] S. Boscolo, M. Midrio, and T.F. Krauss. Y junctions in photonic crystal channel waveguides: High transmission and impedance matching. *Optics Letters*, 27(12):1001–1003, 2002.

[74] Jasmin Smajic, Christian Hafner, and Daniel Erni. Design and optimization of an achromatic photonic crystal bend. *Optics Express*, 11(12):1378–1384, 2003.

[75] E. Yablonovitch. Inverse design of dielectric and plasmonic crystals. *Technical Digest: International Symposium on Photonic Crystals and Electromagnetic Structures V (PECS-V)*, paper Tu-D1:73, 7.–11. March, Kyoto 2004.

[76] A. Hakansson, J. Sanchez-Dehesa, and L. Sanchis. Inverse design of photonic crystal devices. *Selected Areas in Communications, IEEE Journal on*, 23(7):1365–1371, 2005.

[77] Martin Burger, Stanley J. Osher, and Eli Yablonovitch. Inverse problem techniques for the design of photonic crystals. *IEICE Transactions on Electronics*, E87-C(3):258–265, 2004.

[78] S.J. Cox and D.C. Dobson. Band structure optimization of two-dimensional photonic crystals in h-polarization. *Journal of Computational Physics*, 158(2):214–24, 2000.

[79] David C. Dobson and Fadil Santosa. Optimal localization of eigenfunctions in an inhomogeneous medium. *SIAM Journal on Applied Mathematics*, 64(3):762–774, 2004.

[80] O. Sigmund and J. Jensen. Systematic design of phononic band-gap materials and structures by topology optimization. *Phil. Trans. R. Soc. Lond. A*, 361:1001–1019, 2003.

[81] P. I. Borel, A. Harpøth, L. H. Frandsen, M. Kristensen, P. Shi, J. S. Jensen, and O. Sigmund. Topology optimization of photonic crystal structures. *Optics Express*, 12(9):1996–2001, 2004.

[82] J. S. Jensen and O. Sigmund. Systematic design of photonic crystal structures using topology optimization: Low-loss waveguide bends. *Appl. Phys. Lett.*, 84(12):2022–2024, 2004.

[83] J. S. Jensen and O. Sigmund. Topology optimization of photonic crystal structures: A high bandwidth low loss T-junction waveguide. *J. Opt. Soc. Am. B*, 2005.

[84] Jakob S. Jensen. Department of Mechanical Engineering, DTU, Private communication, jsj@mek.dtu.dk.

[85] Ole Sigmund. Department of Mechanical Engineering, DTU, Private communication, sigmund@mek.dtu.dk.

[86] L. H. Frandsen, A. Harpøth, P. I. Borel, M. Kristensen, J. S. Jensen, and O. Sigmund. Broadband photonic crystal waveguide 60° bend obtained utilizing topology optimization. *Optics Express*, 12(24):5916–5921, 2004.

[87] W. Bogaerts, V. Wiaux, P. Dumon, D. Taillert, J. Wouters, S. Beckx, J. Van Campenhout, B. Luyssaert, and R. Baets. Large-scale production techniques for photonic nanostructures. *Proc. SPIE*, 5225:101–112, 2003.

[88] W. Bogaerts, V. Wiaux, D. Taillaert, S. Beckx, B. Luyssaert, P. Bienstman, and R. Baets. Fabrication of photonic crystals in silicon-on-insulator using 248-nm deep UV lithography. *IEEE J. Sel. Top. Quantum Electron.*, 8:928–934, 2002.

[89] Peixiong Shi. Senior Process Engineer, Ph.D, Private communication, pxshi@danchip.dtu.dk.

[90] S. J. McNab, N. Moll, and Y. A. Vlasov. Ultra-low loss photonic integrated circuits with membrane-type photonic crystal waveguides. *Optics Express*, 11(22):2927–2939, 2003.

[91] Hudek P. Eisenmann H. Belic N., Jaritz R. Efficient e-beam proximity correction for high acceleration voltages. *Internal Paper from PDF Solutions, http://www.aiss.de/PROXECCO/PROXECCO.html*, 2005.

[92] T.H.P. Chang. Proximity effect in electron-beam lithography. *Journal of Vacuum Science and Technology*, 12(6):1271–5, 1976.

[93] Bengt Nilsson. Chalmers University of Technology, MC2 Process Laboratory, Private communication, bengt.nilsson@mc2.chalmers.se.

[94] H. Eisenmann, T. Waas, and H. Hartmann. Proxecco-proximity effect correction by convolution. *Journal of Vacuum Science & Technology B (Microelectronics Processing and Phenomena)*, 11(6):2741–5, 1993.

[95] International Technology Roadmap for Semiconductors. International technology roadmap for semiconductors, 2005 edition, lithography. *http://www.itrs.net/Common/2005ITRS/Litho2005.pdf*.

[96] T. Nielsen, D. Nilsson, F. Bundgaard, P. Shi, P. Szabo, O. Geschke, and A. Kristensen. Nanoimprint lithography in the cyclic olefin copolymer, topas®, a higly ultraviolet-transparent and chemically resistant thermoplast. *J. Vac. Sci. Technol. B*, 22(4):1770–1775, 2004.

[97] Bienstmann P. Bogaerts, W. and R. Baets. Scattering at sidewall roughness in photonic crystal slabs. *Optics Letters*, 28(9):689–691, 2003.

[98] R. Legtenberg, H. Jansen, M. de Boer, and Elwenspoek M. Anisotropic reactive ion etching of silicon using $sf_6/o_2/chf_3$ gas mixtures. *J. Electrochem. Soc.*, 142(6):2020–2028, 1995.

[99] H.-C. Liu, Y.-H. Lin, and W. Hsu. Sidewall roughness control in advanced silicon etch process. *Microsystem Technologies*, 10(1):29–34, 2003.

[100] S. M Sze. *Semicondutor Devices: Physics and Technology*. John Wiley & Sons, 1985.

[101] S. Jensen. *Inductively Coupled Plasma Etching for Microsystems*. PhD thesis, Department of Micro and Nanotechnology, MIC, Technical University of Denmark, 2004.

[102] B. A. M. Andersen, O. Hansen, and M. Kristensen. Spatial variation of the etch rate for deep etching of silicon by reactive ion etching. *J. Vac. Sci. Technol. B*, 15(4):993–999, 1997.

[103] Lars Hagedorn Frandsen. Master thesis: Fabrication and characterization of PBG waveguide components. Master's thesis, Research Center COM, Technical University of Denmark, 2003.

[104] Rune Jacobsen. Postdoc, Ph.D.,Department of Communications, Optics, and Materials, DTU, Private communication, rune@com.dtu.dk.

[105] Beate Zsigri. Postdoc, Ph.D.,Department of Communications, Optics, and Materials, DTU, Private communication, bz@com.dtu.dk.

[106] Christophe Peucheret. Assistant Professor, Department of Communications, Optics, and Materials, DTU, Private communication, cp@com.dtu.dk.

[107] L. Frandsen C. Peucheret B. Zsigri G. Moulin J. Fage-Pedersen R. Jacobsen, A. Lavrinenko and P. Borel. Direct experimental and numerical determination of extremely high group indices in photonic crystal waveguides. *Optics Express*, 13:7861–7871, 2005.

[108] Rune Shim Jacobsen. *Electro-optic modulation, measurement technique and enhancement*. PhD thesis, Research Center COM, Technical University of Denmark, 2005.

[109] Sergey I. Bozhevolnyi, Valentyn S. Volkov, Jesper Arentoft, Alexandra Boltasseva, Thomas Soendergaard, and Martin Kristensen. Direct mapping of light propagation in photonic crystal waveguides. *Optics Communications*, 212(1-3):51–55, 2002.

[110] V.S. Volkov, S.I. Bozhevolnyi, P.I. Borel, L.H. Frandsen, and M. Kristensen. Near-field characterization of low-loss photonic crystal waveguides. *Physical Review B (Condensed Matter and Materials Physics)*, 72(3):35118, 2005.

[111] Valentyn S. Volkov. Institute of Physics and Nanotechnology, Aalborg University, volkov@physics.auc.dk.

[112] Sergey I. Bozhevolnyi. Institute of Physics and Nanotechnology, Aalborg University.

[113] P.I. Borel L.H. Frandsen M. Kristensen V.S. Volkov, S.I. Bozhevolnyi and H.M.H. Chong. Near-field imaging of low loss photonic crystal waveguides. *Proceedings of ECOC'03*, 5(Tu4.1.3):68–69, 2003.

[114] P.I. Borel, L.H. Frandsen, M. Thorhauge, A. Boltasseva, J. Cheng, M. Kampanis, M. Kristensen, A. Lavrinenko, K. Rechendorff, R. Shim, Y. Zhuang, and H.M.N. Chong. Very low losses for tm polarized light in photonic crystal waveguides. *Lasers and Electro-Optics, 2003. CLEO '03. Conference on*, pages 957–958, 2003.

[115] N. Ikeda, Y. Sugimoto, Y. Tanaka, K. Inoue, and K. Asakawa. Low propagation losses in single-line-defect photonic crystal waveguides on gaas membranes. *Selected Areas in Communications, IEEE Journal on*, 23(7):1315–1320, 2005.

[116] E Kuramochi, M Notomi, S Hughes, A Shinya, T Watanabe, and L Ramunno. Rapid communications - semiconductors ii - surfaces, interfaces, microstructures, and related topics - disorder-induced scattering loss of line-defect waveguides in photonic crystal slabs (4 pages). *Physical Review - Section B - Condensed Matter*, 72(16):161318R, 2005.

[117] Dario Gerace and Lucio Claudio Andreani. Disorder-induced losses in photonic crystal waveguides with line defects. *Optics Letters*, 29(16):1897–1899, 2004.

[118] D. Gerace and L.C. Andreani. Effects of disorder on propagation losses and cavity q-factors in photonic crystal slabs. *Photonics and Nanostructures - Fundamentals and Applications*, 3(2-3):120–128, 2005.

[119] A. Chutinan, M. Okano, and S. Noda. Wider bandwidth with high transmission through waveguide bends in two-dimensional photonic crystal slabs. *Appl .Phys. Lett.*, 80(10):1698–1700, 2002.

[120] A. Talneau, L. Le Gouezigou, N. Bouadma, M. Kafesaki, C. M. Soukolis, and M. Agio. Photinic-crystal ultrashort bends with imrpovedtransmission and low refelction at 1.55 μm. *Appl. Phys. Lett.*, 80(4):547–549, 2002.

[121] Edmond Chow, S.Y. Lin, J.R. Wendt, S.G. Johnson, and J.D. Joannopoulos. Quantitative analysis of bending efficiency in photonic-crystal waveguide bends at *lambda* = 1.55mu@m wavelengths. *Optics Letters*, 26(5):286–288, 2001.

[122] Y. Sugimoto, Y. Tanaka, N. Ikeda, H. Nakamura, K. Kanamoto, S. Ohkouchi, Y. Watanabe, K. Inoue, and K. Asakawa. Fabrication and characterization of photonic crystal-based symmetric mach-zehnder (pc-smz) structures based on gaas membrane slab waveguides. *Selected Areas in Communications, IEEE Journal on*, 23(7):1308–1314, 2005.

[123] M. Kristensen, L.H. Frandsen, A. Harpøth, Y.X. Zhuang, P.I. Borel, W. Bogaerts, P. Dumon, R. Baets, V. Wiaux, J. Wouters, and S. Beckx. Large bandwidth 60^0 bend in photonic crystal waveguides. *PECS-V: International Symposium on Photonic and Electromagnetic Crystal Structures*, pages Paper Tu–F5, 2004.

[124] J. S. Jensen, O. Sigmund, L. H. Frandsen, P. I. Borel, A. Harpøth, and M. Kristensen. Topology design and fabrication of a new double 90-degree photonic crystal waveguide bend. *Photonics Technology Letters*, 2004.

[125] M. Tokushima, H. Kosaka, A. Tomita, and H. Yamada. Lightwave propagation through a 120degrees sharply bent single-line-defect photonic crystal waveguide. *Applied Physics Letters*, 76(8):952–954, 2000.

[126] R.L. Espinola, R.U. Ahmad, F. Pizzuto, M.J. Steel, and R.M. Osgood Jr. A study of high-index-contrast 90^o waveguide bend structures. *Optics Express*, 8(9):517–528, 2001.

[127] M.D.B. Charlton, M.E. Zoorob, G.J. Parker, M.C. Netti, J.J. Baumberg, S.J. Cox, and H. Kemhadjian. Experimental investigation of photonic crystal waveguide devices and line-defect waveguide bends. *Materials Science and Engineering: B*, 74(1-3):17 – 24, 2000.

[128] S. Boscolo, M. Midrio, and T. F. Krauss. Y-junctions in photonic crystal channel waveguides: High transmission and impedance matching. *Opt. Lett.*, 27(12):1001–1003, 2002.

[129] Y. Sugimoto, N. Ikeda, N. Carlsson, K. Asakawa, N. Kawai, and K. Inoue. Light-propagation characteristics of y-branch defect waveguides in algaas-based air-bridge-type two-dimensional photonic crystal slabs. *Optics Letters*, 27(6):388–390, 2002.

[130] S.Y. Lin, E. Chow, J. Bur, S.G. Johnson, and J.D. Joannopoulos. Low-loss, wide-angle y splitter at [similar to]1.6-μm wavelengths built with a two-dimensional photonic crystal. *Optics Letters*, 27(16):1400–1402, 2002.

[131] L. H. Frandsen, P. I. Borel, Y. X. Zhuang, A. Harpøth, M. Thorhauge, M. Kristensen, W. Bogaerts, P. Dumon, R. Baets, J. Wiaux, and S. Beckx. Ultralow-loss 3-dB photonic crystal splitter. *Opt. Lett.*, 29(14):1623, 2004.

[132] P.I. Borel, L.H. Frandsen, A. Harpøth, M. Kristensen, J. S. Jensen, and O. Sigmund. Topology optimised broadband photonic crystal y-splitter. *Electronics Letters*, 41(2), 2005.

[133] L.H. Frandsen, A. Harpøth, K.K. Hede, M. Kristensen, P.I. Borel, J.S. Jensen, and O. Sigmund. Topology optimised photonic crystal 1x4 waveghuide splitter. *PECS-VI: International Symposium on Photonic and Electromagnetic Crystal Structures*, Poster B14, 2005.

[134] V.S. Volkov, S.I. Bozhevolnyi, P.I. Borel, L.H. Frandsen, and M. Kristensen. Near-field characterization of photonic crystal y-splitters. *Physica Status Solidi C: Conferences*, 2(12):4087–4092, 2005.

[135] L.H. Frandsen, P.I. Borel, J.S. Jensen, and O. Sigmund. Topology optimized photonic wire splitters. *Accepted for publication in Proceedings of CLEO USA'06*, 2006.

[136] Vlasov Y. A. Sekraric, L. and S. J. McNab. Y-splitters in photonic wires and photonic crystal waveguides. *Proceedings of PECS-VI, poster session D*, 2005.

[137] Tapio Niemi. Senior Researcher, Ph.D, Optoelectronics Research Centre, Tampere University of Technology, tapio.Niemi@orc.tut.fi.

[138] T. Niemi, L.H. Frandsen, K.K. Hede, A. Harpoth, P.I. Borel, and M. Kristensen. Wavelength-division demultiplexing using photonic crystal waveguides. *Photonics Technology Letters, IEEE*, 18(1):226–228, 2006.

[139] A. Têtu, L. Yang, A. Lavrinenko, L.H. Frandsen, and P.I. Borel. Enhancement of coupling to the slow light regime in photonic crystal waveguides using topology optimization. *Accepted for publication in Proceedings of CLEO USA'06*, 2006.

[140] M.K. Smit, E.C.M. Pennings, and H. Blok. A normalized approach to the design of low-loss optical waveguide bends. *Lightwave Technology, Journal of*, 11(11):1737–1742, 1993.

[141] N. Moll and G.-L. Bona. Bend design for the low-group-velocity mode in photonic crystal-slab waveguides. *Applied Physics Letters*, 85(19):4322–4324, 2004.

[142] S. Assefa, S. McNab, and Y. Vlasov. Transmission of slow light through photonic crystal waveguide bends. *Accepted for publication in Optics Letters*, 2006.

[143] A. Lavrinenko, A. Têtu, L.H. Frandsen, and P.I. Borel. Optimization of photonic crystal 60^o waveguide bends in the slow light regime for broadband transmission. *In preparation*, 2006.

[144] Guido Mertens, Thorsten Roder, Ralf Schweins, Klaus Huber, and Heinz-S Kitzerow. Shift of the photonic band gap in two photonic crystal/liquid crystal composites. *Applied Physics Letters*, 80(11):1885–1887, 2002.

[145] Ch. Schuller, F. Klopf, J.P. Reithmaier, M. Kamp, and A. Forchel. Tunable photonic crystals fabricated in iii-v semiconductor slab waveguides using infiltrated liquid crystals. *Applied Physics Letters*, 82(17):2767–2769, 2003.

[146] S.W. Leonard, J.P. Mondia, H.M. Van Driel, O. Toader, S. John, K. Busch, A. Bimer, U. Gosele, and V. Lehmann. Tunable two-dimensional photonic crystals using liquid-crystal infiltration. *Physical Review B (Condensed Matter)*, 61(4):2389–2392, 2000.

[147] P.G. de Gennes and J. Prost. *The Physics of Liquid Crystals*. Clarendon Press, 1993.

[148] Thomas Tanggaard Alkeskjold. *Optical devices based on liquid crystal photonic bandgap fibers*. PhD thesis, Research Center COM, Technical Univeristy of Denmark, 2005.